



저작자표시-비영리-변경금지 2.0 대한민국

이용자는 아래의 조건을 따르는 경우에 한하여 자유롭게

- 이 저작물을 복제, 배포, 전송, 전시, 공연 및 방송할 수 있습니다.

다음과 같은 조건을 따라야 합니다:



저작자표시. 귀하는 원저작자를 표시하여야 합니다.



비영리. 귀하는 이 저작물을 영리 목적으로 이용할 수 없습니다.



변경금지. 귀하는 이 저작물을 개작, 변형 또는 가공할 수 없습니다.

- 귀하는, 이 저작물의 재이용이나 배포의 경우, 이 저작물에 적용된 이용허락조건을 명확하게 나타내어야 합니다.
- 저작권자로부터 별도의 허가를 받으면 이러한 조건들은 적용되지 않습니다.

저작권법에 따른 이용자의 권리는 위의 내용에 의하여 영향을 받지 않습니다.

이것은 [이용허락규약\(Legal Code\)](#)을 이해하기 쉽게 요약한 것입니다.

[Disclaimer](#)

Doctor of Philosophy

ELECTRICALLY ASSISTED JOINING AND
FORMING OF AUTOMOTIVE STAINLESS STEELS

The Graduate School of the University of Ulsan

School of Mechanical Engineering

Viet Tien Luu

ELECTRICALLY ASSISTED JOINING AND
FORMING OF AUTOMOTIVE STAINLESS STEELS

Advisor: **Sung-Tae Hong**

A Dissertation

Submitted to

the Graduate School of the University of Ulsan

In Partial Fulfillment of the Requirements

for the Degree of

Doctor of Philosophy

By

Viet Tien Luu

School of Mechanical Engineering

Ulsan, Korea

December 2018

Viet Tien Luu 의

공학박사 학위 논문을 인준함

심사위원	천두만	
심사위원	홍성태	
심사위원	염영진	
심사위원	김동규	
심사위원	김문조	

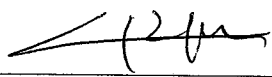
울산대학교 대학원

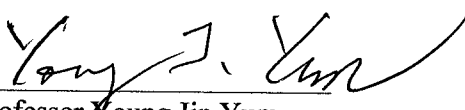
기계자동차공학과

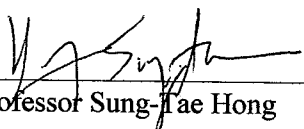
2018년 12월

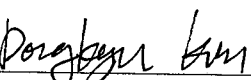
ELECTRICALLY ASSISTED JOINING AND FORMING OF AUTOMOTIVE STAINLESS STEELS

This certifies that the dissertation
of Viet Tien Luu is approved

Committee Chair 
Professor Doo-Man Chun

Committee Member 
Professor Young Jin Yum

Committee Member 
Professor Sung-Tae Hong

Committee Member 
Professor Dong-Kyu Kim

Committee Member 
Dr. Moon-Jo Kim

School of Mechanical Engineering

Ulsan, Korea

December 2018

ACKNOWLEDGMENTS

I would first like to express my deeply sincere thanks to my advisor, Professor Sung-Tae Hong, for constant advice, support, and encouragement during my study. His guidance makes me the completion of this dissertation possible. I would also like to thank my doctoral committee, Professor Young Jin Yum, Professor Doo-Man Chun, Professor Dong-Kyu Kim, and Dr. Moon-Jo Kim, for their assistance and suggestions. I am grateful to my colleagues in the Laboratory of Advanced Engineering Materials for creating my pleasant working environment. Special thanks are due to Dr. Hrishikesh Das for his support and valuable comments on my studies, and to Ju-Ri Kim, Gi Dong Park, Yong-Ha Jeong, Dinh Thi Kieu Anh, Tran Van Loi and Nguyen Thi Anh Nguyet for the assistance with the experiments. I would also to thank professor Heung Nam Han and his students, Micro Mechanics & Material Processing Design Laboratory for their help and valuable discussions during my studies. In addition, I gratefully acknowledge Sejong Company, Hyundai Motor Company and the Korean government for the financial and technical support that allowed me to do this work. Finally, I would like to thank my family and friends for their support and encouragement. Without them, I do not know where I would be.

TABLE AND CONTENTS

ACKNOWLEDGMENTS	ii
LIST OF FIGURES	v
LIST OF TABLES	ix
ABSTRACT	x
CHAPTER I	1
INTRODUCTION	1
References.....	10
CHAPTER II	17
DIFFUSION ENHANCEMENT DURING ELECTRICALLY ASSISTED BRAZING OF FERRITIC STAINLESS STEEL ALLOYS	17
2.1 Introduction	18
2.2 Experimental set-up.....	21
2.3 Results and discussion.....	28
2.4 Conclusion.....	42
References.....	43
CHAPTER III	46
FEASIBILITY OF A TWO-STAGE FORMING PROCESS OF 316L AUSTENITIC STAINLESS STEELS WITH RAPID ELECTRICALLY ASSISTED ANNEALING ... 46	
3.1 Introduction	47
3.2 Experimental set-up.....	50
3.3 Results and discussion.....	55
3.4 Conclusion.....	69
References.....	70

CHAPTER IV	73
ELECTRICALLY ASSISTED SUBSECOND ANNEALING OF PRESTRAINED 304 AUSTENITIC STAINLESS STEEL SHEETS	73
4.1 Introduction	74
4.2 Experimental set-up.....	77
4.3 Results and discussion.....	83
4.4 Conclusion.....	100
References.....	101
CHAPTER V	105
INDUSTRIAL APPLICATIONS	105
5.1 Industrial application of electrically assisted brazing in automotive exhaust systems	96
5.2 Electrically assisted springback reduction of bipolar plates for fuel cell.....	113
CHAPTER VI	121
CONCLUSION.....	121

LIST OF FIGURES

Figure 2. 1 (a) Schematic of brazing specimen and the experimental set-up for: (b) electrically assisted brazing and (c) induction brazing.....	26
Figure 2. 2 Schematic of temperature histories for (a) electrically assisted brazing and (b) induction brazing	27
Figure 2. 3 Temperature histories of (a) electrically assisted brazing and (b) induction brazing for various brazing conditions	30
Figure 2. 4 Cross-sectional images: (a) SEM micrograph of electrically assisted brazing ($t_h = 0$ sec), (b) EBSD inverse pole (IPF) map of electrically assisted brazing ($t_h = 5$ sec), and (c) SEM micrograph of interlayer (filler metal) of electrically assisted brazing ($t_h = 0$ sec).....	32
Figure 2. 5 SEM-EDS elemental line scans of Ni, Cr, Si, and Fe across the brazing joint: EA brazing for (a) $t_h = 0$ sec, (b) $t_h = 5$ sec and induction brazing for (c) $t_h = 0$ sec and (d) $t_h = 20$ sec	34
Figure 2. 6 The Ni distribution: electrically assisted brazing for (a) $t_h = 0$ sec, (b) $t_h = 5$ sec and induction brazing for (c) $t_h = 0$ sec and (d) $t_h = 20$ sec	36
Figure 2. 7 The diffusion thickness as a function of the square root of diffusion time	40
Figure 2. 8 Cross-sectional image of brazing joints after shear test for electrically assisted brazing specimen for $t_h = 5$ sec	41
Figure 2. 9 Comparison of shear strength: electrically assisted brazing for $t_h = 0$ sec (EAB1), $t_h = 5$ sec (EAB2), and $t_h = 10$ sec (EAB3) and induction brazing for holding time of $t_h = 0$ sec (I1), $t_h = 10$ sec (I2) and $t_h = 20$ sec (I3)	41

Figure 3. 1 Schematics of (a) electrically assisted (EA) annealing with a single pulse of electric current and (b) the experimental set-up	52
Figure 3. 2 A stress–strain curve of a baseline specimen	54
Figure 3. 3 (a) Temperature histories of 60% prestrained specimens and (b) the peak temperatures as functions of current density during EA annealing for different prestrains	56
Figure 3. 4 Engineering stress-strain curves after EA annealing with (a) 20% prestrain and (b) 60% prestrain; the engineering stress-strain curves during reloading was constructed based on the gage length and the cross-sectional area at each prestrain.....	57
Figure 3. 5 (a) Post-annealing yield strength and (b) post-annealing elongation of prestrained specimens after EA annealing.....	59
Figure 3. 6 (a) Total achievable elongation as a function of current density and (b) the effect of prestrain and the current density on the total achievable elongation; the total achievable elongation was calculated based on the original gage length of the baseline specimen.....	60
Figure 3. 7 True stress-strain curves after EA annealing with (a) 20% prestrain and (b) 60% prestrain; (c) strain hardening exponent and (d) strength coefficient of prestrained specimens after EA annealing	63
Figure 3. 8 Full width at half maximum (FWHM) profiles of specimens with (a) 20% prestrain and (b) 60% prestrain.....	66
Figure 3. 9 Electron backscatter diffraction system (EBSD) inverse pole figures for normal direction (ND) and kernel average misorientation (KAM) maps of specimens with (a) 20%	

prestrain and (b) 60% prestrain for various electric current densities; (c) Grain orientation spread (GOS) maps of specimens with 60% prestrain for various electric current densities. 68

Figure 4. 1 Schematics of (a) EA annealing with a single pulse of electric current and (b) the experimental set-up..... 81

Figure 4. 2 A stress-strain curve of a baseline specimen..... 82

Figure 4. 3 Temperature histories of 20% prestrained specimens and (b) the peak temperatures as functions of current density during EA annealing for different prestrains..... 84

Figure 4. 4 (a) Inverse pole figure maps of baseline specimen for grain size determination. The grain size of baseline specimen is $17.0 \pm 5.9 \mu\text{m}$; (b) a true stress and strain hardening rate as a function of true strain of a baseline specimen 85

Figure 4. 5 Engineering stress-strain curves after EA annealing with (a) 20% prestrain and (b) 60% prestrain; the engineering stress-strain curves during reloading was constructed based on the gage length and the cross-sectional area at each prestrain..... 88

Figure 4. 6 (a) Post-annealing yield strength and (b) post-annealing elongation of prestrained specimens after EA annealing..... 89

Figure 4. 7 The flow curves and strain hardening rates with respect to true strain at different prestrain of SUS304 after EA annealing for (a) 20% prestrain and (b) 60% prestrain 90

Figure 4. 8 (a) Total achievable elongation as a function of current density and (b) the effect of prestrain and the current density on the total achievable elongation; the total achievable elongation was calculated based on the original gage length of the baseline specimen..... 91

Figure 4. 9 FWHM profiles of specimens with (a) 20% prestrain and (b) 60% prestrain..... 95

Figure 4. 10 X-ray diffraction spectra of specimens: (a) before EA annealing (b) with 60% prestrain after EA annealing	96
Figure 4. 11 EBSD inverse pole figures for ND and phase maps of specimens with (a) 20% prestrain and (b) 60% prestrain for various electric current densities	97
Figure 4. 12 Kernel average misorientation (KAM) maps with (a) 20% prestrain and (b) 60% prestrain for various electric current densities	98
Figure 4. 13 Grain orientation spread (GOS) maps of specimens with 60% prestrain for various electric current densities	99
Figure 5. 1 Schematic of an automotive gas exhaust pipe system.....	106
Figure 5. 2 Schematic of experimental set-up for EA brazing exhaust pipe system	109
Figure 5. 3 Brazed joints of exhaust pipe systems after EA brazing	111
Figure 5. 4 The optical microscope of the brazed joint after EA brazing; blue dash line as marked the intermetallic layers; thickness of intermetallic layers in top and bottom of the brazed joint is a range of 3.0 to 4.0 μm	112
Figure 5. 5 (a) Electrically assisted springback reduction procedure of bipolar plates and (b) Schematic of experimental set-up in EA springback test	115
Figure 5. 6 A SUS316L bipolar plate specimen after EA springback.....	117
Figure 5. 7 Springback reduction height of bipolar plates after applying electric current	118

LIST OF TABLES

Table 2. 1 Chemical composition of ferritic stainless steel and filler material (AMS 4777) .	24
Table 2. 2 Heating parameters for electrically assisted brazing and induction brazing	24
Table 4. 1 The chemical composition of SUS304 sheets from EPMA analysis.....	78
Table 4. 2 Experimental parameters	78
Table 5. 1 Heating parameters for electrically assisted brazing and induction brazing	110
Table 5. 2 Springback test parameters	116

ABSTRACT

Electrically assisted manufacturing (EAM) is a new manufacturing technique that has the potential to improve the cost-efficiency of essentially every metal joining process, forming process, and enable greater process capabilities. In this process, electric current is passed through a metal workpiece. Naturally, the electric current can rapidly increase the temperature of the metals by resistance heating (Joule heating). The effectiveness of resistance heating as a repeat heat source for joining and forming may be accompanied by the benefits of thermal (Joule heating) and the possibility of additional athermal (electroplasticity) with the electric current. Especially, the electric current may induce the electroplasticity, wherein the electric current enhances the mobility of atoms such as the impact of the electrons to dislocations to accelerate the movement of dislocation and scatter of electrons to interfacial defects to increase the resistivity of the metals. As electroplasticity has been widely studied, EAM processes have been increasingly applied. The applications of EAM processes are mainly associated with sheet metal forming, bulk deformation, and electrically assisted (EA) joining for various metal alloys (i.e. Stainless steels, Ultra high strength steels, Aluminum alloys, Magnesium alloys, Titanium alloys). This dissertation presents studies on the feasibility of EA joining and EA forming of stainless steels by applying electric current.

Firstly, the electrically assisted (EA) brazing of a ferritic stainless steel (FSS) with nickel-based filler metal is experimentally investigated. Microstructural analysis results strongly suggest that the electric current during EA brazing enhances diffusion between the filler metal and the FSS, thus inducing significantly thicker diffusion zones compared with induction brazing. In the present study, the EA brazing provides the technical advantage that the process time can be significantly reduced without sacrificing the joint strength (or a higher joint strength with a similar process time) in comparison with induction brazing.

Next, a two-stage forming process of the selected 316L austenitic stainless steel (SUS316L) with rapid EA annealing is experimentally investigated. A single pulse of electric current is applied to the prestrained specimen with a short duration time right after first deformation (prestrain). The stress-strain curve during reloading shows that the flow stress of the SUS316L significantly decreases, which indicates the occurrence of EA annealing. The electric current also increases the maximum achievable elongation of the SUS316L during reloading. The stress-strain curve during reloading and the microstructural observation suggest that the effects of EA annealing on the post-annealing mechanical behavior and microstructure strongly depend on both the applied electric current density (electric current per unit cross-sectional area) and the given prestrain.

Finally, electrically assisted (EA) subsecond annealing of prestrained austenitic 304 stainless steel (SUS304) sheets is carried out. The post-annealing tensile test of two different prestrains is compared with each other by applying the same current densities. The post-annealing stress-strain curve during reloading shows that the flow stress of the SUS304 significantly decreases, while the maximum achievable elongation significant increases with increasing electric current. Microstructural analysis confirms the occurrence of electrically induced annealing and the phase transformations. The results of the present study can be used to improve the formability of the SUS304 in sheet metal forming processes with electric current.

The results of the present study will be used as basic data and methodologies for the development of joining and forming processes in manufacturing by using electric current. Specifically, both EA joining and EA forming processes are contributed to the development of brazing exhaust pipe systems and springback reduction bipolar plates for fuel cell in the automotive industry.

CHAPTER I

INTRODUCTION

Formability is an important issue for all metallic materials in forming processes, even for stainless steels. Stainless steels are iron-based alloys containing greater than approximately 11Cr wt.% as principal alloying elements. The stainless steels require this level of Cr content or more for their corrosion resistance through the formation of a continuous thin layer of passive film on their surface to protect the substrate in a wide range of environments (Correa et al., 2010; Umoru et al., 2008). Depending on the metallurgical structure of iron in the stainless steels, these alloys can be classified into different groups:

Ferritic stainless steel (FSS) grades have chemical compositions containing Fe, 12-30Cr wt.% and less than 0.15C wt.%. The higher amount of Cr and less amount of Ni in FSS is responsible for ferrite with body centered cubic (BCC) crystal as the dominant microstructure. FSSs have excellent applications in architectural and process industries. FSSs have remained the best candidate materials for the automotive exhausts and flue systems because of their excellent stress corrosion cracking resistance, adequate high temperature resistance to oxidation (Kim et al., 2017a; Mohandas et al., 1999). FSSs also have been widely used for the manufacture of domestic appliances and packaging in food industries.

Austenitic stainless steel (ASS) grades have typical compositions containing Fe, 16-30Cr wt.%, 8-25Ni wt.% and less than 0.15C wt.%. Additions of austenite stabilizing elements namely Nickel, Manganese and in particular, the interstitial elements such as Carbon and Nitrogen can significantly modify the gamma (γ) loop to achieve face centered cubic (FCC) structure. The predominant microstructure in austenitic stainless steels at ambient temperature is austenite. However, strain-induced martensitic transformation can simultaneously occur depending on chemical composition, temperature, grain size, strain rate

(Huang et al., 1989; Rocha and Oliveira, 2009; Geijselaers and Perdahcioğlu, 2009). They may also be alloyed with nitrogen and molybdenum in order to further increase corrosion resistance. Austenitic stainless steels are non-magnetic in the annealed condition and can be strain hardened during the plastic deformation, including cold work (McGuire, 2008). Austenitic stainless steels are general purpose grades used in applications requiring a good combination of corrosion resistance and formability (Peterson et al., 1997; Takakuwa and Soyama, 2014; Follansbee, 2015). They have a wide range of applications in process plants, cryogenic plants, food industry and nuclear industry. The primary electronic components, hot work components, and complexity components were manufactured from types 304, 316L and 321 (Anderson et al., 2013; McGuire, 2008).

Martensitic stainless steel (MSS) grades have typical composition containing Fe, 10.5-18Cr wt.% and 0.15-1C wt.%. Martensitic Stainless Steels derive its name from martensite, which is the predominant microstructure at room temperature. They have body centered tetragonal (BCT) crystal structure in the hardened condition. These steels have good toughness and are used in manufacturing turbine and compressor blades and corrosion resistant castings. Martensitic stainless steels are ferromagnetic. They have poor formability and may be subject to impact transition at low temperature. Martensitic stainless steels are resistant to corrosion in the relatively mild environment. They have unique advantage of high strength with adequate toughness, wear resistance and good fatigue resistance after heat treatments, which make them suitable for some special applications. They are largely used for turbine components, valve parts, fasteners, cutlery, mining equipment and in oil and gas industries. High carbon grades of MSS are not suitable for applications which involve welding; high ductility; a greater degree of formability and operation temperature between 400-600°C to avoid the risk of temper embrittlement and inter-granular attack by sensitization.

Duplex stainless steel (DSS) grades are hybrid of ferritic and austenitic stainless steels with typical compositions containing Fe, 20-30Cr wt.%, 2-8Ni wt.%, 1-3Mo wt.% with extra low carbon. At elevated temperature, the melt solidifies into ferrite from which austenite is precipitated. The volume fraction of austenite in ferrite matrix depends on the cooling rate and presence of austenite stabilizing alloys (like Ni). In commercial practice, DSS may be heat treated at temperature in the range 1050-1150°C and then water quenched to obtain microstructures of about 50% ferrite and 50% austenite (Gideon et al., 2008; Olaseinde et al., 2013). Some duplex stainless steels have superplastic properties. They can be subjected to uniform large deformations without local necking at about half of their absolute temperature. The super plasticity of DSS is favored by the small grain sizes obtained from ferrite-austenite phase transformation (Gideon et al., 2008; Olaseinde et al., 2013). They have higher strength than austenitic stainless steels. The presence of higher amount of Cr, Mo, and N offers DSS good resistance to localized and uniform corrosion. Duplex stainless steels are used in power industry feedwater heaters and flue-gas scrubbers. They are also used in the chemical industry for heat exchangers, pressure vessels and for oil and gas production equipment.

In the past, several techniques were attempted to metal joining and forming process with stainless steels. Within this subsection, the most common techniques are described and their advantages/disadvantages discussed.

- Joining by forming process are widely used to permanently join two or more metals through plastic deformation. The main advantages of the joining by forming are saving in materials which reduce the weight ratio, a wide range of joining materials including dissimilar ones, and environment safety. However, the process still has some disadvantages such as geometrical unevenness of joining zone due to nature of processes, more difficult correction and repair, and lack of standardization and calculation methods. Also, this technique requires high forming force during joining leads to high investment capital equipment.

- Welding is a joining process wherein metallic components are joined through fusion (melting) or recrystallization of the base metal by applying heat, pressure or both. The most of significant advantage of welding is a wide variety of process embodiments, applicable to many materials, and manual or automated operation. Aside from the benefits, this process does have its disadvantages such as heat of welding degrades base properties, unbalanced heat input leads to distortion or residual stresses, requires considerable operator skill and complex automated welding systems, along with aforementioned specialized applications can lead to high cost. Also, conventional welding processes may not be suitable for joining thin stainless steel sheets and may make it difficult to accommodate the recent industry trends of using thinner sheet materials for weight reduction.
- Brazing and soldering are a metal-joining process in which workpieces are joined by melting of a filler material without melting of the workpieces (or base metal). The advantages of brazing are low temperature, permanent or temporary joining, dissimilar materials can be joined, speed with less chance of damage, and parts of varying thickness can be joined (Steward et al., 2000; Wu et al., 2000; Shiue et al., 2002; Khorram and Ghoreishi, 2015). However, these techniques with conventional heat source still have the drawbacks such as overheating, easily make fires, require proper workpiece sizes, lack of temperature control, and incomplete penetration.
- Hot and warm forming are conventional technologies to formed of an alloy at elevated temperature (Karbasiyan and Tekkaya, 2010; Bong et al., 2013). The main advantages of these techniques: decreasing the flow stress, increasing the formability of metal, reducing the springback, and the possibility produce the complex components (Karbasiyan and Tekkaya, 2010). Drawbacks of using this technique include large energy consumption, high cost, increased adhesion between the die and workpiece, reduced effect of lubrication, and lower dimensional accuracy due to uneven thermal expansion resulting from temperature

gradients within the material. Moreover, a rougher surface finish (resulting from an oxide layer developing on the outside of the part) is another consequence of using this process.

- Fluid forming technique has been using in automotive and aerospace industries. This method employs fluids to plastically deform a given blank material into the desired shape. Particularly, tube hydroforming with various cross-sectional shapes along the tube axis is a well-known and widely used technology for mass production, due to the improvement in computer controls and high pressure hydraulic systems (Anderson et al., 2013; Thanakijkasem et al., 2014). However, this method also encounters some disadvantages including low dimensional accuracy, wrinkling, slow cycle time and high capital investment.
- Electromagnetic forming (EMF) is a non-contact forming technique performed by electromagnetic forces with a high velocity at room temperature (Psyk et al., 2011; Gayakwad et al., 2014). The high forming rate of steel sheets enables the sheet to be stretched without fracturing (Andersson and Syk, 2008; Zhao et al., 2015). In addition to enhanced formability, the process also reduces springback and wrinkling of the sheet during the forming process. This method can be applied directly to high conductivity materials, e.g., aluminum and magnesium alloys. This technology is still being developed in the lab environment for sheet metal forming.
- Incremental forming process is a type of manufacturing process in which a metallic part is deformed into the final workpiece by a series a small incremental deformation (Chezhian Babu and Senthil Kumar, 2012; Moayedfar et al., 2014). This type of manufacturing is especially beneficial when forming brittle sheet metals and is used in the automotive and aircraft industries. The major advantages to this process are the large amounts of deformation and the decrease in the required deformation forces that can be obtained. These advantages are possible because of the minor heat treatments performed between the

increments of deformation. The treatments eliminate the effects of cold work or strain hardening by causing recrystallization to occur during each process anneal, thus resulting in a new, overall weaker material. However, this process has some disadvantages such as a big downfall is the potential for low-dimensional accuracy, since the part must be continuously removed, and refixed before and after the heat treatments. The decreased accuracy arises from the fact that the part may not be fixtured in the exact fashion each time it is removed and reinstalled. Also, this process can be long time-consuming, depending on the variables such as the number of heat treatments and their respective durations, as well as the depth of the desired deformations. Incremental forming may not be an optimum process for high production or high precision manufacturing.

- Preform annealing is two- or multiple-step forming process that includes an annealing heat treatment between initial and final forming operations (Krajewski, 2005). The preform annealing restores the ductility of single phase alloys partially (or entirely) after cold work (at first forming stage) through static recovery, recrystallization and grain growth. There is limited research on how preforming and annealing affect the material properties subjected to different prestrain and annealing conditions. Another issue is that the preform annealing needs a cost-effective heating method to reduce cycle time.

To overcome these problems of all above processing techniques, the EAM technique can be suggested as a promising technique for manufacturing processes. In this process, electric current is passed through a metal workpiece. The effects induced by electric current have been defined as electroplasticity (Okazaki et al., 1978; Conrad, 2000a). By properly utilizing the electroplasticity behaviors of metals, EAM is expected to reduce the process time and manufacturing cost in various conventional manufacturing processes such as sheet metal forming and joining. Since the 1960s, researchers have studied the effects of electroplasticity, which can be simply described as the passage of electric current through a material. Troitskii

pioneered the topic and applied the electroplasticity technique to many highly deformed metals (Troitskii, 1969). Subsequent electroplasticity studies have been carried out on a variety of metals and alloys including copper (Conrad et al., 1983, 1988), tin-lead alloys (Barnak et al., 1995), steels (Jones and Mears, 2011; Kim et al., 2014b; Thien et al., 2016a, 2016b; Park et al., 2017), titanium alloys (Jones and Mears, 2011; Stepanov et al., 2012; Sun et al., 2015), magnesium alloys (Jeong et al., 2017; Kim et al., 2017b; Park et al., 2017), aluminum alloys (Stepanov et al., 2012; Kim et al., 2014a; Hong et al., 2015), and metallic glass of various compositions (Cao et al., 2013). Throughout research studies, many different electroplasticity effects have been observed. The enhancement of intermetallic compounds was promoted when the electric current was applied to the interface between Sn/Cu, Sn/Ni, Al/Ni, Zn/Ni, and Bi/Ni (Su et al., 1997; Liu et al., 1998; Chen and Chen, 2000; Wang et al., 2011). An accelerated microstructural recrystallization process is consistently reported across a range of metallic materials, generally stemming from an enhanced nucleation rate, which leads to phase transformation and varying degrees of grain refinement (Conrad et al., 1983, 1984, 1988; Conrad, 2000b; Kim et al., 2014a; Park et al., 2017; Jeong et al., 2017). Changes to the mechanical properties associated with altered microstructure are also well documented (Kim et al., 2014b; Stepanov et al., 2012; Roh et al., 2014).

While a clear explanation of the atomic-level mechanism of electroplasticity is still being discussed, attempts to utilize the thermal/athermal effects of electric current in various manufacturing processes have been reported (Nguyen-Tran et al., 2015; Ruszkiewicz et al., 2017). Electrically assisted friction stir welding (EAFSW) was suggested as a new method for easy maintenance and flexible applications. The Z-axis force of EAFSW is decreased more significantly than that of the conventional process and the weld speed and power consumption are improved (Pitschman et al., 2010). Xu et al. (2014) suggested an electrically assisted solid-state pressure welding process of 316 stainless steel and reported that the maximum shear

strength was achieved with increased current density. Wang (2009) and Xie et al. (2016) suggested a schematic for the EA deep drawing process using a pulsed electric current. The lower resistance to deformation, better plasticity, improved ductility, dynamical recrystallization grains at low temperature, and low energy consumption are the advantages of the EA deep drawing process. Kim et al. (2014c) studied electrically assisted blanking, which exploits the electroplasticity of ultra-high strength steel. Their experimental results showed that the blanking load of electrically assisted blanking was clearly lower than that of blanking immediately after local resistance heating. Asghar et al. (2013) successfully formed a titanium alloy using an EA double-side incremental forming process. The pulsed electric current applied to the part of tools can greatly improve the forming limits of incremental forming parts and probably allow the formation of exotic materials. Ti6Al4V, which can only be formed at temperatures of 900-930°C, was successfully formed by applying a pulsed electric current at 47°C to a tool-sheet interface. Its force and the distortion of shape were reduced compared to those in the traditional process. In addition, electrically assisted tools ensure that the zone of current conduction is as small as possible in order to enhance the formability due to electroplasticity. Baranov et al. (2011) suggested an electroplasticity metal cutting process and reported that the friction force and processing time were significantly reduced by applying a pulsed electric current.

In the present study, electrically assisted (EA) joining and forming of stainless steels is experimentally investigated. Note that chapter II and III are presented as two independent journal papers, which have been published, chapter IV is prepared as a journal paper for publication, and chapter V is presented as industrial applications. Therefore, some parts of the introductions and the description of the experimental set-up are repeated in these chapters.

In chapter II, we explored the unique features of electrically assisted brazing of ferritic stainless steels using a nickel-based filler metal. Two test fixtures were designed such that two

different heat sources can be applied to brazing joints. The microstructural and mechanical properties of the electrically assisted brazing joints were experimentally compared with those of induction brazing. Athermal effects of the electric current in electrically assisted brazing are discussed based on the experimental results.

In chapter III, we investigate the effect of a single pulse of electric current on the mechanical behavior and microstructure of a commercially available 316L austenite stainless steel (SUS316L). Specifically, the goal of the present study is to evaluate the feasibility of a two-stage forming process of the selected SUS316L with rapid EA annealing. At the first stage, a tensile specimen is performed to a specific prestrain and then annealed by applying a single pulse of electric current with a short duration time. Finally, the specimen is reloaded until fracture at the second stage. Two different prestrain levels (20 and 60%) were combined in parameter study with three different true electric current densities (95, 100, and 105 A/mm²) and a constant electric current duration of 0.75 sec. Both effects of the applied current density and the magnitude of prestrain on the tensile behavior are reported.

In chapter IV, we investigate the effect of EA subsecond annealing on mechanical properties and microstructure of a commercial available 304 austenite stainless steel (SUS304). The experiments of this work employ the same testing system as the previous work in chapter III. The post-annealing tensile behavior of two different prestrains is compared with each other by applying the same current densities. Based on the experimental results, the effects of prestrain and electric current are also investigated. The phase transformations before and after EA subsecond annealing are also discussed.

In chapter V, the industrial applications are demonstrated based on the experimental data and theories in chapter II, III, IV. Both EA joining and EA forming processes are applied to the development of EA brazing exhaust systems and EA springback reduction bipolar plates for fuel cell in the automotive industry.

References

- Anderson, M., Gholipour, J., Bridier, F., Bocher, P., Jahazi, M., Savoie, J., Wanjara, P., 2013. Improving the Formability of Stainless Steel 321 through Multistep Deformation for Hydroforming. *Transactions of the Canadian Society for Mechanical Engineering* 37, 39–52.
- Andersson, R., Syk, M., 2008. Electromagnetic Pulse Forming of Carbon Steel Sheet Metal. Presented at the 3rd International Conference on High Speed Forming, 233–244.
- Asghar, J., Reddy, N.V., 2013. Importance of Tool Configuration in Incremental Sheet Metal Forming of Difficult to Form Materials Using Electro-Plasticity. Presented at the World Congress on Engineering, WCE 2013, London; United Kingdom, 1734–1738.
- Baranov, S.A., Staschenko, V.I., Sukhov, A.V., Troitskiy, O.A., Tyapkin, A.V., 2011. Electroplastic metal cutting. *Russian Electrical Engineering* 82, 477–479.
- Barnak, J.P., Sprecher, A.F., Conrad, H., 1995. Colony (grain) size reduction in eutectic Pb-Sn castings by electroplusing. *Scripta Metallurgica et Materialia* 32, 879–884.
- Bong, H.J., Barlat, F., Ahn, D.C., Kim, H.-Y., Lee, M.-G., 2013. Formability of austenitic and ferritic stainless steels at warm forming temperature. *International Journal of Mechanical Sciences* 75, 94–109.
- Cao, X.D., Kim, B.H., Chu, C.N., 2013. Hybrid micromachining of glass using ECDM and micro grinding. *International Journal of Precision Engineering and Manufacturing* 14, 5–10.
- Chen, C.-M., Chen, S.-W., 2000. Electromigration effect upon the Zn/Ni and Bi/Ni interfacial reactions. *Journal of Electronic Materials* 29, 1222–1228.
- Chezian Babu, S., Senthil Kumar, V.S., 2012. Experimental studies on incremental forming of stainless steel AISI 304 sheets. *Proceedings of the Institution of Mechanical Engineers, Part B: Journal of Engineering Manufacture* 226, 1224–1229.

- Conrad, H., 2000a. Electroplasticity in metals and ceramics. *Materials Science and Engineering: A* 287, 276–287.
- Conrad, H., 2000b. Effects of electric current on solid state phase transformations in metals. *Materials Science and Engineering: A* 287, 227–237.
- Conrad, H., Karam, N., Mannan, S., 1984. Effect of prior cold work on the influence of electric current pulses on the recrystallization of copper. *Scripta Metallurgica* 18, 275–280.
- Conrad, H., Karam, N., Mannan, S., 1983. Effect of electric current pulses on the recrystallization of copper. *Scripta Metallurgica* 17, 411–416.
- Conrad, H., Karam, N., Mannan, S., Sprecher, A.F., 1988. Effect of electric current pulses on the recrystallization kinetics of copper. *Scripta Metallurgica* 22, 235–238.
- Correa, E.O., Barbosa, R.P., Buschinelli, A.J.A., Silva, E.M., 2010. Influence of Clad Metal Chemistry on Stress Corrosion Cracking Behaviour of Stainless Steels Claddings in Chloride Solution. *Engineering* 2, 391.
- Follansbee, P.S., 2015. Structure Evolution in Austenitic Stainless Steels. *Materials Sciences and Applications* 6, 457-463.
- Gayakwad, D., Dargar, M.K., Sharma, P.K., purohit, R., Rana, R.S., 2014. A Review on Electromagnetic Forming Process. *Procedia Materials Science*, 3rd International Conference on Materials Processing and Characterisation 6, 520–527.
- Geijselaers, H.J.M., Perdahcioğlu, E.S., 2009. Mechanically induced martensitic transformation as a stress-driven process. *Scripta Materialia* 60, 29–31.
- Gideon, B., Ward, L., Biddle, G., 2008. Duplex Stainless Steel Welds and their Susceptibility to Intergranular Corrosion. *Journal of Minerals and Materials Characterization and Engineering* 7, 247-263.

- Hong, S.-T., Jeong, Y.-H., Chowdhury, M.N., Chun, D.-M., Kim, M.-J., Han, H.N., 2015. Feasibility of electrically assisted progressive forging of aluminum 6061-T6 alloy. *CIRP Annals* 64, 277–280.
- Huang, G.L., Matlock, D., Krauss, G., 1989. Martensite formation, strain rate sensitivity, and deformation behavior of type 304 stainless steel sheet. *Metallurgical Transactions* 20A, 1239–1246.
- Jeong, H.-J., Kim, M.-J., Park, J.-W., Yim, C.D., Kim, J.J., Kwon, O.D., Madakashira, P.P., Han, H.N., 2017. Effect of pulsed electric current on dissolution of Mg 17 Al 12 phases in as-extruded AZ91 magnesium alloy. *Materials Science and Engineering: A* 684, 668–676.
- Jones, J.J., Mears, L., 2011. Constant Current Density Compression Behavior of 304 Stainless Steel and Ti-6Al-4V During Electrically-Assisted Forming. *The American Society of Mechanical Engineering* 1, 629–637.
- Karbasian, H., Tekkaya, A.E., 2010. A review on hot stamping. *Journal of Materials Processing Technology* 210, 2103–2118.
- Khorram, A., Ghoreishi, M., 2015. Comparative study on laser brazing and furnace brazing of Inconel 718 alloys with silver based filler metal. *Optics & Laser Technology* 68, 165–174.
- Kim, K.-H., Bang, Han-Sur, Ro, C.-S., Bang, Hee-Seon, 2017a. Influence of preheating source on mechanical properties and welding residual stress characteristics in ultra thin ferritic stainless steel hybrid friction stir welded joints. *International Journal of Precision Engineering and Manufacturing-Green Technology* 4, 393–400.
- Kim, M.-J., Lee, K., Oh, K.H., Choi, I.-S., Yu, H.-H., Hong, S.-T., Han, H.N., 2014a. Electric current-induced annealing during uniaxial tension of aluminum alloy. *Scripta Materialia* 75, 58–61.

- Kim, M.-J., Lee, M.-G., Hariharan, K., Hong, S.-T., Choi, I.-S., Kim, D., Oh, K.H., Han, H.N., 2017b. Electric current–assisted deformation behavior of Al-Mg-Si alloy under uniaxial tension. *International Journal of Plasticity* 94, 148–170.
- Kim, M.-S., Vinh, N.T., Yu, H.-H., Hong, S.-T., Lee, H.-W., Kim, M.-J., Han, H.N., Roth, J.T., 2014b. Effect of electric current density on the mechanical property of advanced high strength steels under quasi-static tensile loads. *International Journal of Precision Engineering and Manufacturing* 15, 1207–1213.
- Kim, W., Yeom, K.-H., Thien, N.T., Hong, S.-T., Min, B.-K., Ik Oh, S., Kim, M.-J., Han, H.N., Lee, H.-W., 2014c. Electrically assisted blanking using the electroplasticity of ultra-high strength metal alloys. *CIRP Annals* 63, 273–276.
- Krajewski, P., 2005. Method for production of stamped sheet metal panels. US20050199032A1.
- Liu, W.-C., Chen, S.-W., Chen, C.-M., 1998. The Al/Ni interfacial reactions under the influence of electric current. *Journal of Electronic Materials* 27, L6–L9.
- Michael F. McGuire, 2008. *Stainless Steels for Design Engineers* - ASM International.
- Moayedfar, M., Leman, Z., bin Baharudin, B.T.H.T., 2014. Incremental Sheet Forming (ISF) of AISI 316 Stainless Steel Sheet Using CNC Milling Machine. *Advanced Materials Research* 939, 322-327.
- Mohandas, T., Madhusudhan Reddy, G., Naveed, M., 1999. A comparative evaluation of gas tungsten and shielded metal arc welds of a “ferritic” stainless steel. *Journal of Materials Processing Technology* 94, 133–140.
- Nguyen-Tran, H.-D., Oh, H.-S., Hong, S.-T., Han, H.N., Cao, J., Ahn, S.-H., Chun, D.-M., 2015. A review of electrically-assisted manufacturing. *International Journal of Precision Engineering and Manufacturing-Green Technology* 2, 365–376.
- Okazaki, K., Kagawa, M., Conrad, H., 1978. A study of the electroplastic effect in metals. *Scripta Metallurgica* 12, 1063–1068.

- Olaseinde, O.A., Merwe, J.V. der, Cornish, L., 2013. Characterization and Corrosion Behaviour of Selected Duplex Stainless Steels in Acidic and Acidic-Chloride Solution. *Advances in Chemical Engineering and Science* 4, 89-93.
- Park, J.-W., Jeong, H.-J., Jin, S.-W., Kim, M.-J., Lee, K., Kim, J.J., Hong, S.-T., Han, H.N., 2017. Effect of electric current on recrystallization kinetics in interstitial free steel and AZ31 magnesium alloy. *Materials Characterization* 133, 70–76.
- Peterson, S.F., Mataya, M.C., Matlock, D.K., 1997. The formability of austenitic stainless steels. *The Journal of The Minerals, Metals & Materials Society* 49, 54–58.
- Pitschman, M., Dolecki, J.W., Johns, G.W., Zhou, J., Roth, J.T., 2010. Application of Electric Current in Friction Stir Welding 185–189.
- Psyk, V., Risch, D., Kinsey, B.L., Tekkaya, A.E., Kleiner, M., 2011. Electromagnetic forming- A review. *Journal of Materials Processing Technology, Special Issue: Impulse Forming* 211, 787–829.
- Rocha, M.R. da, Oliveira, C.A.S. de, 2009. Evaluation of the martensitic transformations in austenitic stainless steels. *Materials Science and Engineering: A* 517, 281–285.
- Roh, J.-H., Seo, J.-J., Hong, S.-T., Kim, M.-J., Han, H.N., Roth, J.T., 2014. The mechanical behavior of 5052-H32 aluminum alloys under a pulsed electric current. *International Journal of Plasticity* 58, 84–99.
- Ruszkiewicz, B.J., Grimm, T., Ragai, I., Mears, L., Roth, J.T., 2017. A Review of Electrically-Assisted Manufacturing With Emphasis on Modeling and Understanding of the Electroplastic Effect. *Journal of Manufacturing Science and Engineering* 139, 110801.
- Shiue, R.K., Wu, S.K., Hung, C.M., 2002. Infrared repair brazing of 403 stainless steel with a nickel-based braze alloy. *Metallurgical and Materials Transactions A* 33, 1765–1773.

- Stepanov, G.V., Babutskii, A.I., Chizhik, A.V., Gromov, V.E., 2012. Pulse electric current effect on mechanical properties of titanium aluminide produced by the self-propagating high-temperature synthesis technique. *Strength Mater* 44, 636–644.
- Steward, R., Grossbeck, M., Chin, B., Aglan, H., Gan, Y., 2000. Furnace brazing type 304 stainless steel to vanadium alloy (V–5Cr–5Ti). *Journal of Nuclear Materials* 283–287, 1224–1228.
- Su, L.-H., Yen, Y.-W., Lin, C.-C., Chen, S.-W., 1997. Interfacial reactions in molten Sn/Cu and molten In/Cu couples. *Metallurgical and Materials Transactions B* 28, 927–934.
- Sun, Y., Haley, J., Kulkarni, K., Aindow, M., Lavernia, E.J., 2015. Influence of electric current on microstructure evolution in Ti/Al and Ti/TiAl₃ during spark plasma sintering. *Journal of Alloys and Compounds* 648, 1097–1103.
- Takakuwa, O., Soyama, H., 2014. Effect of Residual Stress on the Corrosion Behavior of Austenitic Stainless Steel. *Advances in Chemical Engineering and Science* 5, 62.
- Thanakijkasem, P., Uthaisangsuk, V., Pattarangkun, A., Mahabunphachai, S., 2014. Effect of bright annealing on stainless steel 304 formability in tube hydroforming. *The International Journal of Advanced Manufacturing Technology* 73, 1341–1349.
- Thien, N.T., Hong, S.-T., Kim, M.-J., Han, H.N., Yang, D.-H., Lee, H.-W., Lee, K., 2016a. Electrically assisted bake hardening of complex phase ultra-high strength steels. *International Journal of Precision Engineering and Manufacturing* 17, 225–231.
- Thien, N.T., Jeong, Y.-H., Hong, S.-T., Kim, M.-J., Han, H.N., Lee, M.-G., 2016b. Electrically assisted tensile behavior of complex phase ultra-high strength steel. *International Journal of Precision Engineering and Manufacturing-Green Technology* 3, 325–333.
- Troitskii, O.A., 1969. Electromechanical Effect in Metals. *ZhETF Pisma Redaktsiui* 10, 18.

- Umoru, L.E., Afonja, A.A., Ademodi, B., 2008. Corrosion Study of AISI 304, AISI 321 and AISI 430 Stainless Steels in a Tar Sand Digester. *Journal of Minerals and Materials Characterization and Engineering* 7, 291-299.
- Wang, C.-H., Kuo, C., Chen, H., Chen, S., 2011. Effects of current density and temperature on Sn/Ni interfacial reactions under current stressing. *Intermetallics* 19, 75–80.
- Wang Shao Zuo, 2009. Effect of Electric Pulses on Drawability and Corrosion Property of AZ31 Magnesium Alloy. Master's Thesis Dissertation.
- Wu, X., Chandel, R.S., Pheow, S.H., Li, H., 2000. Brazing of Inconel X-750 to stainless steel 304 using induction process. *Materials Science and Engineering: A* 288, 84–90.
- Xie, H., Dong, X., Ai, Z., Wang, Q., Peng, F., Liu, K., Chen, F., Wang, J., 2016. Experimental investigation on electrically assisted cylindrical deep drawing of AZ31B magnesium alloy sheet. *The International Journal of Advanced Manufacturing Technology* 86, 1063–1069.
- Xu, Z., Peng, L., Lai, X., 2014. Electrically assisted solid-state pressure welding process of SS 316 sheet metals. *Journal of Materials Processing Technology* 214, 2212–2219.
- Zhao, Q., Wang, C., Xu, J., Shan, D., Guo, B., 2015. Study of micro electromagnetic bulging on a stainless steel foil. *Manufacturing Review* 2, 7.

CHAPTER II

DIFFUSION ENHANCEMENT DURING ELECTRICALLY ASSISTED BRAZING OF FERRITIC STAINLESS STEEL ALLOYS

ABSTRACT

The electrically assisted brazing of a ferritic stainless steel with nickel-based filler metal is experimentally investigated. During electrically assisted brazing of a lap joint, the temperature of the joint is first rapidly increased to a brazing temperature and held nearly constant for a specific period using a pulsed electric current. Microstructural analysis results strongly suggest that the electric current during electrically assisted brazing enhances diffusion between the filler metal and the ferritic stainless steel, thus inducing significantly thicker diffusion zones compared with induction brazing. The mechanical test results show that the strength of the electrically assisted brazing joint is comparable to or even superior to those of the joint fabricated by induction brazing, while the process time of the electrically assisted brazing is significantly shorter than that of induction brazing.

Keywords: electrically assisted; brazing; diffusion; stainless steels

2.1 INTRODUCTION

Ferritic stainless steels are widely used in automotive industries, especially for exhaust systems including manifolds, catalytic converters, mufflers, and tail pipes. Ferritic stainless steels are well known for their excellent stress corrosion cracking resistance, adequate high temperature resistance to oxidation, good weldability, and good forming characteristics (Mohandas et al., 1999; Kim et al., 2017a). However, the heat generated during conventional fusion welding processes of these stainless steels may lead to grain coarsening in the welded region, since they directly solidify from a liquid phase to the ferrite phase without any intermediate phase transformation (Taban et al., 2009; Yang and Chen, 2013). Grain coarsening in the welded region may reduce the toughness, ductility, and corrosion resistance of the joint. Also, conventional fusion welding processes may not be suitable for joining thin stainless steel sheets and may make it difficult to accommodate the recent industrial trends of using thinner sheet materials for weight reduction.

Brazing is a metal-joining process in which workpieces are joined by melting and solidifying a filler material without melting the workpieces. Since brazing does not require melting the workpieces, very thin metal sheets that are less than a millimeter in thickness can be easily joined by brazing. The brazing of stainless steel sheets has been frequently studied (Lugscheider, 1983; Wu et al., 2000; Shiue et al., 2002; Ou et al., 2006). Shiue et al. (2002) studied the infrared brazing of 403 martensitic stainless steel with a nickel (Ni)-based braze alloy, and they achieved a joint strength close to 300 MPa with brittle failure. Ou et al. (2006) studied infrared brazing of 422 stainless steel using a BNi-2 braze alloy as a filler metal; they observed a decrease in the shear strength of the brazed joint with increasing brazing temperature and/or time. Wu et al. (2000) investigated induction brazing of Inconel X-750 to stainless steel 304 and reported that the width of the braze-affected zone increased with increasing joining time. Lugscheider et al. (1983) studied the brazing of 316 stainless steel with

BNi-2, BNi-5 and BNi-7 filler metals to determine the effects of brazing temperature, time, post-braze heat treatment, and brazing clearance on the metallurgical quality and tensile strength of the joints. They reported that the 316 stainless steel braze joint with BNi-5 filler metal showed the maximum joint strength.

While various heat sources are available for successful brazing of stainless steels as mentioned above, the resistance heating can also be a very effective heat source for brazing. The effectiveness of resistance heating as a heat source for brazing may be accompanied by the benefits of rapid heating and the possibility of additional athermal effects associated with the electric current. Specifically, the electric current may induce the electroplasticity, wherein the electric current enhances the mobility of atoms in addition to the well-known effect of elevated temperature by resistance heating (Conrad, 2000a; Li et al., 2008; Kim et al., 2014a; Kim et al., 2014b; Nguyen-Tran et al., 2015; Thien et al., 2016a; Oh et al., 2016). While a clear explanation of the atomic-level mechanism of electroplasticity is still being discussed, attempts to utilize the thermal/athermal effects of electric current in various manufacturing processes (electrically assisted manufacturing: EAM) have been reported (Nguyen-Tran et al., 2015). For example, Xu et al. (2014) suggested an electrically assisted solid-state pressure welding process of 316 stainless steel and reported that the maximum shear strength was achieved with increased current density. Kim et al. (2014c) studied electrically assisted blanking, which exploits the electroplasticity of ultra-high strength steel. Their experimental results showed that the blanking load of electrically assisted blanking was clearly lower than that of blanking immediately after local resistance heating. Baranov et al. (2011) suggested an electroplastic metal cutting process and reported that the friction force and processing time were significantly reduced by applying a pulsed electric current. It also needs to be mentioned that under certain process conditions, the results for some selected EAMs have been described without considering the athermal effects of electric current. For example, Ng et al. (2015) suggested

using electric current in the roll bonding process and used the joule heating effect to explain the result that electrically assisted roll bonding lowered rolling forces and increased the joint strength of bonded sheets.

In the present study, we explored the unique features of electrically assisted brazing of ferritic stainless steels using a nickel-based filler metal. In electrically assisted brazing, only the filler metal melts and solidifies, unlike conventional resistance spot welding. The microstructural and mechanical properties of the electrically assisted brazing joints were experimentally compared with those of induction brazing. Athermal effects of the electric current in electrically assisted brazing are discussed based on the experimental results.

2.2 EXPERIMENTAL SET-UP

In the present study, 436 ferritic stainless steel sheets with a thickness of 0.8 mm were used for the experiments. The chemical composition of the 436 ferritic stainless steel is listed in Table 1. Brazing specimens with a length of 100 mm and a width of 20 mm were fabricated from the ferritic stainless steel sheet by laser cutting along the rolling direction of the sheet. A nickel (Ni)-based filler metal (AMS 4777, Lucas-Milhaupt Incorporated, USA) film with a thickness of 76 μm was used for brazing, and its chemical composition is also listed in Table 2.1. The Ni-based filler metal film was cut to sizes of 20 mm x 20 mm and was placed at the interface of the two brazing specimens, while the overlap length of the two brazing specimens was fixed at 40 mm, as schematically shown in Figure 2.1(a). Two different heating methods, resistance heating (electrically assisted brazing) and induction heating (induction brazing), were used to fabricate lap joints via brazing. Note that the induced eddy current during induction heating is a surface phenomenon (or simply a skin effect) (Davies and Simpson, 1979). The thermal homogeneity during induction heating is mostly obtained by thermal conduction.

For electrically assisted brazing with resistance heating, a programmable welder (VADAL SP-1000U, Hyosung, South Korea) was used to apply an electric current to the specimens. A pair of copper electrodes was used to clamp the brazing specimens, and an electric current was applied through the joint of the specimens, as described in Figure 2.1(b). A custom made 25 kW induction brazing machine (SK brazing Corporation, South Korea) with a maximum frequency of 440 kHz was used for induction brazing. The assembly of brazing specimens with the Ni-based filler (Figure 2.1(a)) was placed inside an induction coil, as described in Figure 2.1(c).

A pulsed electric current was used for electrically assisted brazing. During electrically assisted brazing, the temperature of the assembly of brazing specimens with Ni-based filler (simply, the joint temperature) was rapidly increased to the brazing temperature ($\approx 1100^\circ\text{C}$) using the electric current, which had a magnitude of I_i and a duration of t_i . The joint temperature was then held nearly constant for an additional holding time t_h by periodically applying an electric current I_m with a duration of t_m and a period of μ_m , as schematically described in Figure 2.2(a). During induction brazing, the joint temperature also increased to the target value ($\approx 1100^\circ\text{C}$) and was then held nearly constant for a holding time t_h by the induction coil, as schematically described in Figure 2.2(b). The heating parameters for the electrically assisted brazing and the induction brazing are listed in Table 2.2. Note that for the zero holding time ($t_h = 0$ sec), the joint was simply cooled down to room temperature immediately after the joint temperature reached the target brazing temperature. During electrically assisted and induction brazing, the temperature history of the joint was measured using an infrared thermal imaging camera (T621, FLIR, Sweden), which was calibrated in separate preliminary experiments with a k-type thermocouple, and a k-type thermocouple, respectively.

After brazing, the cross-sectional samples were prepared along the width direction at the center of the joint for microstructural analysis. The cross-sectional samples were processed using a standard metallographic grinding and polishing procedure, and were finished with a 1 μm diamond suspension followed by electrical polishing with colloidal silica. The cross-sectional samples were first examined using a scanning electron microscope (SEM) to confirm that the brazing joint was successfully fabricated without any macroscopic defects with the heating parameters in Table 2. The microstructure was then observed using a field emission scanning electron microscope (FE-SEM: SU70, Hitachi, Japan) equipped with an electron backscatter diffraction system (EBSD: EDAX-TSL Hikari, USA) and an energy dispersive spectrometer (EDS: X-Max50, Horiba, Japan). Finally, the mechanical properties of the joint

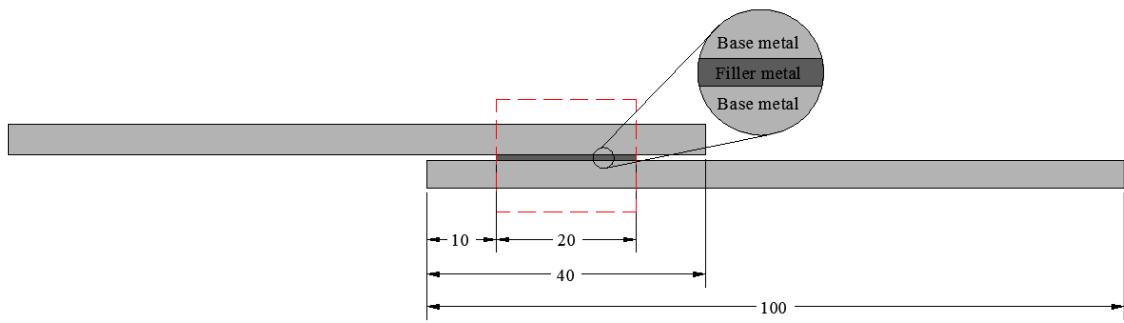
were evaluated by simple tensile lap-shear tests using a universal testing machine with a constant displacement rate of 2 mm/min.

Materials	Chemical composition (wt.%)										
	Fe	Cr	Si	B	Ni	N	P	C	S	Mo	Mn
436 ferritic stainless steel	Bal.	17.0 - 20.0	1.00	-	0.6	0.025	0.04	0.025	0.03	0.4 - 0.8	1
AMS 4777	3.0	7.0	4.5	3.1	Bal.	-	-	-	-	-	-

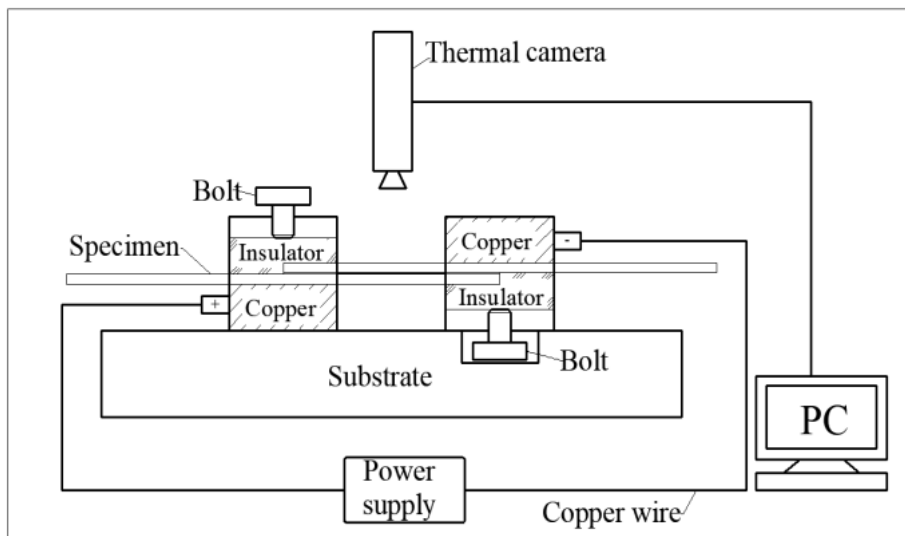
Table 2. 1 Chemical composition of ferritic stainless steel and filler material (AMS 4777)

Type	Electric current I_i (A)	Duration time t_i (sec)	Electric current I_m (A)	Period time μ_m (sec)	Duration time t_m (sec)
Electrically assisted brazing	2500	1.10	750	0.5	0.5
Induction brazing	Induction power (%)		Heating time (sec)		Holding time (sec)
	75		15		0, 10, 20

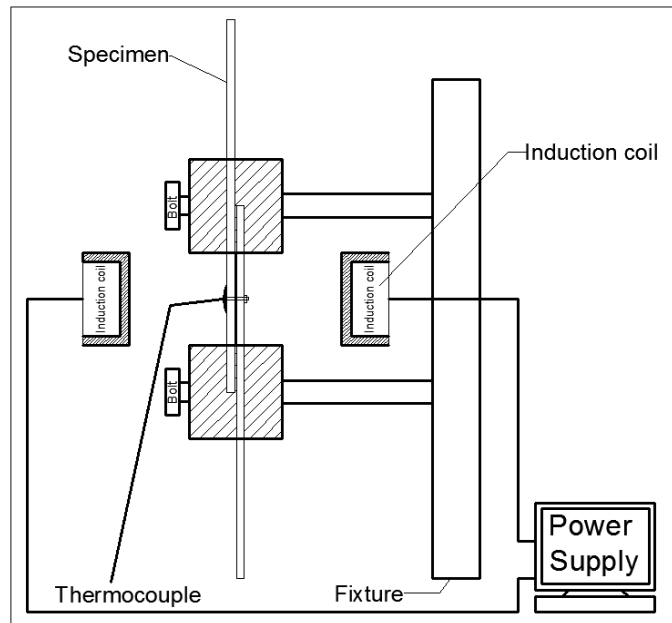
Table 2. 2 Heating parameters for electrically assisted brazing and induction brazing



(a)

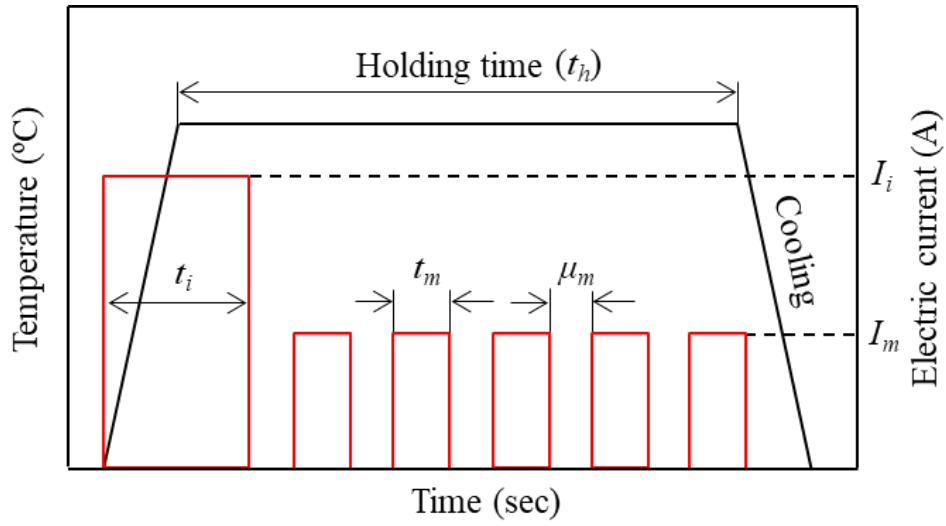


(b)

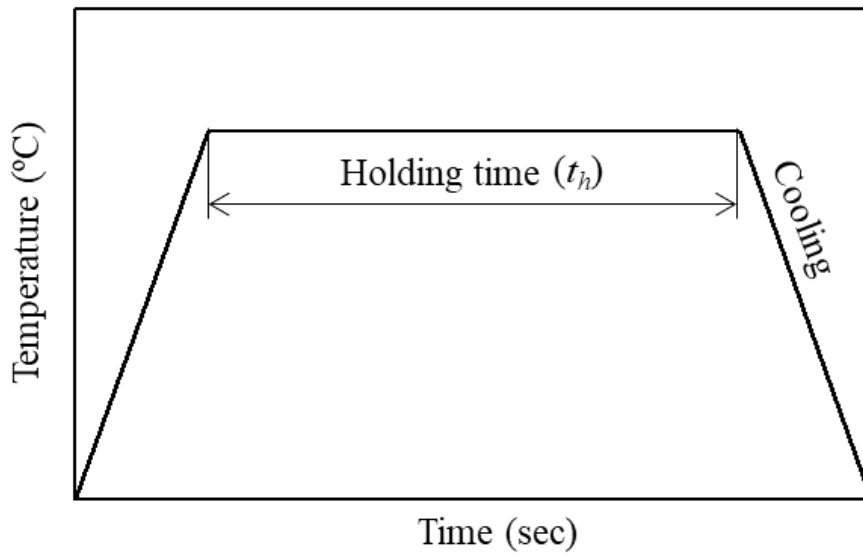


(c)

Figure 2. 1 (a) Schematic of brazing specimen and the experimental set-up for: (b) electrically assisted brazing and (c) induction brazing



(a)



(b)

Figure 2. 2 Schematic of temperature histories for (a) electrically assisted brazing and (b) induction brazing

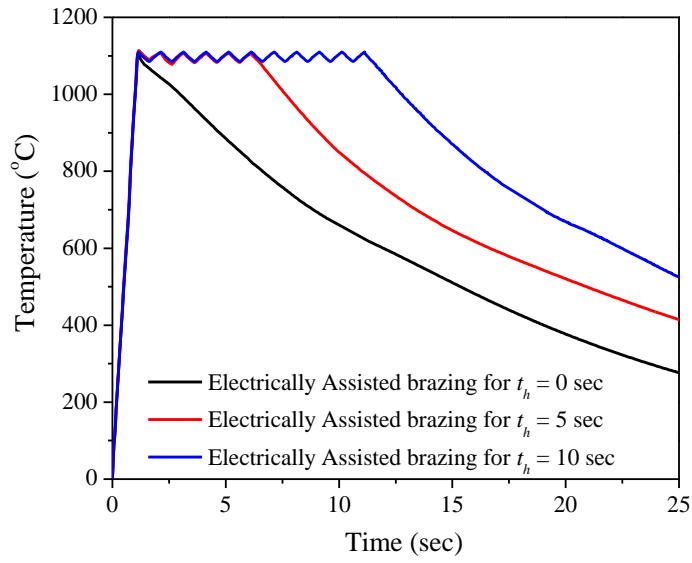
2.3 RESULTS AND DISCUSSION

The temperature histories during electrically assisted brazing show that the joint temperature rapidly reached the brazing temperature ($\approx 1100^\circ\text{C}$) and was held nearly constant during the remaining process time (Figure 2.3(a)). The temperature histories of the induction brazing are shown in Figure 2.3(b). Note that the time to reach the target brazing temperature was much longer for the induction brazing (approximately 15 sec) than for the electrically assisted brazing (1.1 sec). Therefore, for the same holding time t_h a higher amount of thermal energy was provided to the joint in induction brazing than in electrically assisted brazing even though the effect may not be significant, since the intensity of diffusion at temperatures below the liquidus of the filler metal would be relatively low.

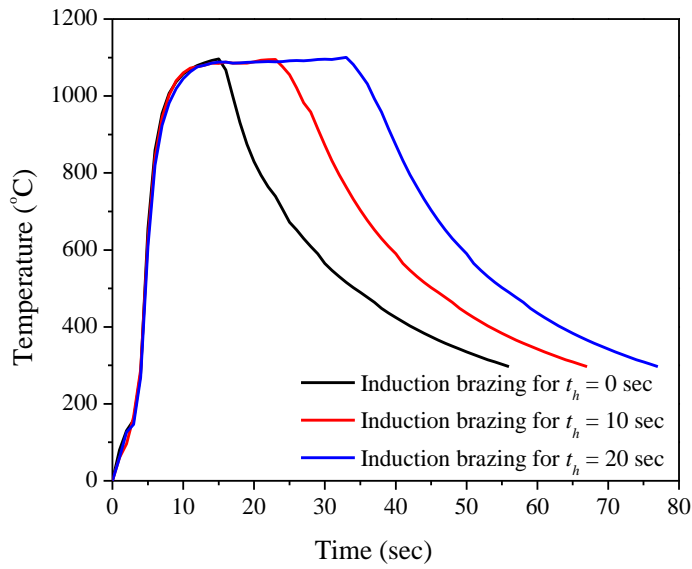
For both electrically assisted brazing and induction brazing, the 436 ferritic stainless steel specimens were successfully joined using the Ni-based filler metal without any visible porosity or macroscopic defects, even for $t_h = 0$ sec, as shown in the SEM images of the cross-sections of the joints (Figure 2.4(a)). As marked in Figures 2.4(a) and (b), it was observed that all the brazing joints consist of three distinctively different zones, i.e., the base metals, the diffusion zone (or transition zone), and the interlayer (or the filler metal). The SEM images of the interlayer show bright and dark phases for all the electrically assisted and induction brazing joints (Figure 2.4(c)). The results of EDS point scan analysis on the bright and dark phases in the interlayer reveal that the bright phase is primarily composed of Ni (~ 44 wt%) and Fe (~ 40 wt%) with different alloying element concentrations, while the dark phase is composed of B (~ 15 wt%), Cr (~ 37 wt%), Fe (~ 36 wt%), and a smaller amount of Ni (~ 8.5 wt%). It is interesting to note that both bright and dark phases are Fe rich, which indicates the dissolution of Fe from the ferritic stainless steel base metal into the molten brazing filler metal during

brazing. A further discussion on the microstructure of the interlayer is outside the scope of the present study. The microstructures of the interlayer of brazing joints of stainless steels with Ni-based filler metal have been discussed in the open literature (Shiue et al., 2002; Ou et al., 2006).

The thickness of the diffusion zone can be approximated by the distribution of major alloying elements across the interface between the interlayer and the base metal through the EDS line scan. As expected, the EDS line scan results of four different alloying elements (Fe, Cr, Ni, and Si) show that the concentrations of those elements gradually change within the diffusion zone for all the brazing joints (Figure 2.5). In the present study, the concentration curve of Ni, which is the major alloying element of the filler metal, was used to measure the thickness of the diffusion zone (Figure 2.6). The thickness of the diffusion zone was measured by measuring the distance from the last peak of the concentration curve of Ni prior to the rapid decrease to the point of average Ni intensity of the 436 ferritic stainless steel, as schematically marked in Figure 2.6(a). The diffusion zone thicknesses were measured on both the top and bottom sides of the interlayer for each specimen. Note that some fluctuations in the concentration curve of Ni were found in the interlayer zone. This is attributed to the two different Ni rich (bright) and Ni poor (dark) phases in the interlayer zone as marked in Figure 2.4(c).

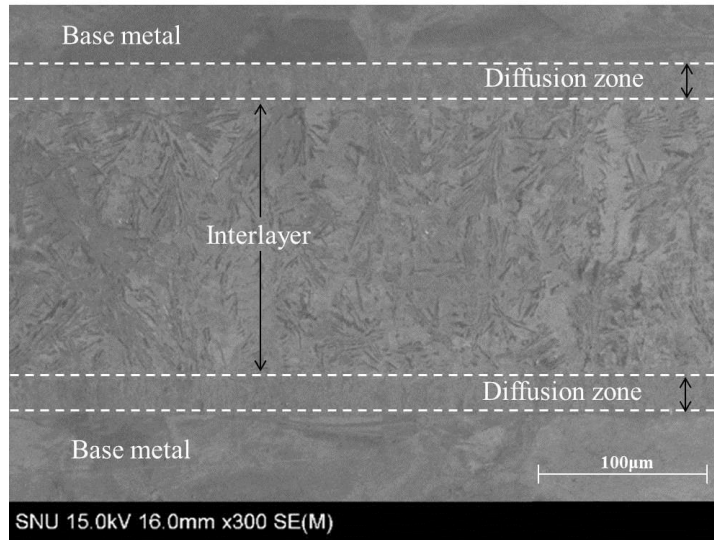


(a)

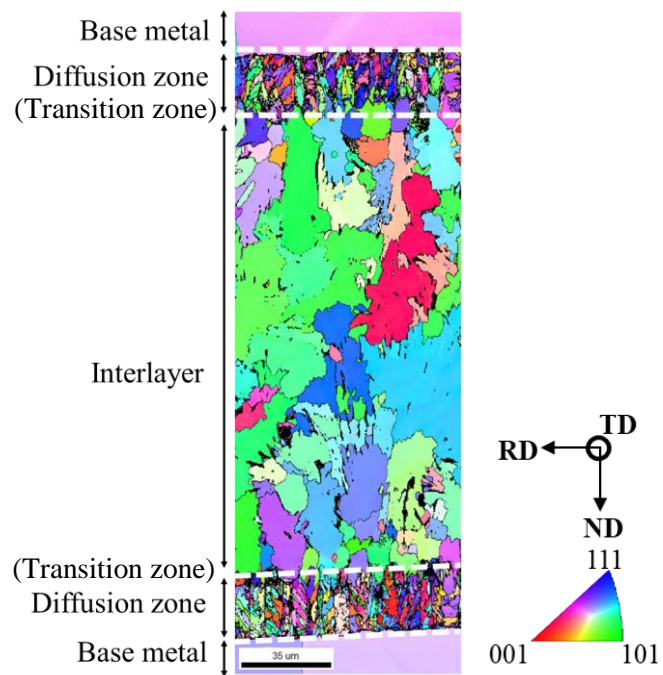


(b)

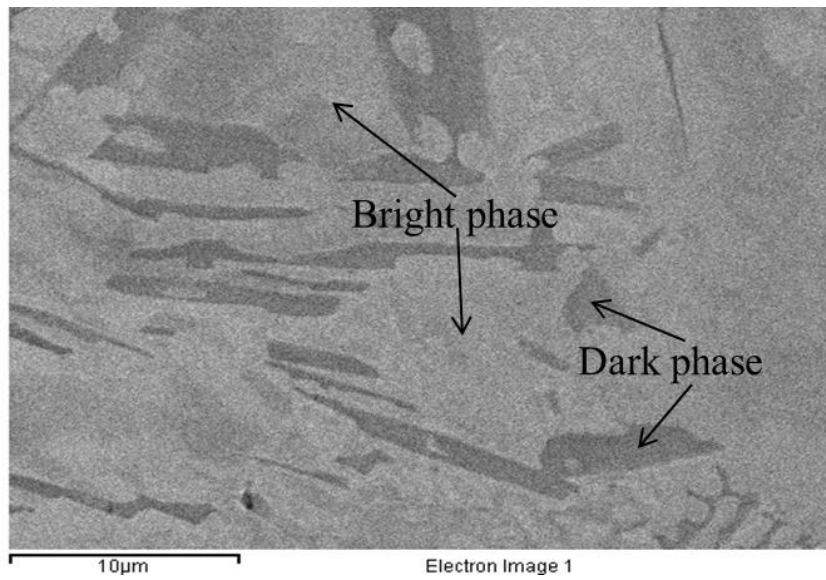
Figure 2. 3 Temperature histories of (a) electrically assisted brazing and (b) induction brazing for various brazing conditions



(a)

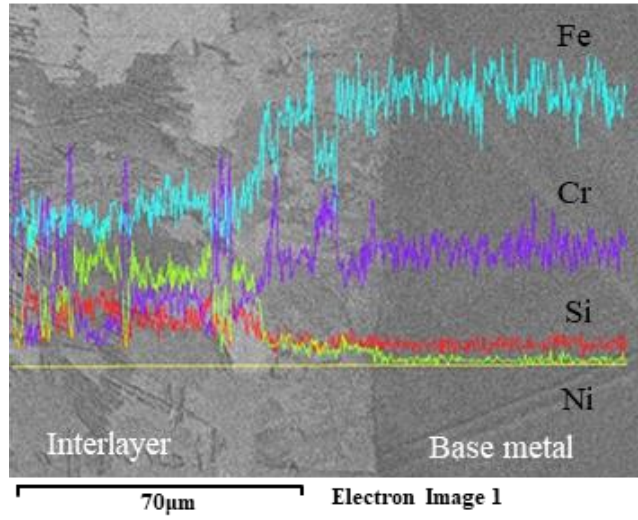


(b)

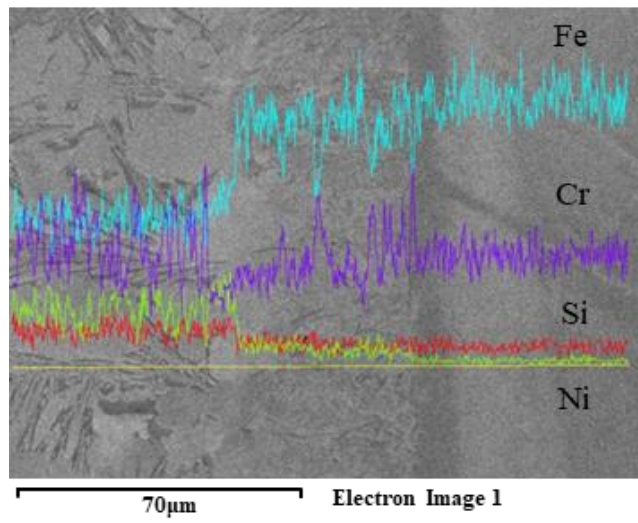


(c)

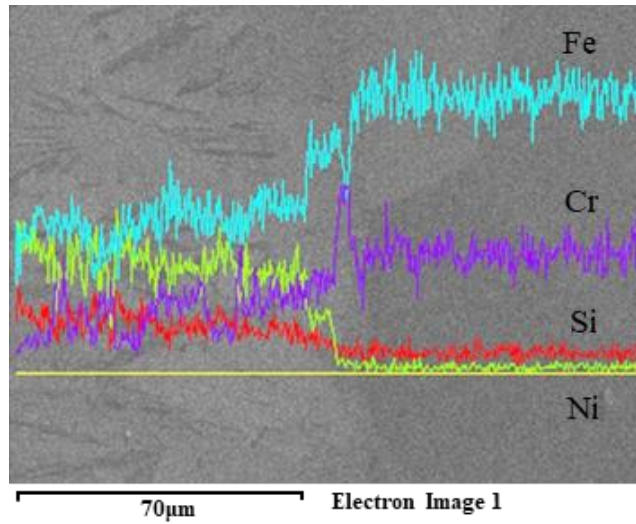
Figure 2. 4 Cross-sectional images: (a) SEM micrograph of electrically assisted brazing ($t_h = 0$ sec), (b) EBSD inverse pole (IPF) map of electrically assisted brazing ($t_h = 5$ sec), and (c) SEM micrograph of interlayer (filler metal) of electrically assisted brazing ($t_h = 0$ sec)



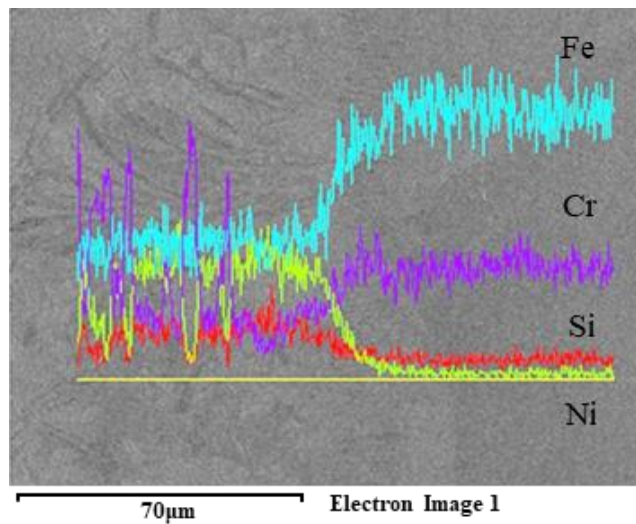
(a)



(b)

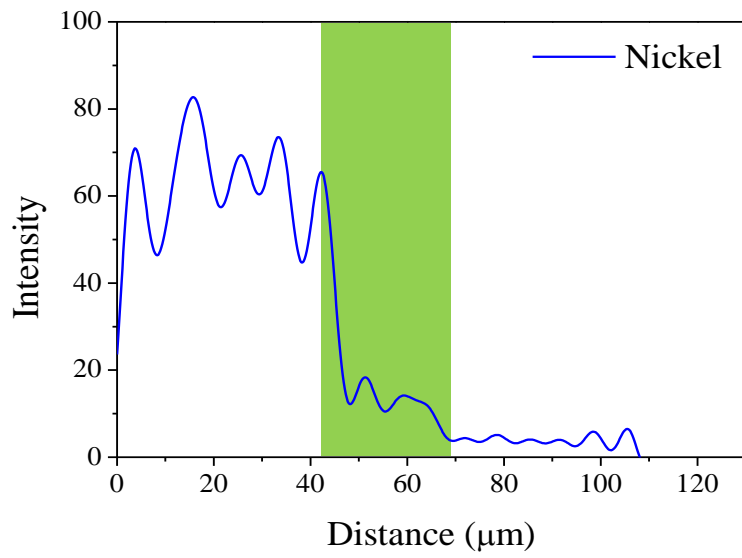


(c)

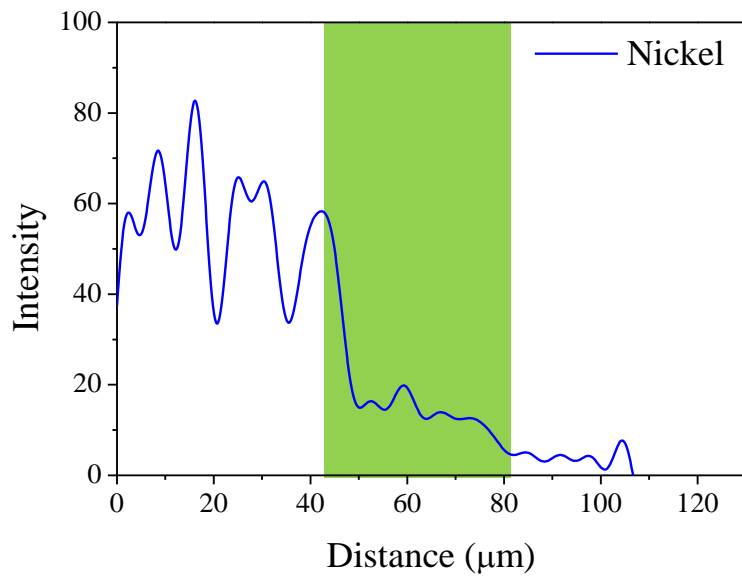


(d)

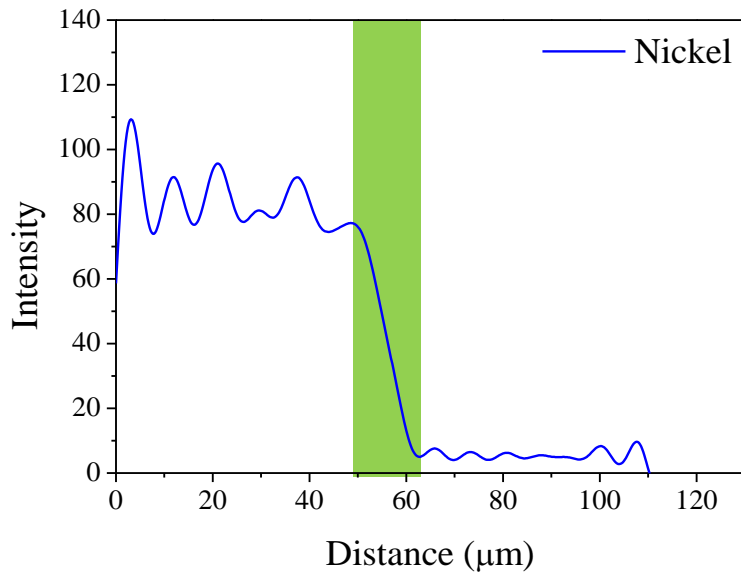
Figure 2. 5 SEM-EDS elemental line scans of Ni, Cr, Si, and Fe across the brazing joint: EA brazing for (a) $t_h = 0$ sec, (b) $t_h = 5$ sec and induction brazing for (c) $t_h = 0$ sec and (d) $t_h = 20$ sec



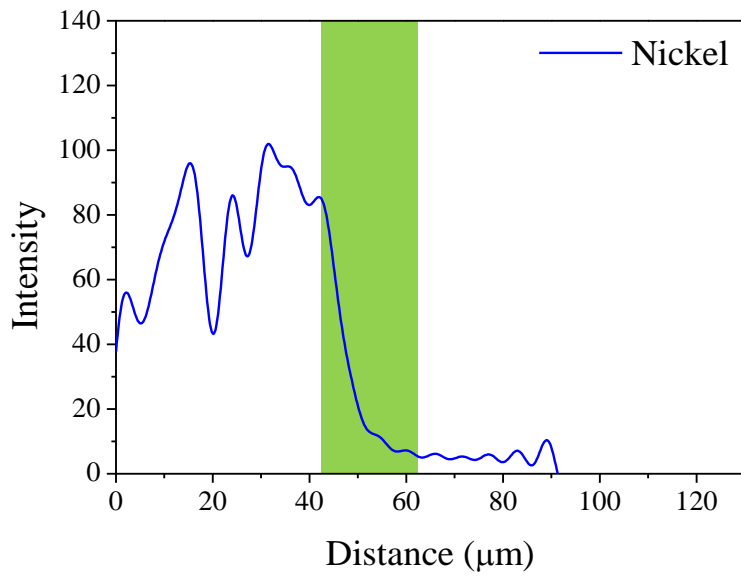
(a)



(b)



(c)



(d)

Figure 2. 6 The Ni distribution: electrically assisted brazing for (a) $t_h = 0$ sec, (b) $t_h = 5$ sec and induction brazing for (c) $t_h = 0$ sec and (d) $t_h = 20$ sec

As expected (Wu et al., 2000; Yu et al., 2014), measurements of the thickness of the diffusion zone show that the thickness increased as the holding time t_h increased (Table 2.3). However, a comparison of the results for electrically assisted brazing and induction brazing shows that the thickness of the diffusion zone can vary significantly depending on the heat source. The diffusion zones of electrically assisted brazing joints appear to be much thicker than those of induction brazing joints. Even the diffusion zone for electrically assisted brazing with $t_h = 0$ sec is approximately 50% thicker than that for induction brazing with $t_h = 20$ sec. The significantly thicker diffusion zones of electrically assisted brazing joints suggest that the athermal effect of the electric current (Conrad, 2000a; Kim et al., 2014a) occurred during electrically assisted brazing in addition to resistance heating. The result of induction brazing was not much different from that of furnace brazing with similar experimental parameters.

For induction brazing, the thickness of diffusion zone, X_D , in Table 2.3 can be simply related to the diffusivity and the diffusion time as (Atabaki et al., 2013)

$$X_D \propto \sqrt{Dt_D} \quad (1)$$

where D and t_D are the diffusivity of Ni to the ferritic stainless steel and the diffusion time, respectively. In the present study, the diffusion time is defined as the period in which the joint temperature is above the liquidus (1000°C) of the filler metal, as listed in Table 2.3. The thickness of the diffusion zone can be plotted as a function of the square root of diffusion time, $\sqrt{t_D}$, as shown in Figure 2.7. As listed in Table 2.3, the figure shows that resistance heating using an electric current result in a significant offset in the thickness of the diffusion zone. Note that the slope of the linear least square fit (LSF) for the results of induction brazing can be easily correlated with diffusivity during induction brazing. However, one may not simply correlate the slope of the LSF from the electrically assisted brazing results with the diffusivity during electrically assisted brazing, since each result for the electrically assisted brazing has

both a different diffusion time and a different history of electric current density. In general, the enhanced diffusion by electric current corresponds well with the enhanced diffusion of Zn/Cu couples by electric current (Li et al., 2008). However, it may be too early to explain the effect of electric current on diffusion by using the theory of electron migration, since a few recent studies reported experimental results that cannot be simply explained by the theory of electron migration (Atabaki et al., 2013; Kim et al., 2014a; Kim et al., 2014c). Even though various hypotheses are being actively investigated (Molotskii and Fleurov, 1995; Park et al., 2017; Kim et al., 2017b), the exact mechanism related with the athermal effect of electric current, has not been identified yet.

Fracture during tensile lap-shear tests occurred in the interlayer along the interface between the diffusion zone and the interlayer for all electrically assisted and induction brazing joints (Figure 2.8). For both electrically assisted and induction brazing, the shear strength increased with increasing holding time t_h (or the brazing time t_D), as shown in Figure 2.9. A comparison of the shear strength of the joints shows that electrically assisted brazing induced a higher fracture strength than induction brazing even with a shorter holding time or brazing time. For example, electrically assisted brazing with $t_h = 0$ sec (or $t_D = 2$ sec) induced an average fracture strength of 184 MPa, which is higher than the result of the induction brazing with $t_h = 10$ sec (or $t_D = 18.5$ sec) and comparable to the result of induction brazing with $t_h = 20$ sec (or $t_D = 28.3$ sec), as indicated in Figure 2.9. The higher fracture strength obtained by electrically assisted brazing stainless steel in electrically assisted brazing, since the strength of the brazing joint is affected by the diffusion of main alloying elements in the filler metal to the base metal (Atabaki et al., 2013; Khorram and Ghoreishi, 2015).

Type	Electrically assisted brazing for holding time (sec)			Induction brazing for holding time (sec)			
	$t_h = 0$ (or $t_D = 2$)	$t_h = 5$ (or $t_D = 6.6$)	$t_h = 10$ (or $t_D = 11.7$)	$t_h = 0$ (or $t_D = 9$)	$t_h = 10$ (or $t_D = 18.5$)	$t_h = 20$ (or $t_D = 28.3$)	
Thickness of Ni gradient (μm)	Top 01	29.5	40.1	45.6	15.7	16.8	19.5
	Top 02	24.6	39.4	43.5	11.5	17.4	17.3
	Bottom 01	32.6	37.4	40.3	12.6	18.5	22.1
	Bottom 02	30.1	37.1	38.2	14.2	14.5	20.7
	Average	29.2	38.5	41.9	13.5	16.8	19.9

Table 2. 3 The thickness of diffusion zone in brazing experiment with various brazing conditions

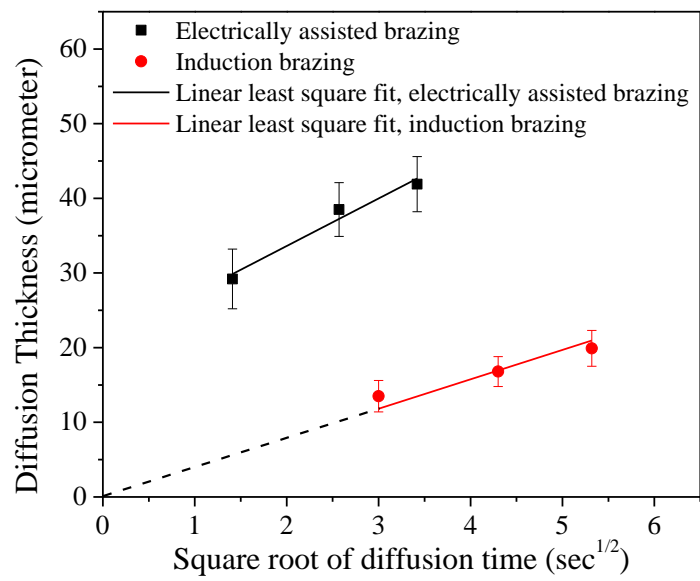


Figure 2. 7 The diffusion thickness as a function of the square root of diffusion time

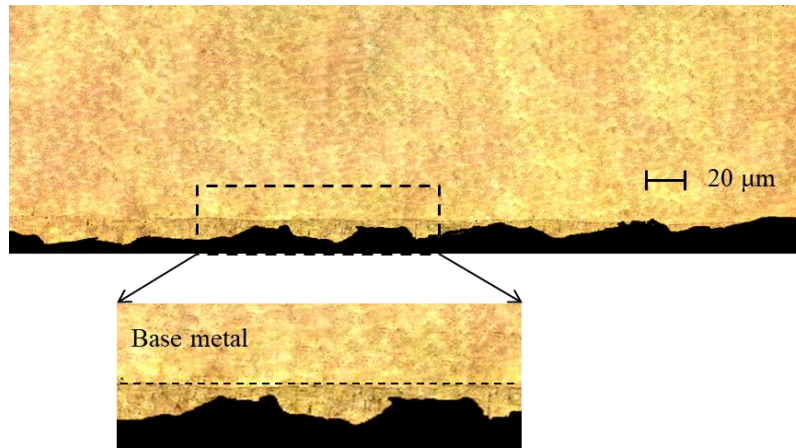


Figure 2. 8 Cross-sectional image of brazing joints after shear test for electrically assisted brazing specimen for $t_h = 5$ sec

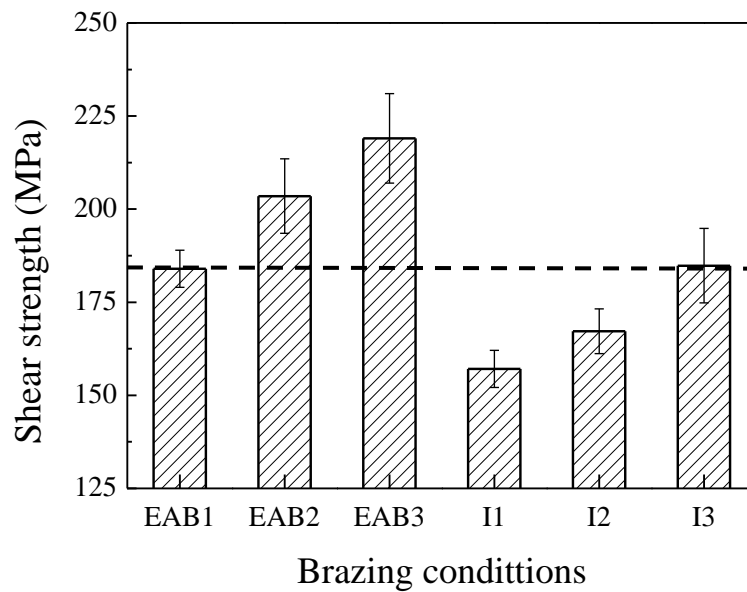


Figure 2. 9 Comparison of shear strength: electrically assisted brazing for $t_h = 0$ sec (EAB1), $t_h = 5$ sec (EAB2), and $t_h = 10$ sec (EAB3) and induction brazing for holding time of $t_h = 0$ sec (I1), $t_h = 10$ sec (I2) and $t_h = 20$ sec (I3)

2.4 CONCLUSION

In the present study, the effectiveness of electrically assisted brazing was compared with that of conventional induction brazing by joining ferritic stainless steel sheets with a Ni-based filler metal. As shown in the microstructural analysis results, the electric current during electrically assisted brazing significantly enhanced the diffusion between the filler metal and the ferritic stainless steel sheets in comparison with induction brazing. The enhanced diffusion during electrically assisted brazing strongly supports the athermal effect of electric current, which is closely related to the theory of electroplasticity. Also, the results of mechanical tests showed that electrically assisted brazing provided a joint strength comparable to the strength of the induction brazing joint with a significantly shorter processing time. Therefore, the electrically assisted brazing provides the technical advantage that the process time can be significantly reduced without sacrificing the joint strength (or a higher joint strength with a similar process time) in comparison with induction brazing. Also, due to the significantly higher heating rate, the energy loss to the environment during heating is likely to be less in electrically assisted brazing than in induction brazing. These superior properties of electrically assisted brazing over induction brazing could make electrically assisted brazing a strong candidate to replace conventional induction brazing.

References

- Atabaki, M.M., Wati, J.N., Idris, J., 2013. Transient Liquid Phase Diffusion Brazing of Stainless Steel 304. *Welding Journal*, 57–63.
- Baranov, S.A., Staschenko, V.I., Sukhov, A.V., Troitskiy, O.A., Tyapkin, A.V., 2011. Electroplastic metal cutting. *Russian Electrical Engineering* 82, 477–479.
- Conrad, H., 2000. Electroplasticity in metals and ceramics. *Materials Science and Engineering: A* 287, 276–287.
- Davies, J., Simpson, P., 1979. *Induction heating handbook*. McGraw-Hill.
- Khorram, A., Ghoreishi, M., 2015. Comparative study on laser brazing and furnace brazing of Inconel 718 alloys with silver based filler metal. *Optics & Laser Technology* 68, 165–174.
- Kim, K.-H., Bang, Han-Sur, Ro, C.-S., Bang, Hee-Seon, 2017a. Influence of preheating source on mechanical properties and welding residual stress characteristics in ultra thin ferritic stainless steel hybrid friction stir welded joints. *International Journal of Precision Engineering and Manufacturing-Green Technology* 4, 393–400.
- Kim, M.-J., Lee, K., Oh, K.H., Choi, I.-S., Yu, H.-H., Hong, S.-T., Han, H.N., 2014a. Electric current-induced annealing during uniaxial tension of aluminum alloy. *Scripta Materialia* 75, 58–61.
- Kim, M.-J., Lee, M.-G., Hariharan, K., Hong, S.-T., Choi, I.-S., Kim, D., Oh, K.H., Han, H.N., 2017b. Electric current-assisted deformation behavior of Al-Mg-Si alloy under uniaxial tension. *International Journal of Plasticity* 94, 148–170.
- Kim, M.-S., Vinh, N.T., Yu, H.-H., Hong, S.-T., Lee, H.-W., Kim, M.-J., Han, H.N., Roth, J.T., 2014b. Effect of electric current density on the mechanical property of advanced high strength steels under quasi-static tensile loads. *International Journal of Precision Engineering and Manufacturing* 15, 1207–1213

- Kim, W., Yeom, K.-H., Thien, N.T., Hong, S.-T., Min, B.-K., Ik Oh, S., Kim, M.-J., Han, H.N., Lee, H.-W., 2014c. Electrically assisted blanking using the electroplasticity of ultra-high strength metal alloys. *CIRP Annals* 63, 273–276.
- Li, Y., Yang, Y., Feng, X., 2008. Influence of Electric Current on Kirkendall Diffusion of Zn/Cu Couples. *Journal of Materials Science & Technology* 24, 410-414.
- Lugscheider, E., 1983. High Temperature Brazing of Stainless Steel with Nickel-Base Filler Metals BNi-2, BNi-5 and BNi-7. *Welding Journal* 62, 160–164.
- Mohandas, T., Madhusudhan Reddy, G., Naveed, M., 1999. A comparative evaluation of gas tungsten and shielded metal arc welds of a “ferritic” stainless steel. *Journal of Materials Processing Technology* 94, 133–140.
- Molotskii, M., Fleurov, V.V., 1995. Magnetic effects in electroplasticity of metals. *Phys. Rev., B Condens. Matter* 52, 15829–15834.
- Ng, M.-K., Li, L., Fan, Z., Gao, R.X., Smith, E.F., Ehmman, K.F., Cao, J., 2015. Joining sheet metals by electrically-assisted roll bonding. *CIRP Annals* 64, 273–276.
- Nguyen-Tran, H.-D., Oh, H.-S., Hong, S.-T., Han, H.N., Cao, J., Ahn, S.-H., Chun, D.-M., 2015. A review of electrically-assisted manufacturing. *International Journal of Precision Engineering and Manufacturing-Green Technology* 2, 365–376.
- Oh, H.-S., Cho, H.-R., Park, H., Hong, S.-T., Chun, D.-M., 2016. Study of electrically-assisted indentation for surface texturing. *International Journal of Precision Engineering and Manufacturing-Green Technology* 3, 161–165.
- Ou, C.L., Liaw, D.W., Du, Y.C., Shiue, R.K., 2006. Brazing of 422 stainless steel using the AWS classification BNi-2 Braze alloy. *Journal of Materials Science* 41, 6353–6361.
- Park, J.-W., Jeong, H.-J., Jin, S.-W., Kim, M.-J., Lee, K., Kim, J.J., Hong, S.-T., Han, H.N., 2017. Effect of electric current on recrystallization kinetics in interstitial free steel and AZ31 magnesium alloy. *Materials Characterization* 133, 70–76.

- Shiue, R.K., Wu, S.K., Hung, C.M., 2002. Infrared repair brazing of 403 stainless steel with a nickel-based braze alloy. *Metallurgical and Materials Transactions A* 33, 1765–1773.
- Taban, E., Deleu, E., Dhooge, A., Kaluc, E., 2009. Laser welding of modified 12% Cr stainless steel: Strength, fatigue, toughness, microstructure and corrosion properties. *Materials & Design* 30, 1193–1200.
- Thien, N.T., Hong, S.-T., Kim, M.-J., Han, H.N., Yang, D.-H., Lee, H.-W., Lee, K., 2016a. Electrically assisted bake hardening of complex phase ultra-high strength steels. *International Journal of Precision Engineering and Manufacturing* 17, 225–231.
- Thien, N.T., Jeong, Y.-H., Hong, S.-T., Kim, M.-J., Han, H.N., Lee, M.-G., 2016b. Electrically assisted tensile behavior of complex phase ultra-high strength steel. *International Journal of Precision Engineering and Manufacturing-Green Technology* 3, 325–333.
- Wu, X., Chandel, R.S., Pheow, S.H., Li, H., 2000. Brazing of Inconel X-750 to stainless steel 304 using induction process. *Materials Science and Engineering: A* 288, 84–90.
- Xu, Z., Peng, L., Lai, X., 2014. Electrically assisted solid-state pressure welding process of SS 316 sheet metals. *Journal of Materials Processing Technology* 214, 2212–2219.
- Yang, R.-T., Chen, Z.-W., 2013. A study on fiber laser lap welding of thin stainless steel. *International Journal of Precision Engineering and Manufacturing* 14, 207–214.
- Yu, C.-C., Su, P.-C., Bai, S.J., Chuang, T.-H., 2014. Nickel-tin solid-liquid inter-diffusion bonding. *International Journal of Precision Engineering and Manufacturing* 15, 143–147.

CHAPTER III

FEASIBILITY OF A TWO-STAGE FORMING PROCESS OF 316L AUSTENITIC STAINLESS STEELS WITH RAPID ELECTRICALLY ASSISTED ANNEALING

ABSTRACT

The post-annealing mechanical behavior of 316L austenitic stainless steel (SUS316L) after electrically assisted (EA) annealing with a single pulse of electric current is experimentally investigated to evaluate the feasibility of a two-stage forming process of the selected SUS316L with rapid EA annealing. A tensile specimen is deformed to a specific prestrain and then annealed by applying a single pulse of electric current with a short duration less than 1 sec. Finally, the specimen is reloaded until fracture. The stress-strain curve during reloading shows that the flow stress of the SUS316L significantly decreases, which indicates the occurrence of EA annealing. The electric current also increases the maximum achievable elongation of the SUS316L during reloading. The stress-strain curve during reloading and the microstructural observation suggest that the effects of EA annealing on the post-annealing mechanical behavior and microstructure strongly depend on both the applied electric current density (electric current per unit cross-sectional area) and the given prestrain. The results of the present study suggest that the EA annealing technique could be effectively used to improve the formability of SUS316L when manufacturing complex parts.

Keywords: electrically assisted annealing; electric current; prestrain; stainless steels

3.1 INTRODUCTION

Formability is an important issue for all metallic materials in forming processes, even for austenitic stainless steels (ASSs). ASSs are known to have good formability, excellent corrosion resistance, and good weldability (Acar and Fitzpatrick, 2017; Andrade et al., 2004; Peterson et al., 1997). However, in some industrial applications, the good formability of ASSs may still not be satisfactory (Anderson et al., 2013; Thanakijkasem et al., 2014). For example, in deep drawing of consumer electric components using ASSs, the forming process is frequently composed of two (or multiple) forming stages with heat treatment between the forming stages, due to the formability of the ASSs.

Furnace annealing between forming stages is a commercially well-established heat treatment process to control the formability of an ASS in a two- or multiple-stage forming process. A deformed part is heat-treated in a certain temperature range (800-1100°C) for a specified duration (usually from 30 to 45 min) (Anderson et al., 2013; Thanakijkasem et al., 2014) before the next forming stage. While furnace annealing can effectively restore the formability of the product by annihilating strain hardening from the previous forming stage, furnace annealing frequently becomes quite time-consuming and expensive. Thus, a cost-effective and preferably rapid alternative technique to control the formability of ASS is still desired.

Electrically assisted manufacturing (EAM) is a promising metal forming technique, in which the mechanical property of a metal is controlled by simply applying electricity to the metal during deformation (referred to as electroplasticity) (Okazaki et al., 1978; Conrad, 2000a). In the investigation of the effect of electric current on the mechanical behavior of metal alloys, several researchers repeatedly applied electric current with a short duration (pulsed electric current) to a metal during deformation. Roth et al. (2008) applied a pulsed electric current to aluminum 5754 alloy during tension to achieve maximum elongation close to 400%

of the gage length. Salandro et al. (2010) applied a pulsed electric current to aluminum 5052 and 5083 alloys during tension. According to Salandro et al. (2010), the effectiveness of the electric current on the tensile behavior of selected aluminum alloys depends on both the alloy and the heat treatment. Kim et al. (2014a) and Roh et al. (2014) reported that the formability of aluminum alloys during tension with a pulsed electric current is increased due to electric current induced (or electrically assisted: EA) annealing. It has also been reported that the microstructure of metals can be significantly affected by electric current. Conrad et al. (2000) reported that the plasticity and phase transformation of various metals and ceramics were affected by an electric current. Xu et al. (1988) reported that recrystallization and grain growth of cold rolled α -Ti were accelerated by an electric current. More recently, Park et al. (2017) reported that the annealing temperature and time for recrystallization of interstitial free (IF) steel and AZ31 magnesium alloy were significantly reduced by electropulsing treatment (EPT) compared to conventional heat treatment with a furnace. It is important to note, however, that for specific metal alloys and experimental conditions, applying an electric current during deformation may induce adverse effects on the formability (Magargee et al., 2013; Jeong et al., 2018). Magargee et al. (2013) observed that the formability of commercially pure titanium was not significantly changed when an electric current was applied during tensile deformation, even though the flow stress substantially decreased. Jeong et al. (2018) studied the effect of electric current on the tensile behavior of transformation induced plasticity (TRIP)-aided steel and reported that the elongation of TRIP-aided steel significantly decreased by applying a pulsed electric current during tensile deformation. They suggested that the effect of electric current on the mechanical behavior can be strongly affected by designing the pulsing pattern of the electric current in accordance with the material's characteristic.

While applying a pulsed electric current to a metal alloy during deformation generally enhances the formability of the metal alloy, it may not be practical to design a commercial

metal forming process with a pulsed electric current. The cycle time of the process may be significantly increased and/or the structure of forming machines may become quite complex. Several recent studies on EAM or electroplasticity have reported that the mechanical properties of a metal can be altered by applying a single pulse of electric current of short duration. Kim et al. (2014b) reported that the springback in U-bending of advanced high strength steel sheets can be reduced or even eliminated by applying a single pulse of electric current prior to removal of the forming load. Thien et al. (2016) applied a single pulse of electric current to a complex phase ultra-high strength steel at a specific prestrain and reported that the flow stress significantly decreased and the formability increased during reloading. These previous studies suggest that electrically assisted two- (or multiple-) stage metal forming processes for certain metal alloys may be effectively designed with a single pulse of electric current.

However, studies on the mechanical behavior of metal alloys (including ASSs) under a single pulse of electric current between plastic deformations are still quite limited. In the present study, the effect of a single pulse of electric current on the mechanical behavior and microstructure of a commercially available 316L austenite stainless steel (SUS316L) is reported. Specifically, the goal of the present study is to evaluate the feasibility of a two-stage forming process of the selected SUS316L with rapid EA annealing.

3.2 EXPERIMENTAL SET-UP

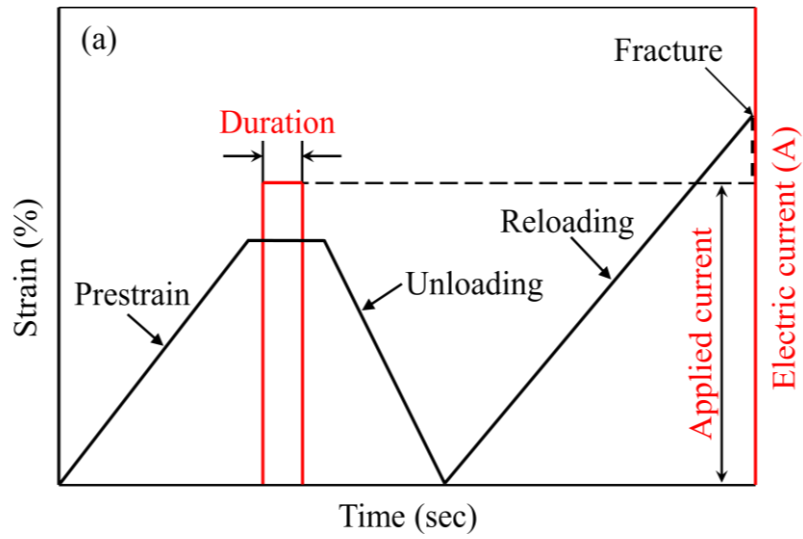
Commercially available 1 mm thick grade SUS316L sheets (Fe-17.06Cr-9.81Ni-1.17Mn-1.97Mo-0.59Si-0.028C in wt.%) were used for the experiment. Typical tensile specimens according to ASTM-E08 with a gage width of 12.5 mm and a gage length of 50 mm were fabricated by laser cutting along the rolling direction of the sheet.

In the present study, electrically assisted (EA) two-stage forming of the selected SUS316L was simply implemented by quasi-static tensile tests with a single pulse of electric current, as schematically described in Figure 3.1. The quasi-static tensile test was conducted using a universal testing machine. The baseline tensile test was first conducted by simply deforming a specimen by tension until fracture. For the quasi-static tensile test with EA annealing, a specimen was first deformed to a specified prestrain by uniaxial tension with a constant displacement rate of 2.5 mm/min. A single pulse of electric current with a short duration was then applied to the prestrained specimen to induce EA annealing, according to the electric current parameters. Next, the specimen was cooled to room temperature in air and unloaded. Finally, the specimen was reloaded until fracture by uniaxial tension with a constant displacement rate of 2.5 mm/min.

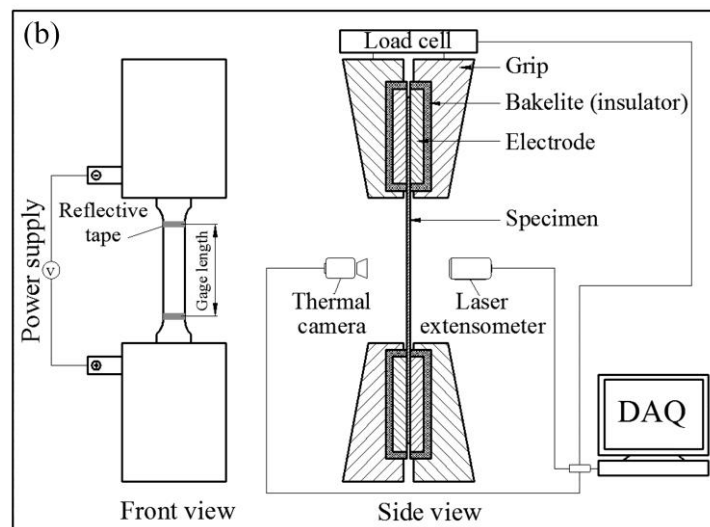
For EA annealing, the electric current was generated by a programmable Vadal SP-1000U power supply (Hyosung, South Korea). By inserting a set of bakelite insulators between the specimen and grips, the tensile test machine was insulated from the electric current (Figure 3.1(b)). The force history during the experiment was measured as a function of time by a load cell using a PC-based data acquisition system (Figure 3.1(b)). The displacement history was also measured using a laser extensometer (LX500, MTS, Eden Prairie, MN, USA) by attaching retro-reflective tape to the specimen. Finally, an infrared thermal imaging camera (T621, FLIR, Taby, Sweden) was employed to monitor the temperature change of the specimen throughout the experiment. It should be noted that one side of the specimen was sprayed with black thermal

paint to stabilize the emissivity and thus improve the accuracy of the temperature measurement.

The emissivity was calibrated by a k-type thermocouple through separate calibration tests.



(a)



(b)

Figure 3. 1 Schematics of (a) electrically assisted (EA) annealing with a single pulse of electric current and (b) the experimental set-up

For the parameter study, two different prestrain levels (20 and 60%) were combined with three different true electric current densities (95, 100, and 105 A/mm²) and a constant electric current duration of 0.75 sec. It should also be noted that the selected prestrains in the present study correspond to 20% and 60% of uniform elongation from the baseline tensile test (without prestrain and electric current), respectively, as indicated in Figure 3.2. The true electric current density was calculated based on the actual cross-sectional area of the specimen at the given prestrain, as the term “true” indicates. For each parameter set, at least three specimens were tested to verify repeatability of the results.

To analyze the effect of electric current on the microstructure of a prestrained specimen, the EA annealed specimen was removed from the test without reloading to fracture and was prepared for microstructural analysis. The microstructure of the specimen was characterized by an electron probe microanalyzer (EPMA, JXA-8530F, JEOL Ltd., Tokyo, Japan) and a field emission gun scanning electron microscope (FE-SEM, SU70, Hitachi, Tokyo, Japan) equipped with an electron backscatter diffraction system (EBSD, EDAX/TSL, Hikari, Hayward, CA, USA). To evaluate the change of dislocation density by EA annealing, the full width at half maximum (FWHM) of the diffraction peak was measured with an X-ray diffractometer (D8-Advanced, BRUKER MILLER Co., Massachusetts, USA) using a Cu radiation source operating at 50 kV at room temperature. Diffraction patterns were recorded in the scan range of 40–85° with a scan speed of 1°/min. Specimens for microstructural observation were prepared by mechanical grinding followed by electropolishing with an 80 mL perchloric acid, 90 mL distilled water, 100 mL butanol, and 730 mL ethanol solution at 20 V. For EBSD analysis, the accelerating voltage and scan step size were 15 kV and 0.5 μm, respectively. The critical misorientation angle was set to 15° for grain identification.

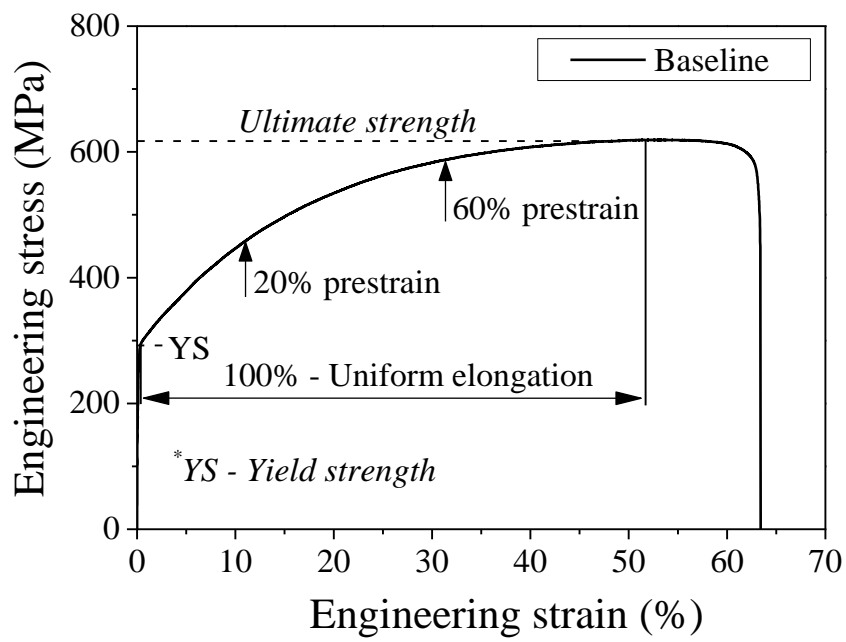
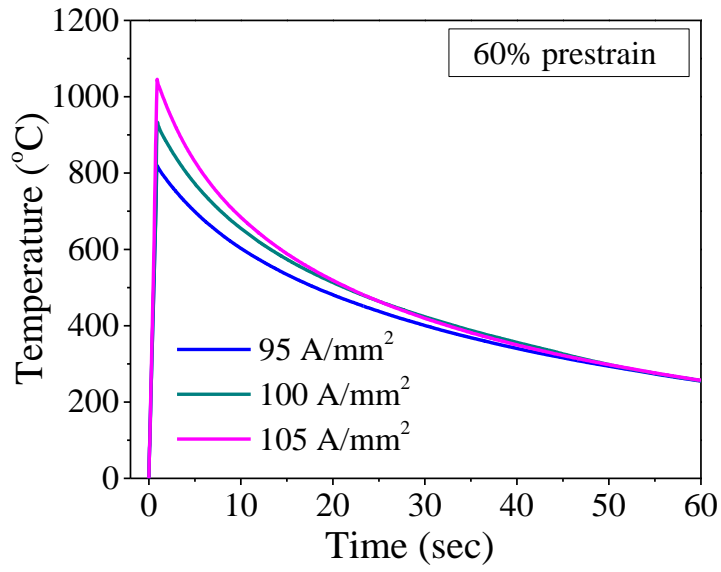


Figure 3. 2 A stress–strain curve of a baseline specimen

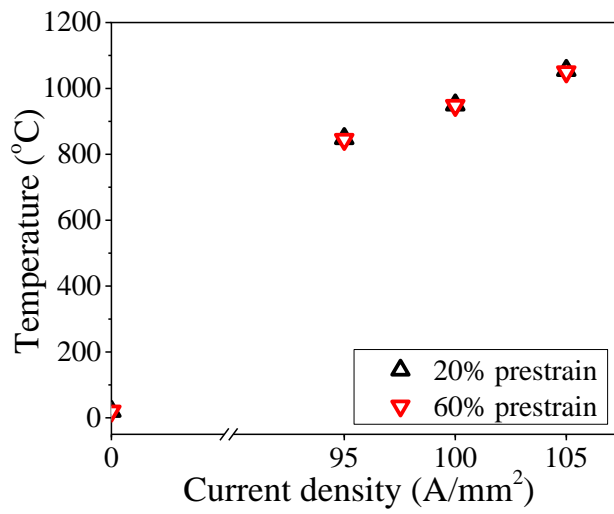
3.3 RESULTS AND DISCUSSION

During EA annealing, the temperature of the specimen rapidly reached the maximum temperature using resistance heating followed by cooling, as representative temperature histories of the 60% prestrained specimens shown in Figure 3.3(a). It should be noted that the temperature was measured at the center of the specimen, which gave the highest temperature from application of the electric current. Naturally, the peak temperature increased as the current density was increased as shown in Figure 3.3(b). Additionally, there was no significant effect of two different prestrains on the peak temperature.

From the load-displacement history during reloading, engineering stress-strain curves during reloading were constructed based on the gage length and cross-sectional area at each prestrain, as shown in Figure 3.4. As expected, the yield strengths during reloading (the post-annealing yield strengths) generally showed higher values than the baseline yield strength without prestrain due to strain hardening for both prestrains. For the same reason, the elongations at fracture during reloading (the post-annealing elongation) for both prestrains generally showed lower values than the baseline elongation at fracture without prestrain. As the current density was increased, the engineering stress-strain curves during reloading clearly showed that the flow stress of the SUS316L gradually decreased, which indicates the occurrence of EA annealing (Kim et al., 2014a). The post-annealing elongation also clearly increased with increasing current density.

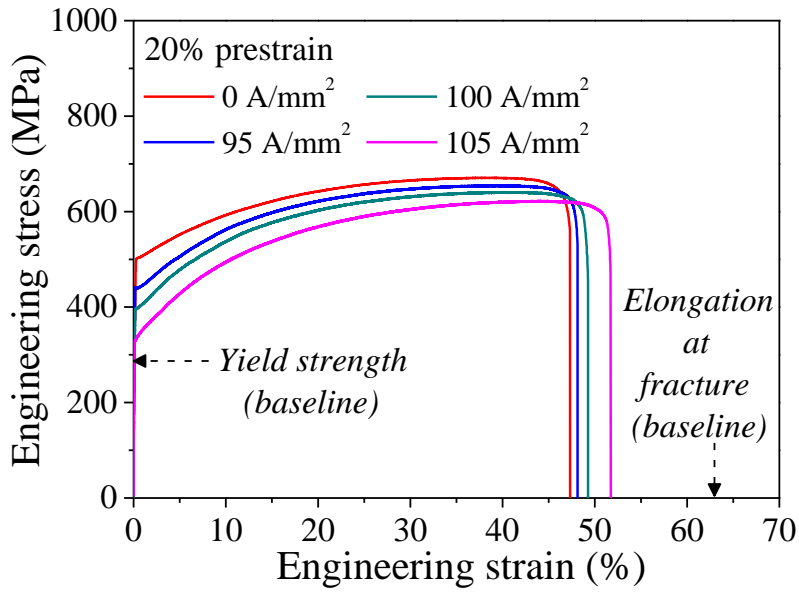


(a)

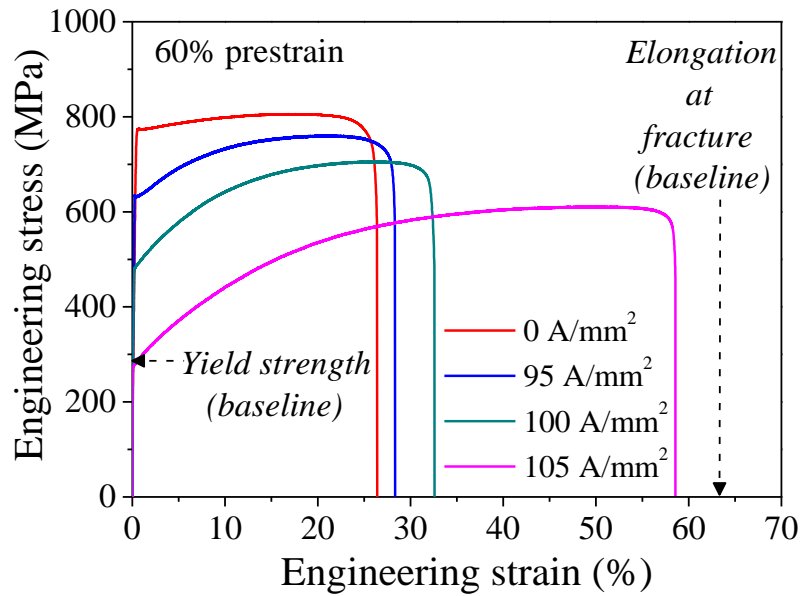


(b)

Figure 3. 3 (a) Temperature histories of 60% prestrained specimens and (b) the peak temperatures as functions of current density during EA annealing for different prestrains



(a)



(b)

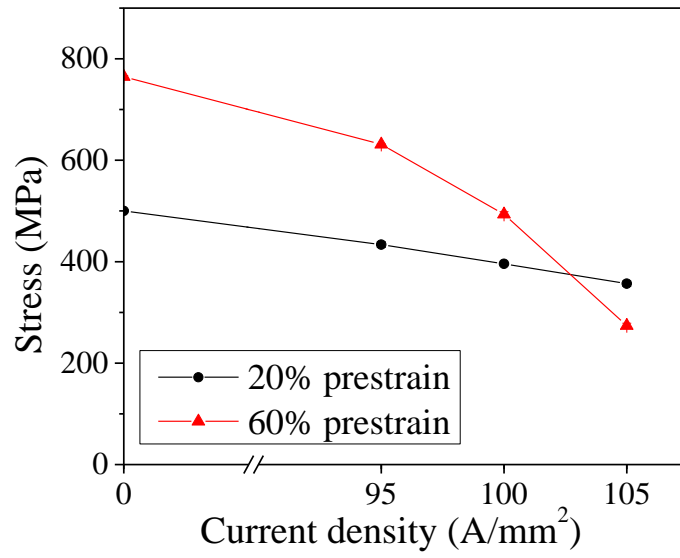
Figure 3. 4 Engineering stress-strain curves after EA annealing with (a) 20% prestrain and (b) 60% prestrain; the engineering stress-strain curves during reloading was constructed based on the gage length and the cross-sectional area at each prestrain

The post-annealing yield strength and post-annealing elongation can be plotted as functions of current density (Figures 3.5(a) and (b), respectively). The results in Figures 3.5(a) and (b) suggest that the effect of EA annealing on the mechanical behavior during reloading is significantly different depending on the magnitude of the prestrain, even with the same true current density and nearly identical peak temperatures. As shown in Figures 3.5(a) and (b), with the higher prestrain, the effect of EA annealing becomes more pronounced, i.e., the post-annealing yield strength and post-annealing elongation change more rapidly with the higher prestrain, as the current density increases with the constant duration of electric current. The effectiveness of EA annealing on the formability of the SUS316L can be further evaluated by comparing the total achievable displacement or total achievable elongation based on the original gage length of the baseline specimen. The total achievable displacement and total achievable elongation can be simply calculated as:

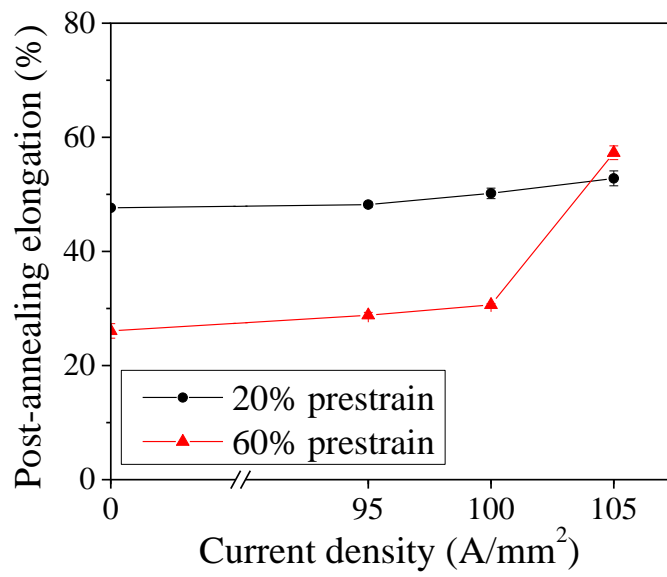
Total achievable displacement = displacement by prestrain + displacement during reloading

Total achievable elongation = total achievable displacement/the gage length of the baseline specimen

The total achievable elongation as a function of current density, clearly seen in Figures 3.6(a) and (b) confirms that EA annealing at the higher prestrain is beneficial to improve formability of the given metal alloy. Especially at the highest current density of 105 A/mm², the total achievable elongation with the 60% prestrain was approximately 1.5 times higher than that with the 20% prestrain (Figures 3.6(a) and (b)). It is to be noted that the total achievable elongation with the 20% prestrain and current density of 95 A/mm² still surpassed that of the baseline tensile test.

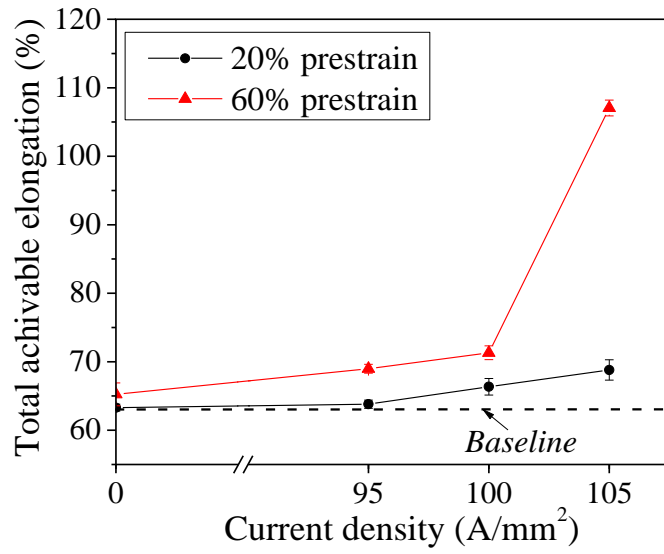


(a)

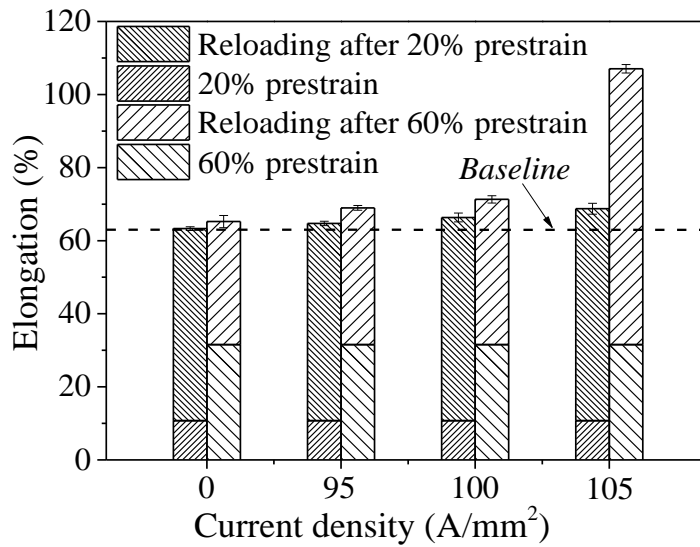


(b)

Figure 3. 5 (a) Post-annealing yield strength and (b) post-annealing elongation of prestrained specimens after EA annealing



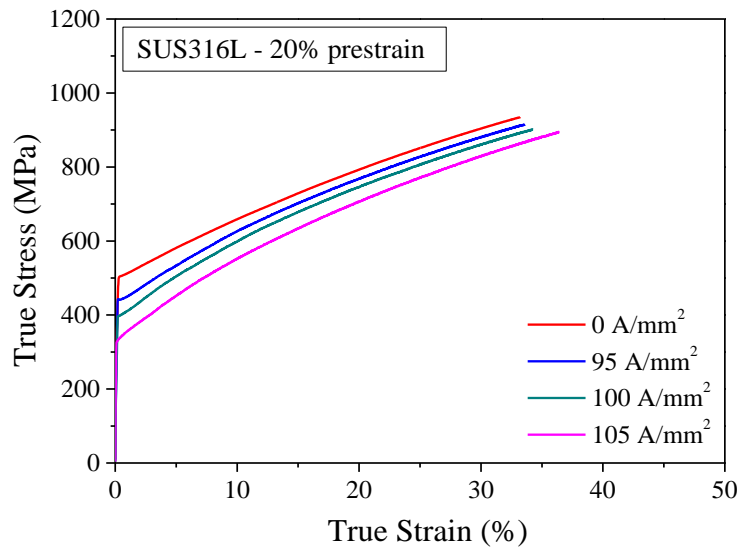
(a)



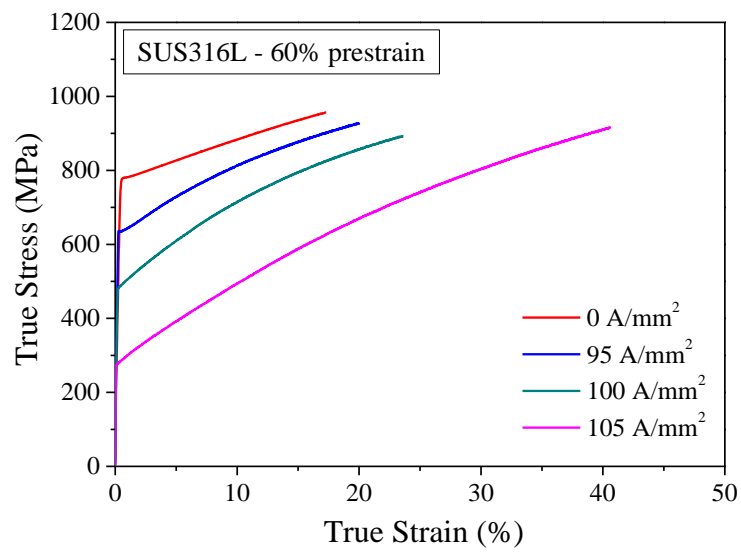
(b)

Figure 3. 6 (a) Total achievable elongation as a function of current density and (b) the effect of prestrain and the current density on the total achievable elongation; the total achievable elongation was calculated based on the original gage length of the baseline specimen

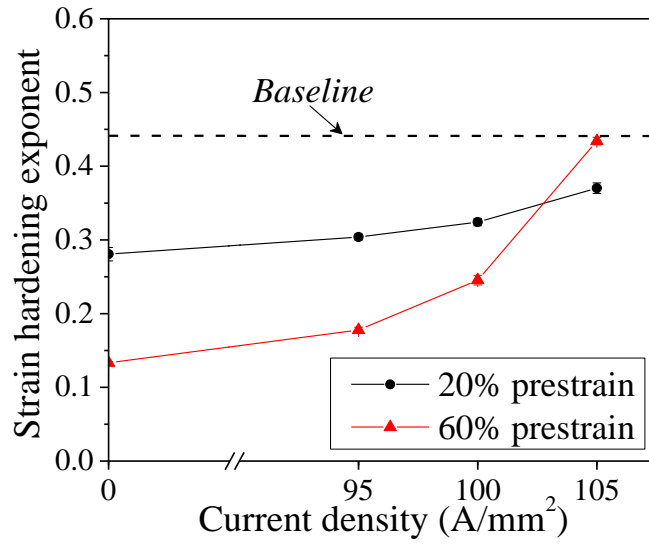
For evaluation of the effect of EA annealing on hardening behavior during reloading, the engineering stress-strain curves in Figure 3.4 were converted to true stress-strain curves up to the engineering strain of uniform elongation, as shown in Figures 3.7(a) and (b). As expected, strain hardening parameters with the higher prestrain showed lower values in comparison to those with the lower prestrain. However, the strain hardening exponent (Figure 3.7(c)) and strength coefficient (Figure 3.7(d)) as functions of current density showed that with the higher prestrain, both strain hardening parameters increased more rapidly as the current density was increased. At the current density of 105 A/mm^2 , the strain hardening parameters during reloading with the 60% prestrain became nearly identical to those of the baseline curve without prestrain. This finding suggests that the strain hardening by the given prestrain was completely annihilated by the electric current with a duration of 0.75 sec, which confirms the benefit of EA annealing as a rapid annealing process for cost-effective two-stage forming. However, it should be noted that with the 20% prestrain, the strain hardening parameters during reloading were not close to those of the baseline curve without prestrain, even at the current density of 105 A/mm^2 , which was the highest current density selected in the present study. Therefore, in the design of two-stage forming with EA annealing, the amount of deformation in the first forming stage needs to be carefully decided to optimize the effect of EA annealing in the process.



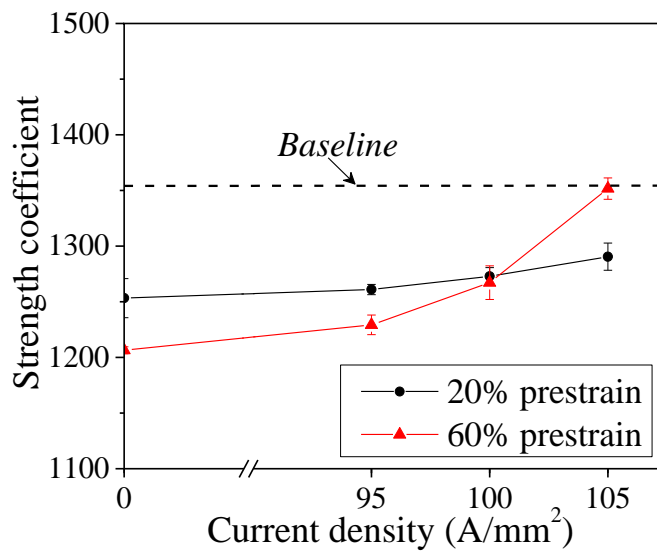
(a)



(b)



(c)



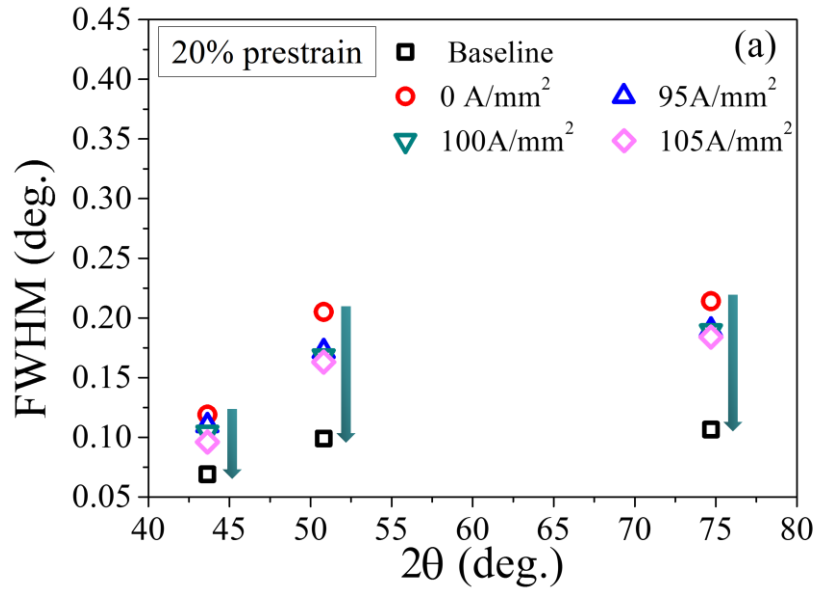
(d)

Figure 3. 7 True stress-strain curves after EA annealing with (a) 20% prestrain and (b) 60% prestrain; (c) strain hardening exponent and (d) strength coefficient of prestrained specimens after EA annealing

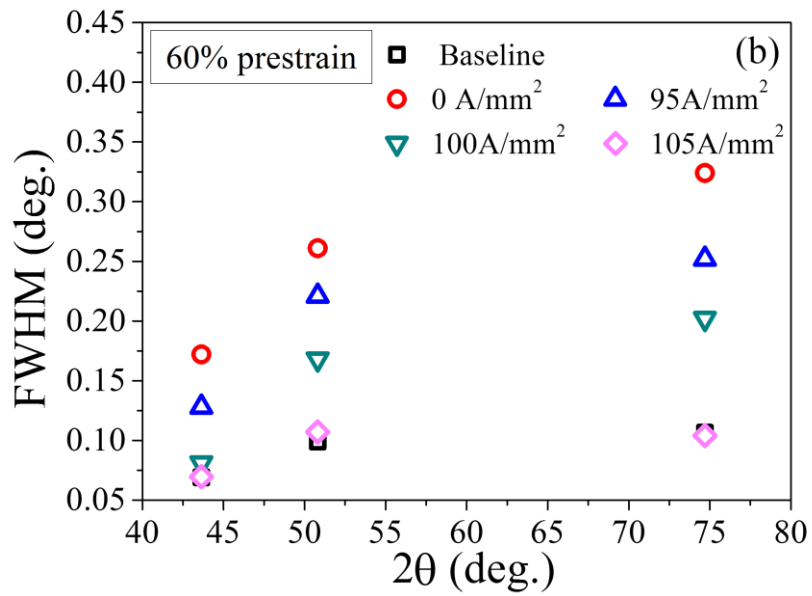
As presented above, the mechanical behavior of the SUS316L during reloading after a short duration of electric current strongly suggests the occurrence of EA annealing. To confirm this occurrence of EA annealing, FWHM analysis of the diffraction peak profile can be effectively used (Hong et al., 2015; Kim et al., 2017). For crystalline materials, the diffraction peak profile is typically broadened when the crystal lattice is distorted by lattice defects, especially by dislocations (Williamson and Hall, 1953; Ungár and Borbély, 1996). As shown in Figures 3.8(a) and (b), the FWHM values decreased with increasing current density for both prestrains selected in the present study. The results in Figures 8(a) and (b) clearly confirm the reduction of dislocation density (annihilation of dislocations) in the prestrained specimen by the applied electric current, which is EA annealing. It should be noted that for the 60% prestrain, the FWHM values show that the specimen was fully annealed to the baseline status without prestrain when the electric current density of 105 A/mm^2 was applied. Therefore, it is speculated that recrystallization occurred under this condition. In contrast, for all of the 20% prestrained specimens, full annealing was not achieved, even though the peak temperatures were nearly the same, as shown in Figure 3(b). The results of the FWHM analysis are in good agreement with the observed mechanical behavior during reloading after EA annealing in Figures 3.4–3.6.

Figure 3.9(a) and (b) show the EBSD inverse pole figures (IPF) with respect to the normal direction (ND) and kernel average misorientation (KAM) maps for each specimen. For KAM maps, the higher degree of misorientation is denoted by a brighter color. The color of the KAM maps is proportional to the amount of dislocation or the accumulated strain energy present in the specimen, as indicated in the color scale bar. The KAM maps display effects, which can be interpreted as dislocations. For EA annealing with 105 A/mm^2 , the average grain size of the 60% prestrained specimen was significantly reduced from 17.0 ± 5.9 to $12.1 \pm 4.3 \text{ }\mu\text{m}$. The average KAM value of the 60% prestrained specimen was also significantly reduced

from 1.10 to 0.33 under the condition of 105 A/mm². This result clearly indicates that recrystallization occurred in the 60% prestrained specimen after EA annealing with the current density of 105 A/mm². In addition, the grain orientation spread (GOS) map was used to determine the recrystallization fraction and the recrystallized grain is defined within 2° of GOS, as shown in Figure 3.9 (c). It was observed that the recrystallized area fraction was approximately 99.6 % which confirms the full recrystallization in the 60% prestrained specimen after EA annealing with the current density of 105 A/mm². This result coincides with the FWHM value of the 60% prestrained specimen under the electric current density of 105 A/mm², as shown in Figure 3.8(b). This result can be explained as the dislocation density induced by the 60% prestrain was high enough to provide the driving force for recrystallization (Cho and Yoo, 2001) during EA annealing with 105 A/mm² for the duration of 0.75 sec. This phenomenon might be related to the acceleration of recrystallization kinetics due to the electric current (Park et al., 2017). No significant changes in the grain size were observed for the other combinations of prestrain and electric current density considered in the present study.

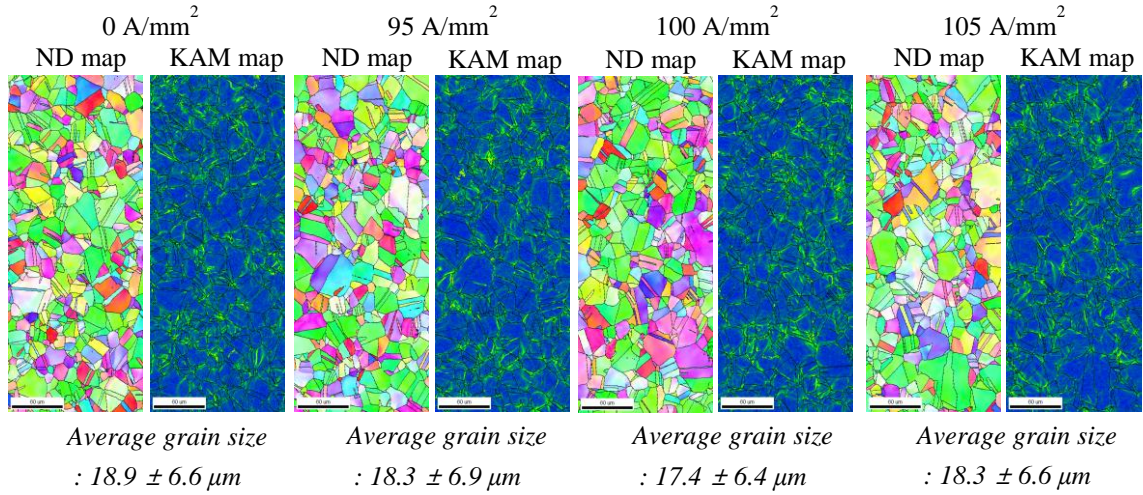
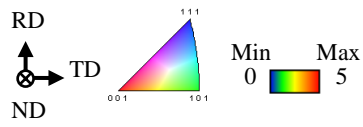


(a)

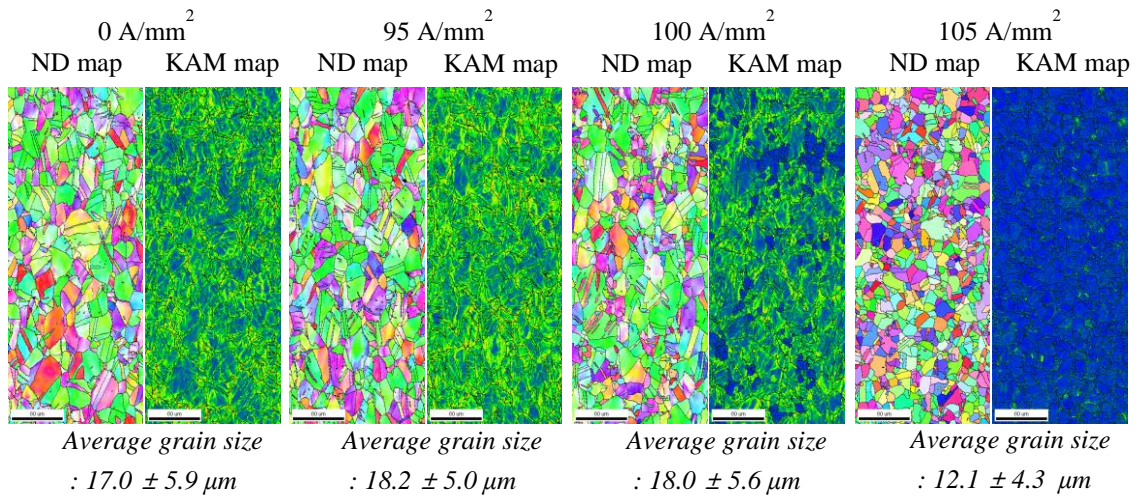


(b)

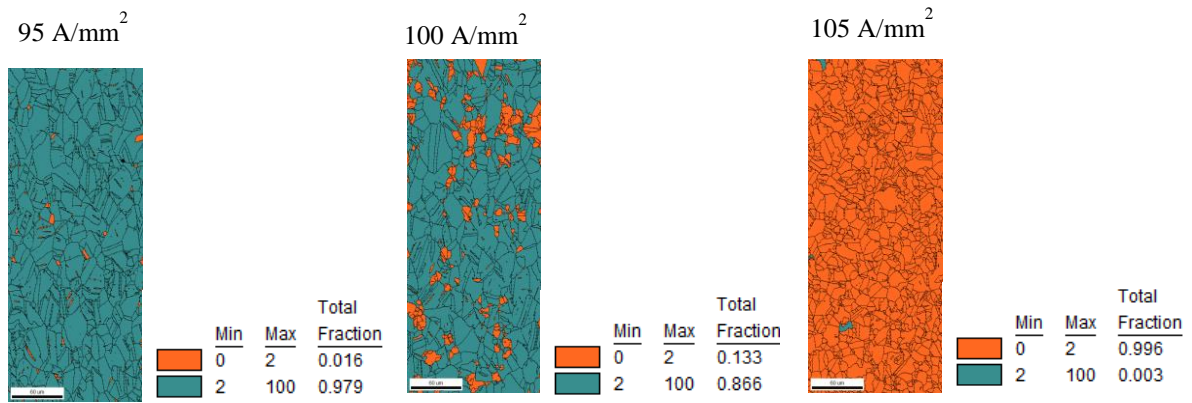
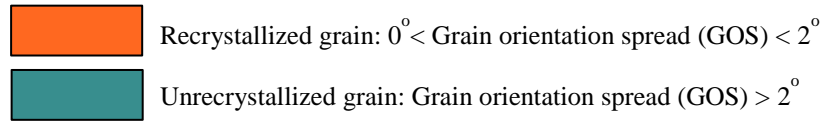
Figure 3. 8 Full width at half maximum (FWHM) profiles of specimens with (a) 20% prestrain and (b) 60% prestrain



(a)



(b)



(c)

Figure 3. 9 Electron backscatter diffraction system (EBSD) inverse pole figures for normal direction (ND) and kernel average misorientation (KAM) maps of specimens with (a) 20% prestrain and (b) 60% prestrain for various electric current densities; (c) Grain orientation spread (GOS) maps of specimens with 60% prestrain for various electric current densities

3.4 CONCLUSION

In the present study, the effects of a single pulse of electric current on the mechanical behavior and microstructure of a commercially available SUS316L were investigated to evaluate the feasibility of a two-stage forming process with rapid EA annealing in less than 1 sec. The mechanical behavior of the prestrained specimen after applying a single pulse of electric current to the specimen suggests the occurrence of EA annealing. The results of microstructural analysis show the annihilation of dislocations by the electric current, confirming the occurrence of EA annealing. The experimental results show that the effectiveness of EA annealing strongly depends not only on the electric current parameters, but also the magnitude of the prestrain. Depending on the electric current parameters and the magnitude of the prestrain, full annealing with recrystallization was even possible to significantly increase the total maximum achievable elongation of the specimen. The results of the present study suggest that a two-stage forming process of SUS316L can be simplified and expedited by properly implementing rapid EA annealing in the process. As a final remark, in the present feasibility study, the duration of electric current was fixed for simplicity. However, for optimization of a practical dual-stage forming process with rapid EA annealing, a further study with expanded electric current parameter combinations with different electric current durations may be necessary.

References

- Acar, M.O., Fitzpatrick, M.E., 2017. Determination of plasticity following deformation and welding of austenitic stainless steel. *Materials Science and Engineering: A* 701, 203–213.
- Anderson, M., Gholipour, J., Bridier, F., Bocher, P., Jahazi, M., Savoie, J., Wanjara, P., 2013. Improving the Formability of Stainless Steel 321 through Multistep Deformation for Hydroforming. *Transactions of the Canadian Society for Mechanical Engineering* 37, 39–52.
- Andrade, M.S., Gomes, O.A., Vilela, J.M.C., Serrano, A.T.L., Moraes, J.M.D. de, 2004. Formability evaluation of two austenitic stainless steels. *Journal of the Brazilian Society of Mechanical Sciences and Engineering* 26, 47-50.
- Cho, S.-H., Yoo, Y.-C., 2001. Static recrystallization kinetics of 304 stainless steels. *Journal of Materials Science* 36, 4273 – 4278.
- Conrad, H., 2000a. Electroplasticity in metals and ceramics. *Materials Science and Engineering: A* 287, 276–287.
- Conrad, H., 2000b. Effects of electric current on solid state phase transformations in metals. *Materials Science and Engineering: A* 287, 227–237.
- Hong, S.-T., Jeong, Y.-H., Chowdhury, M.N., Chun, D.-M., Kim, M.-J., Han, H.N., 2015. Feasibility of electrically assisted progressive forging of aluminum 6061-T6 alloy. *CIRP Annals* 64, 277–280.
- Jeong, H.-J., Park, J., Jeong, K.J., Hwang, N.M., Hong, S.-T., Han, H.N., 2018. Effect of Pulsed Electric Current on TRIP-aided steel. *International Journal of Precision Engineering and Manufacturing-Green Technology* (in press).

- Kim, M.-J., Lee, K., Oh, K.H., Choi, I.-S., Yu, H.-H., Hong, S.-T., Han, H.N., 2014a. Electric current-induced annealing during uniaxial tension of aluminum alloy. *Scripta Materialia* 75, 58–61.
- Kim, M.-J., Lee, M.-G., Hariharan, K., Hong, S.-T., Choi, I.-S., Kim, D., Oh, K.H., Han, H.N., 2017. Electric current–assisted deformation behavior of Al-Mg-Si alloy under uniaxial tension. *International Journal of Plasticity* 94, 148–170.
- Kim, M.-S., Vinh, N.T., Yu, H.-H., Hong, S.-T., Lee, H.-W., Kim, M.-J., Han, H.N., Roth, J.T., 2014b. Effect of electric current density on the mechanical property of advanced high strength steels under quasi-static tensile loads. *International Journal of Precision Engineering and Manufacturing* 15, 1207–1213.
- Magargee, J., Morestin, F., Cao, J., 2013. Characterization of Flow Stress for Commercially Pure Titanium Subjected to Electrically Assisted Deformation. *Journal of Engineering Materials and Technology* 135, 041003.
- Okazaki, K., Kagawa, M., Conrad, H., 1978. A study of the electroplastic effect in metals. *Scripta Metallurgica* 12, 1063–1068.
- Park, J.-W., Jeong, H.-J., Jin, S.-W., Kim, M.-J., Lee, K., Kim, J.J., Hong, S.-T., Han, H.N., 2017. Effect of electric current on recrystallization kinetics in interstitial free steel and AZ31 magnesium alloy. *Materials Characterization* 133, 70–76.
- Peterson, S.F., Mataya, M.C., Matlock, D.K., 1997. The formability of austenitic stainless steels. *The Journal of The Minerals, Metals & Materials Society* 49, 54–58.
- Roh, J.-H., Seo, J.-J., Hong, S.-T., Kim, M.-J., Han, H.N., Roth, J.T., 2014. The mechanical behavior of 5052-H32 aluminum alloys under a pulsed electric current. *International Journal of Plasticity* 58, 84–99.

- Roth, J.T., Loker, I., Mauck, D., Warner, M., Golovashchenko, S.F., Krause, A. 2008. Enhanced Formability of 5754 Aluminum Sheet Metal Using Electric Pulsing. Presented at the North American manufacturing research conference 36, 405-412.
- Salandro, W.A., Jones, J.J., McNeal, T.A., Roth, J.T., Hong, S.-T., Smith, M.T., 2010. Formability of Al 5xxx Sheet Metals Using Pulsed Current for Various Heat Treatments. *Journal of Manufacturing Science and Engineering* 132, 051016.
- Thanakijkasem, P., Uthaisangsuk, V., Pattarakun, A., Mahabunphachai, S., 2014. Effect of bright annealing on stainless steel 304 formability in tube hydroforming. *The International Journal of Advanced Manufacturing Technology* 73, 1341–1349.
- Thien, N.T., Jeong, Y.-H., Hong, S.-T., Kim, M.-J., Han, H.N., Lee, M.-G., 2016. Electrically assisted tensile behavior of complex phase ultra-high strength steel. *International Journal of Precision Engineering and Manufacturing-Green Technology* 3, 325–333.
- Ungár, T., Borbély, A., 1996. The effect of dislocation contrast on x-ray line broadening: A new approach to line profile analysis. *Applied Physics Letters* 69, 3173–3175.
- Williamson, G.K., Hall, W.H., 1953. X-ray line broadening from fcc aluminium and wolfram. *Acta Metallurgica* 1, 22–31.
- Xu, Z.S., Lai, Z.H., Chen, Y.X., 1988. Effect of Electric Current on the Recrystallization Behavior of Cold Worked α – Ti 22, 187–190

CHAPTER IV

ELECTRICALLY ASSISTED SUBSECOND ANNEALING OF PRESTRAINED 304 AUSTENITIC STAINLESS STEEL SHEETS

ABSTRACT

The post-annealing tensile behavior of prestrained austenitic 304 stainless steel (SUS304) sheets under a single pulse of electric current is experimentally investigated. A prestrained specimen is applied a single pulse of electric current with a short duration during annealing time and then tested for post-annealing mechanical properties. The post-annealing stress-strain curve during reloading shows that the flow stress of the SUS304 significantly decreases, while the maximum achievable elongation significant increases with increasing electric current. The microstructural analysis confirms the occurrence of the electrically induced annealing and reused benefits of mechanically induced martensitic transformation (MIMT). The post-annealing mechanical property and the microstructure of the SUS304 strongly depend on the prestrain and the magnitude of current density. The result of the present study will be used to improve the formability of the SUS304 in sheet metal forming processes with electric current.

Keywords: electrically assisted annealing; electric current; prestrain; stainless steels

4.1 INTRODUCTION

Austenitic stainless steels (ASSs) are the most commonly and widely used stainless steels. ASSs are commonly used for industrial applications due to their good formability, excellent corrosion resistance and good welding properties (McGuire, 2008; Padilha et al., 2003). These steels may present mechanically induced martensitic transformation (MIMT) during deformation, which can increase their mechanical strength and improve their formability. Such phenomena are known as TRIP effect (Han et al., 2008; Rocha and Oliveira, 2009; Geijselaers and Perdahcioğlu, 2009). However, the good formability of ASSs is not satisfactory (Anderson et al., 2013; Thanakijkasem et al., 2014) in some industrial applications due to the shapes of final products made of ASSs are becoming increasingly complicated. For example, in tube hydroforming of exhaust systems using ASSs, the forming process is composed of an intermediate heat treatment between the multiple- (or two-) forming stages, due to the formability of the ASSs.

Recently, furnace annealing between forming stages has been developed to address the formability of ASSs, which includes a two- or multiple- stage. In this process, a pre-deformed part is annealed at an elevated temperature (800-1100°C) for a specific duration to eliminate or reduce the effects of strain hardening before the next forming stage. However, the conventional heat treatment using a furnace is time-consuming and costly. Thus, an effective method with the rapid process is needed to control the formability of ASSs.

To overcome with these problems, electrically assisted manufacturing (EAM) is a promising metal forming technique, in which electric current can influence the mechanical and microstructural behavior of materials (Machlin, 1959; Troitskii, 1969; Okazaki et al., 1978). Note that the effect of the electric current on the metals during deformation is often called electroplastic effect. Many researchers have carried out researches to understand the electroplastic effect on the mechanical behavior and microstructure (Okazaki et al., 1978;

Conrad et al., 1983, 1988; Conrad, 2000a; Kim et al., 2014a; Lin et al., 2015; Kim et al., 2017; Park et al., 2017). Conrad et al. (2000) conducted a series of extensive studies on the effect of the pulsed electric current in various metals, supporting the fact that high electric current can clearly enhance the ductility of metals. Kim et al. (2014a) also observed the acceleration of dislocation annihilation by applying pulsed electric current during tensile tests of aluminum alloys and reported that the pulsed electric current was significantly increased the elongation. Also, Conrad et al. (1983,1988) reported that the pulsed electric current strongly affected the recrystallization kinetics of pure copper. Lin et al. (2015) reported that the dynamic recrystallization temperature of AZ31 alloy was obviously decreased under the electric current. More recently, Park et al. (2017) reported that the annealing temperature and time for recrystallization of interstitial free (IF) steel and AZ31 magnesium alloy were significantly reduced by electropulsing treatment (EPT) compared to conventional heat treatment with a furnace. However, it also needs to be noted that for specific metal alloys and experimental conditions, the effect of the pulsed electric current on formability gives an adverse effect on the formability (Jeong et al., 2018; Mai et al., 2011). Mai et al. (2011) applied the electric current to stainless steel 316L during deformation and reported that the ductility was significantly reduced with increasing electric current density, despite the reduction in flow stress. Jeong et al. (2018) investigated the effect of electric current on the tensile behavior of transformation induced plasticity (TRIP)-aided steel and reported that the elongation of TRIP-aided steel significantly decreased by applying a pulsed electric current during tensile deformation. According to Jeong et al. (2018), the effectiveness of electric current on the tensile behavior of selected TRIP-aided steel depends on designing the pulsing pattern of the electric current in accordance with the metal alloys.

It is obvious that the formability of the metal alloy generally enhances with applying a pulsed electric current to a metal alloy during deformation, it may not be feasible to design a

commercial metal forming process with a pulsed electric current. The cycle time of the process may be significantly increased and/or the structure of forming equipment may become quite complex. Recently, several studies on EAM or electroplastic have reported that the mechanical properties of metal can be altered or modified by only applying a single pulse electric current at specific deformation (Kim et al., 2014b; Thien et al., 2016a; Luu et al., 2018). Thien et al. (2016) applied a single pulse electric current with a short duration time to a complex phase ultra-high strength steel at a specific prestrain and reported that the flow stress significantly decreased and the formability increased during reloading. Luu et al. (2018) also applied a single pulse electric current to a 316L stainless steel between two deformation stages in the tensile test and reported that the formability significantly enhanced with rapid electrically assisted annealing. Also, Luu et al. (2018) indicated that the improvement formability of the selected metal strongly depended on the prestrain and current density.

However, studies on the mechanical behavior and microstructure with electrically assisted (EA) subsecond annealing between plastic deformation are still quite limited, especially for the ASSs. In the present study, the effect of EA subsecond annealing on mechanical properties and microstructure of a commercial available 304 austenite stainless steel (SUS304) is investigated.

4.2 EXPERIMENTAL SET-UP

Commercial 1 mm thick grade 304 austenite stainless steel (SUS304) sheet was used for the experiments. The chemical composition of the SUS304 is listed in Table 4.1. Note that the selected ASS is a metastable austenitic stainless steel and frequently occurs martensitic transformation during deformation. Typical tensile specimens (ASTM-08) with a gage width of 12.5 mm and a gage length of 50 mm were fabricated by laser cutting along the rolling direction of the sheet.

A preform annealing of the selected SUS304 with rapid EA subsecond annealing was simply conducted by quasi-static tensile tests with a single pulse of electric current, as schematically described in Figure 4.1. The quasi-static tensile test was conducted using a universal testing machine with a constant displacement rate of 2.5 mm/min. The baseline tensile test was implemented by simply deform a specimen by uniaxial tension until fracture. For the quasi-static tensile test with EA subsecond annealing, a tensile specimen is firstly performed to a specified prestrain by the uniaxial tension. A single pulse of electric current was then applied to the prestrained specimen to induce annealing, according to the electric parameters listed in Table 4.2. Subsequently, the specimen was cooled down to room temperature in air and unloaded. Finally, the specimens were reloaded until fracture. Note that the post-annealing elongation and post-annealing yield strength were measured using standard uniaxial tensile tests, which were performed at room temperature with a constant displacement rate of 2.5 mm/min.

Materials	Chemical composition (wt. %)						
	Fe	Cr	Si	Ni	C	Mo	Mn
SUS304	Bal.	18.82	0.39	7.85	0.037	-	1.33

Table 4. 1 The chemical composition of SUS304 sheets from EPMA analysis

Sorts	Materials	Current density* (A/mm ²)			Duration (sec)	Prestrain (%)
Tensile test	SUS304	95	100	105	0.75	20 and 60

*Based on the actual cross-sectional area of the specimen at the given prestrain level

Table 4. 2 Experimental parameters

For EA subsecond annealing, the electric current was generated by a Vadal SP-1000U power supply (Hyosung, South Korea) with a programmable pulse controller. The tensile test machine was insulated from the electric current by inserting bakelite between the specimen and each grip, which was described previously by Luu et al. (2018). The force history during the experiment was measured by a CSDH load cell (Bongshin, South Korea) with a maximum capacity of 250 kN as a function of time using a PC-based data acquisition system (Figure 4.1(b)). The displacement history was measured using a laser extensometer (LX500, MTS, USA) by attaching retro-reflective tape (MTS) to the specimen. Finally, an infrared thermal imaging camera (T621, FLIR, Sweden) was employed to monitor the temperature change of the specimen throughout the experiment. Note that one side of the specimen was sprayed with black thermal paint to stabilize the emissivity and thus to improve the accuracy of the temperature measurement. The emissivity was calibrated by comparing the measured temperature using a k-type thermocouple. The temperature was measured for the middle part of the specimen, which is the highest temperature part when the electric current was applied to the specimen.

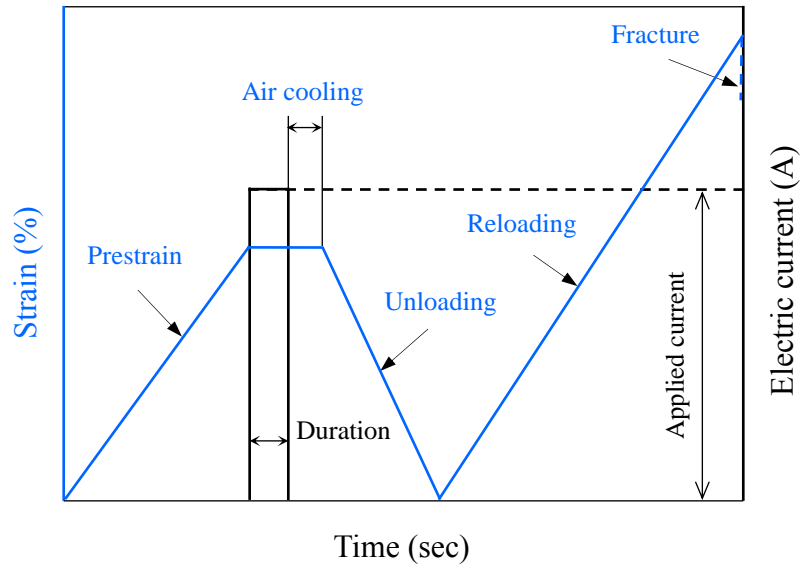
For the parameter study, two different prestrain levels were combined with three different true electric current densities, as listed in Table 4.2. Note that the selected prestrain in the present study were deformed to 20% and 60% of uniform elongation, respectively, from the tensile test of baseline specimen (without prestrain and electric current), as marked in Figure 4.2. In order to maintain a constant electric current density based on the initial cross-sectional area of the specimen, a different amplitude of electric current was applied to the specimen considering the decrease in cross-sectional area of the specimen at each specified prestrain, as the term “true” indicated. To verify the repeatability of the results, at least three specimens were tested for each parameter set.

As mentioned above, the true electric current density at different prestrain (ρ_i) based on the actual cross-sectional area (A_i) of the specimen at the given prestrain level as

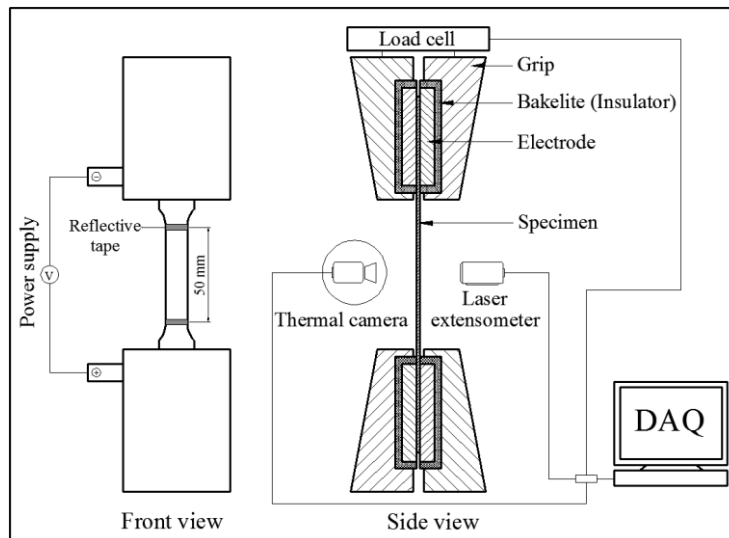
$$\rho_i = \frac{I}{A_i} \quad (1) \quad \text{and} \quad A_i = \frac{A_o}{(1 + \varepsilon_i)} \quad (2)$$

Where I , A_o , and ε_i present the magnitude of current density (in A), the cross-sectional area of the baseline (or original specimen) (in mm²), and engineering strain of the specimen at the given prestrain, respectively.

A baseline specimen and prestrained specimens after EA subsecond annealing were prepared for microstructural analysis. Note that the prestrained specimen with EA subsecond annealing were removed from the test without reloading to fracture. The microstructure of the specimens was characterized by electron probe microanalyzer (EPMA, JXA-8530F, JEOL Ltd., Japan) analysis and a field emission gun scanning electron microscope (FE-SEM, SU70, Hitachi, Japan) equipped with EBSD system (EDAX/TSL, Hikari, USA). To evaluate the change in dislocation density by the EA subsecond annealing, the full width at half maximum (FWHM) of the diffraction peak was measured with an X-ray diffractometer (D8-Advance, BRUKER MILLER Co, Japan) using a radiation source of Cu operating at 50 kV at room temperature. The diffraction patterns were recorded in the scan range of 40-85 deg. with a scan speed of 1 deg./min and could be fitted well with the Pearson VII function. Specimens for microstructure observation were prepared by mechanical grinding followed by electropolishing with a 80ml perchloric acid, 90ml distilled water, and 730 ml ethanol solution at 18V. For EBSD analysis, the accelerating voltage and scan step size were 15 kV and 0.5 μm , respectively. The critical misorientation angle was set to 15° for grain identification.



(a)



(b)

Figure 4. 1 Schematics of (a) EA annealing with a single pulse of electric current and (b) the experimental set-up

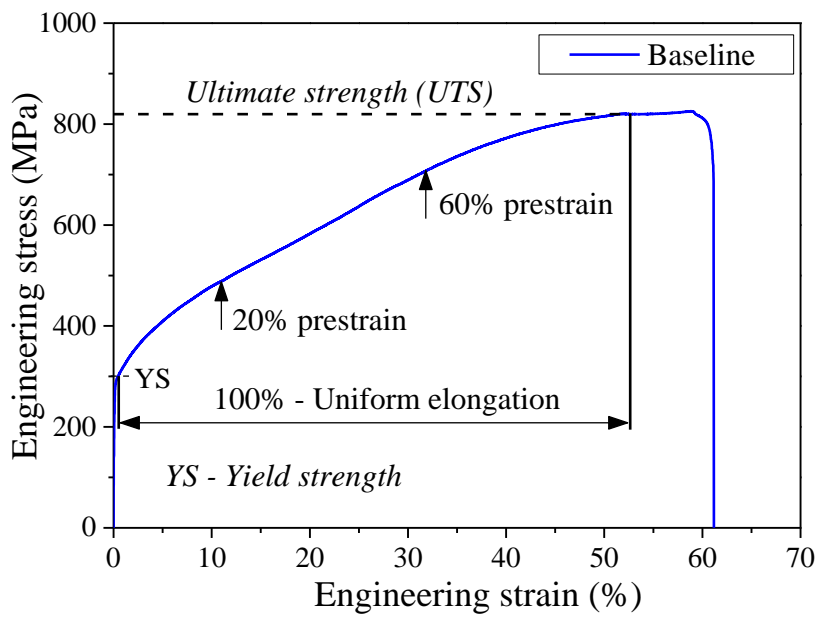


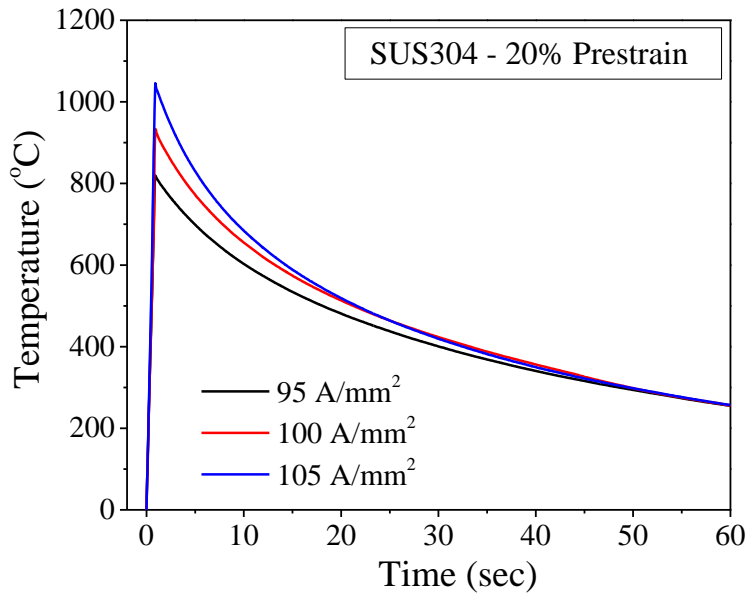
Figure 4. 2 A stress-strain curve of a baseline specimen

4.3 RESULTS AND DISCUSSION

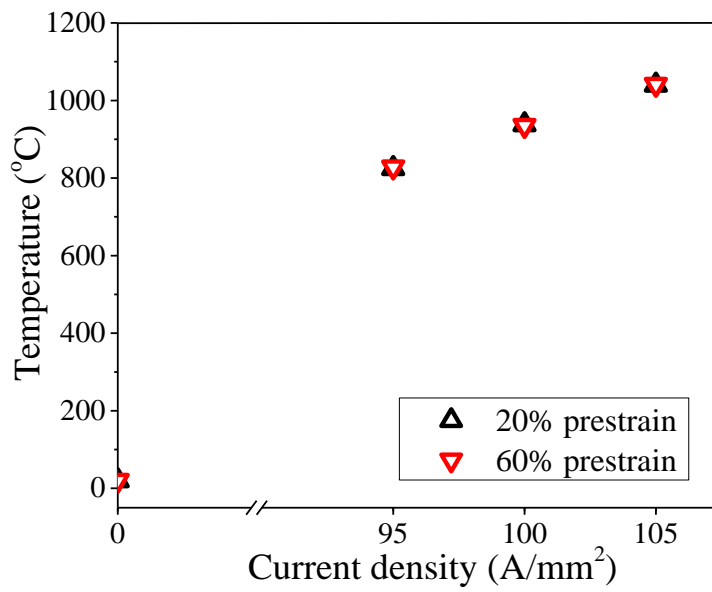
The measured specimen temperature during EA subsecond annealing is presented in Figure 4.3. As representative temperature histories of the 20% prestrained specimens are shown in Figure 4.3(a), the specimen temperature rapidly increased the maximum temperature by the resistance heating (Joule heating effect). After applying the electric current, the specimen temperature decreased by air cooling. Note that the temperature was measured at the center of the specimen, which showed the highest temperature when the electric current was applied. Normally, the peak temperatures increased as the electric current density increased as shown in Figure 4.3(b). Also, the effect of two different prestrains on the peak temperature was insignificant.

Figure 4.4(a) shows the EBSD inverse pole figure (IPF) and phase maps for the SUS304. The different colors in the IPF map indicate the orientation of each grain with respect to the normal direction (ND). The baseline specimen consists of austenitic phase (green area) with a small area of martensitic phase (red area). Note that the martensitic phase was insignificant in the baseline specimen. The average grain size of the austenite phase in baseline specimen was $17.0 \pm 5.9 \mu\text{m}$, which was measured from EBSD analysis.

The flow curve and strain hardening rate (SHR) of the baseline specimen are plotted as shown in Figure 4.4(b). The strain hardening rates of the baseline specimen show a sigmoidal or S-shaped, which is decreased to minimum point and then increase with straining. As marked in the figure, the minimum point of the SHR is well known to be an active point of mechanically induced martensitic transformation (MIMT) and related with the minimum strain needed for α' martensite formation (Huang et al., 1989; Mertinger et al., 2008). Moreover, the point of intersection between the flow curve and the SHR indicates the onset of necking in the tensile test of the specimen (Figure 4.4(b)). It could be used to predict the uniform elongation and tensile strength (Han et al., 2008, 2009).

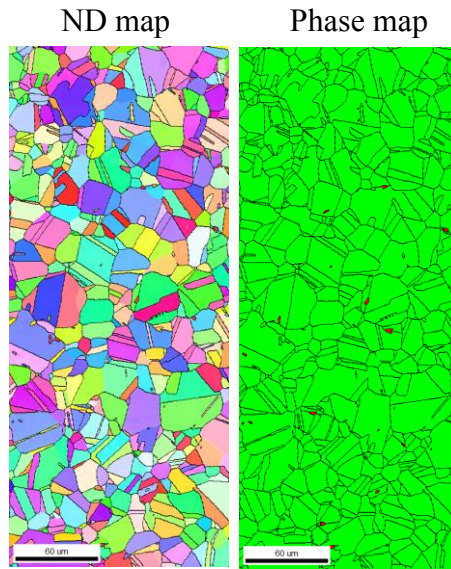


(a)

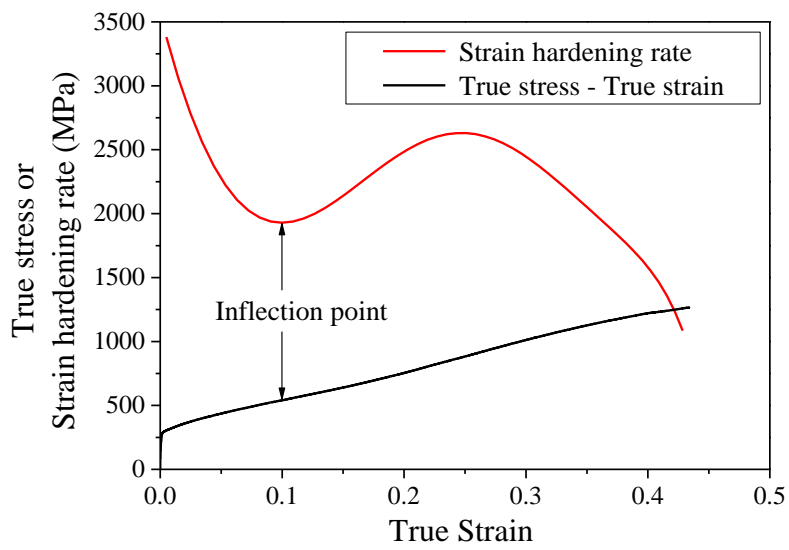


(b)

Figure 4. 3 Temperature histories of 20% prestrained specimens and (b) the peak temperatures as functions of current density during EA annealing for different prestrains



(a)



(b)

Figure 4. 4 (a) Inverse pole figure maps of baseline specimen for grain size determination.

The grain size of baseline specimen is $17.0 \pm 5.9 \mu\text{m}$; (b) a true stress and strain hardening

rate as a function of true strain of a baseline specimen

The reloading engineering stress-strain curves after EA subsecond annealing in both prestrains are shown in Figure 4.5. Note that the reloading engineering stress-strain was calculated based on the gage length and cross-sectional area at each prestrain. As expected, the 0.2% yield strengths during reloading mostly showed higher values than the baseline yield strength without prestrain due to strain hardening for both prestrains. With the same reason, the elongations at fracture during reloading (the post-annealing elongation) for both prestrains mostly showed lower values than the baseline elongation at fracture without prestrain. As the current density was increased in both magnitudes of prestrain, 20% and 60%, the experimental results clearly show that the flow stress of the SUS304 gradually decreased, which indicates the occurrence of electrically induced annealing (Kim et al., 2014a, 2017). Also, the post-annealing elongation clearly increased with increasing the current density.

The post-annealing yield strength and post-annealing elongation can be plotted as functions of current density (Figures 4.6(a) and (b), respectively). The experimental results suggest that the effect of EA subsecond annealing on the mechanical behavior during reloading is significantly different depending on the magnitude of the prestrain, even with the same true current density and nearly identical peak temperatures. With higher prestrain, as shown in Figures 4.6(a) and (b), the effect of EA subsecond annealing becomes more pronounced. Especially, the post-annealing yield strength and post-annealing elongation change more rapidly with the higher prestrain, as the current density increases with the constant duration of electric current.

For evaluation of the effect of EA subsecond annealing on the uniform elongation of SUS304 during reloading, the onset of necking was determined by the points of intersection between the flow curve and the SHR as a function of the true strain at various current densities, as shown in Figure 4.7. As expected, the intersection of the strain hardening rates and stress-strain curves is shifted to higher strains with increasing current densities. Consequently, the

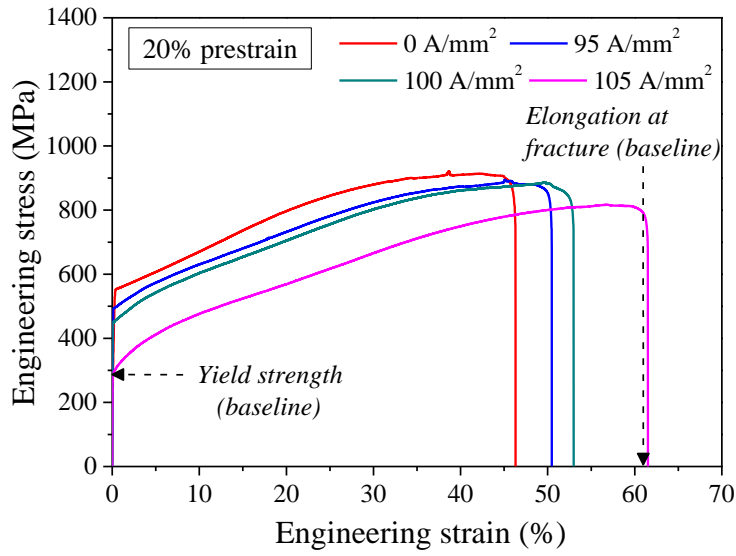
uniform elongation of prestrained specimens after EA subsecond annealing significantly increase as current density increased. This result reveals that the onset of necking at the given strain was significantly delayed by the electric current during the EA subsecond annealing. Hence, the strain hardening rates of prestrained specimens after the EA subsecond annealing show a sigmoidal or S-shape (Figure 4.7), which are a similar shape with the SHR of baseline specimen. It is interestingly noted that the strain hardening rates of the prestrained specimen after the EA subsecond annealing were changed one more times during reloading in both prestrains.

The effectiveness of EA subsecond annealing on the formability of the SUS304 can be future evaluated by comparing the total achievable displacement or total achievable elongation based on the original gage length of the baseline specimen. The total achievable displacement and total achievable elongation can be simply calculated as

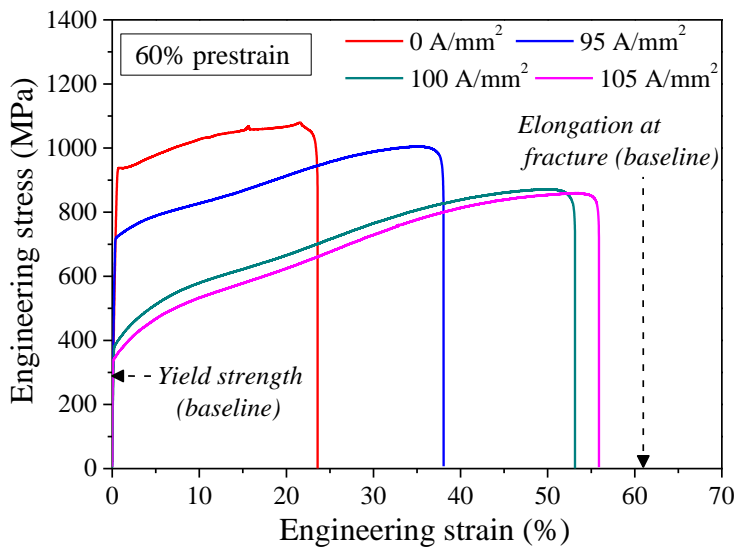
Total achievable displacement = displacement by prestrain + displacement during reloading

Total achievable elongation = total achievable displacement/the gage length of the baseline specimen

Total achievable elongation as a function of current density clearly seen in Figures 4.8(a) and (b) confirms that EA subsecond annealing at higher prestrain is beneficial to improve formability of the given metal alloy. Especially, at both current densities of 100 and 105 A/mm², the total achievable elongation with the 60% prestrain was approximately 1.3 times higher than with the 20% prestrain (Figures 4.8(a) and (b)). Note that the total achievable elongation with the 20% prestrain and current density of 95 A/mm² still exceeded that of the baseline tensile test.

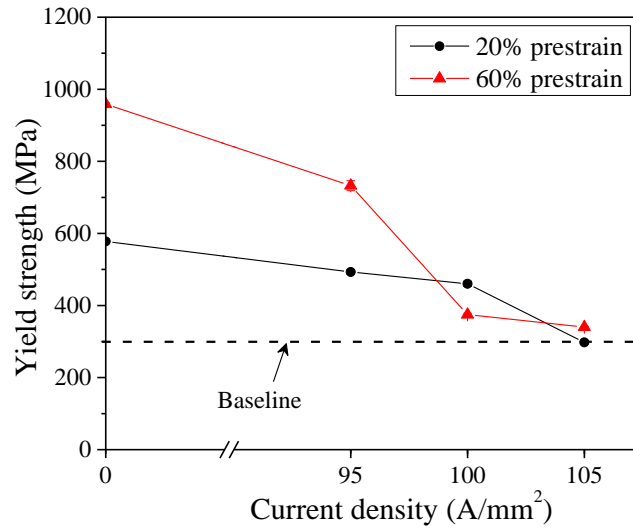


(a)

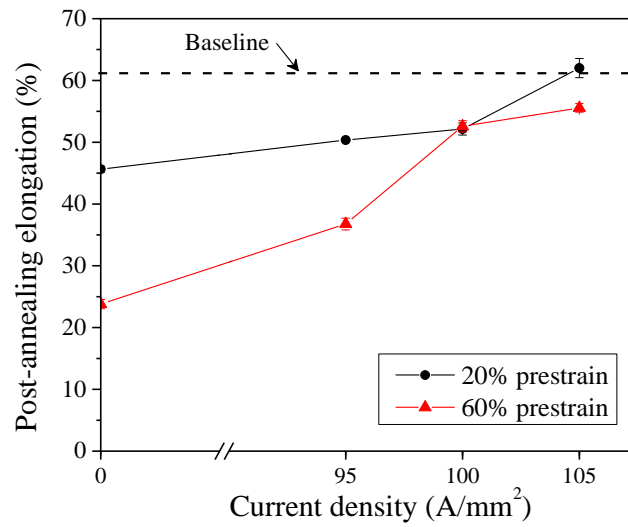


(b)

Figure 4. 5 Engineering stress-strain curves after EA annealing with (a) 20% prestrain and (b) 60% prestrain; the engineering stress-strain curves during reloading was constructed based on the gage length and the cross-sectional area at each prestrain

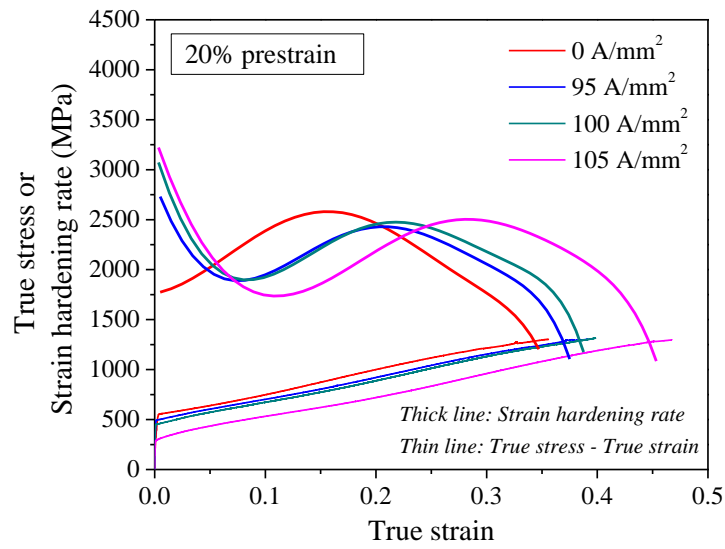


(a)

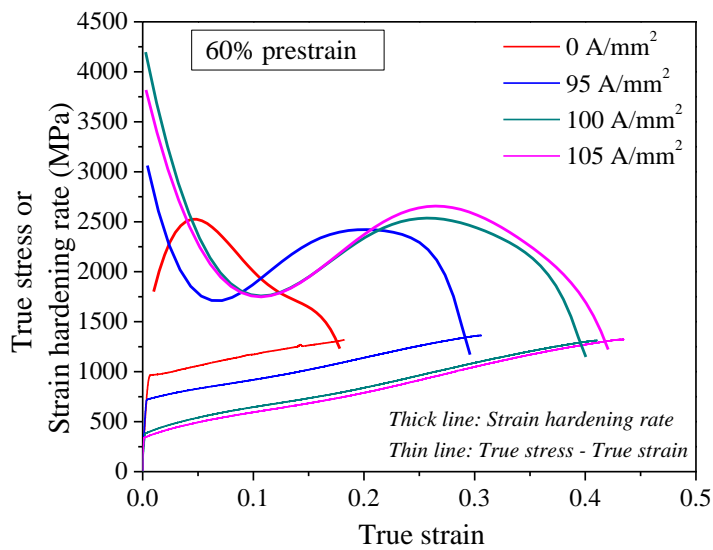


(b)

Figure 4. 6 (a) Post-annealing yield strength and (b) post-annealing elongation of prestrained specimens after EA annealing

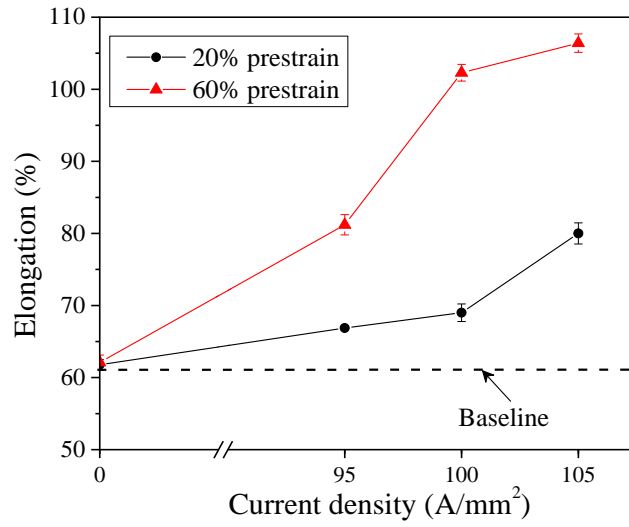


(a)

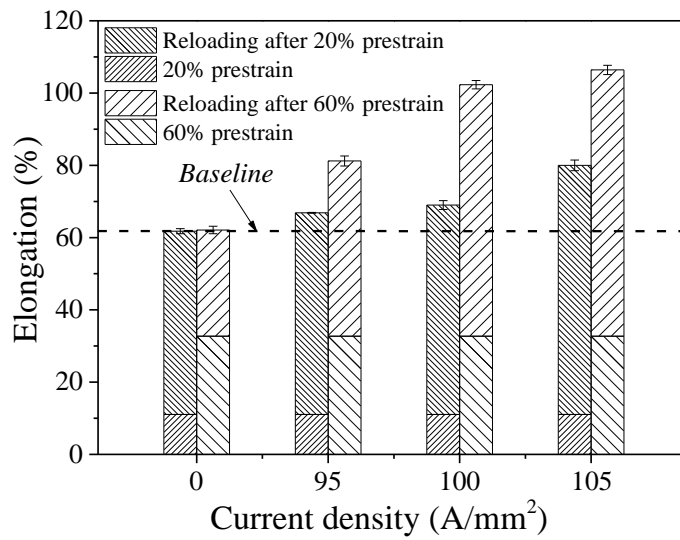


(b)

Figure 4. 7 The flow curves and strain hardening rates with respect to true strain at different prestrain of SUS304 after EA annealing for (a) 20% prestrain and (b) 60% prestrain



(a)



(b)

Figure 4. 8 (a) Total achievable elongation as a function of current density and (b) the effect of prestrain and the current density on the total achievable elongation; the total achievable elongation was calculated based on the original gage length of the baseline specimen

As presented above, the mechanical behavior of the SUS304 during reloading after a short duration of electric current strongly suggests the occurrence of EA subsecond annealing. To confirm this occurrence of EA subsecond annealing, FWHM analysis of the diffraction peak profile is a well-established (Kim et al., 2017). Typically, diffraction peak profile is broadened when the crystal lattice is distorted by lattice defects, especially by dislocations (Williamson and Hall, 1953; Ungár and Borbély, 1996). In the present study, since the instrumental effect could be assumed to be the same in all specimens due to the identical operational conditions, the FWHM analysis was closely related to the density of lattice defect including dislocation in the specimen. As shown in Figure 4.9, the FWHM values decreased with increasing current density in both selected prestrains. The results clearly confirm the reduction of dislocation density (annihilation of dislocation) in the prestrained specimen by the applied electric current (Figure 4.9), which is EA subsecond annealing. It should be noted that for 60% prestrain, the FWHM values show that the specimen was fully annealed to the baseline status without prestrain when the electric current densities of 100 and 105 A/mm² were applied, while full annealing for 20% prestrain was achieved at only 105 A/mm². The results suggest that the specimens after EA subsecond annealing with high prestrain level could be earlier achieved full annealing than that of the specimen with low prestrain level. The results of the FWHM analysis are in good agreement with the observed mechanical behavior during reloading after EA subsecond annealing in Figures 4.5-4.8.

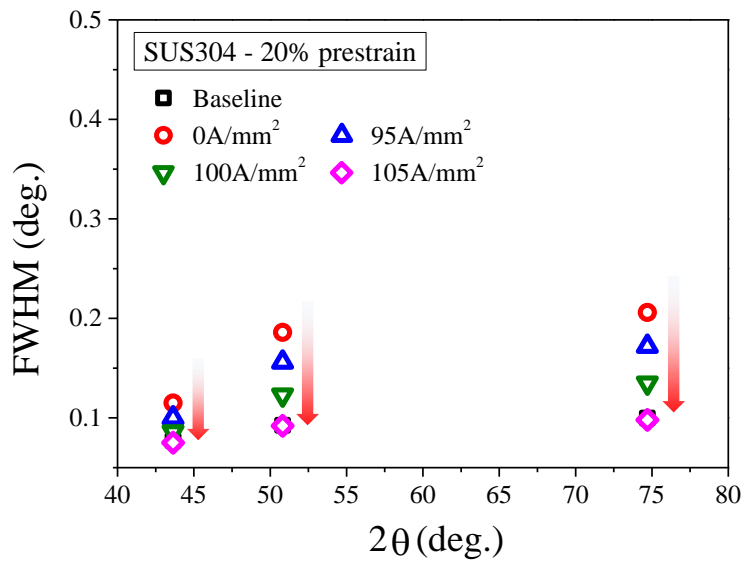
The X-ray diffraction patterns of baseline specimen and prestrained specimens after EA subsecond annealing at two different prestrain levels are presented as shown in Figure 4.10. As expected, the reflected lines of (111), (200) and (211) planes of the γ -austenitic phase observed without appearing of α' -martensitic phase for the 20% prestrained specimen (Figure 4.10(a)). In contrast, for 60% prestrain, the γ -austenitic phase and the α' -martensitic phase with the reflected line of (110), (200) and (211) planes were detected. It clearly shows that the

martensitic phase occurred during deformation of the SUS304 at higher prestrain specimen or the occurrence of MIMT effect during prestrained specimen (during first stage forming). As current density increased, the peak of α' -martensitic phase was vanished, as shown in Figure 4.10(b). This result suggests that the α' -martensitic phase was completely reverted to γ -austenitic phase during EA subsecond annealing.

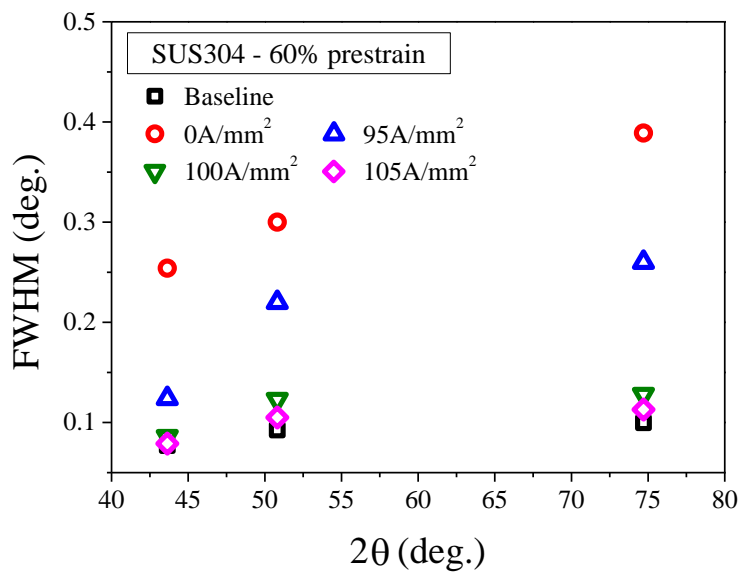
Figure 4.11 shows the EBSD inverse pole figure (IPF) and phase maps for the SUS304 at two different prestrains with various current densities. As shown in the figure, the red area is well-known martensite in the specimen. The volume fraction of the martensitic phase is approximated 16% in the 60% prestrained specimens before EA subsecond annealing (Figure 4.11(b)), while the volume fraction of martensite was insignificant in the 20% prestrained specimens before EA subsecond annealing (Figure 4.11(a)). This result shows a good agreement with the X-ray diffraction results (Figure 4.10) and the repeated shape of the SHR of the baseline specimen (Figure 4.7). However, it is interestingly noted that the occurrence of martensite during deformation completely vanished (or reversed to austenite) (Guy et al., 1983; Smith and West, 1973) after EA subsecond annealing (Figure 4.11(b)), even at the applied current density of 95 A/mm². By applied current density of 95 A/mm², the peak temperature of the 60% prestrained specimen reached approximately 820°C which induced the transformation of the martensite to the austenite (McGuire, 2008). This result suggests that the martensitic phase was changed during the prestrain and EA subsecond annealing. As a result, the benefits of MIMT in 60% prestrain during reloading tensile test can be reused due to the resetting martensite to austenite during EA subsecond annealing of the prestrained specimen. However, the occurrence of MIMT and reused MIMT strongly depend on the given prestrain and need to be carefully decided to optimize the effect of MIMT and EA subsecond annealing in the process.

Figure 4.12 and 4.13 show kernel average misorientation (KAM) maps and grain orientation spread (GOS) maps of each specimen. As mentioned in chapter III, the KAM maps

display effects, which can be interpreted as dislocations. The average KAM value of the 60% prestrained specimens was significantly reduced from 1.35 (for 0 A/mm²) to approximately 0.53 (for 100 A/mm² and 105 A/mm²). The average grain size of the 60% prestrained specimen was also significantly reduced under the condition of 100 and 105 A/mm². The results indicate that recrystallization occurred in 60% prestrained specimen after the EA subsecond annealing with the current densities of 100 and 105 A/mm². For the GOS maps, the recrystallized area was identified based on the GOS values obtained from EBSD measurement and the criterion of GOS value for identifying recrystallized grain was set to below 2⁰. The recrystallized area fractions were approximately 92.6% (for 100 A/mm²) and 98.7% (for 105 A/mm²), which confirm the recrystallization in the 60% prestrained specimen after EA subsecond annealing under the condition of 100 and 105 A/mm². As current density increased from 100 A/mm² to 105 A/mm², the average grain size of the 60% prestrained specimen was slightly increased from 10.5 ± 3.6 to 14.3 ± 5.1 μm, which relates to the grain growth during annealing (Padilha et al., 2003). Note that the temperature peaks of 100 A/mm² and 105 A/mm² were significantly increased, as shown in Figure 4.3. However, there is no recrystallization occurred during EA annealing in 20% prestrained specimens, even with the applied electric current of 105 A/mm². These results indicate that the dislocation density induced by the 60% prestrain was high enough to provide driving force to result in the rapid recrystallization (Park et al., 2017) during the EA subsecond annealing with the current densities 100 and 105 A/mm². No significant changes in the grain size were observed for the other combinations of the prestrain and the current density considered in the present study.

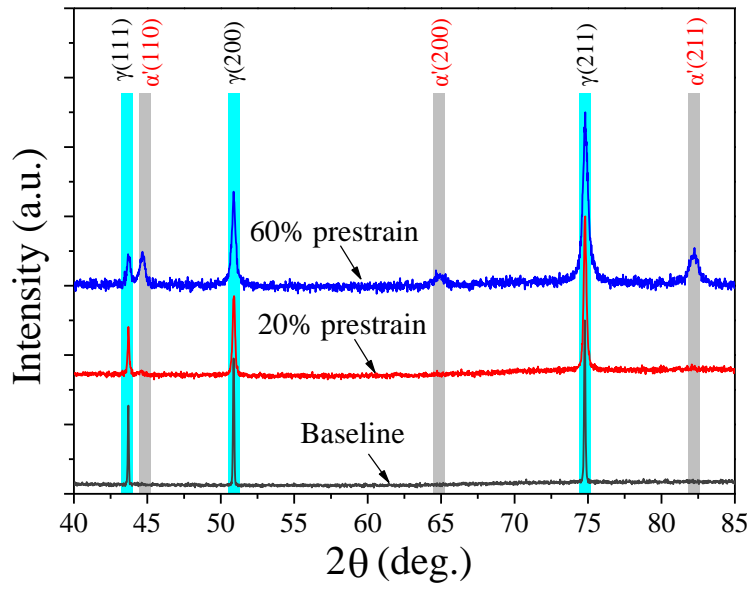


(a)

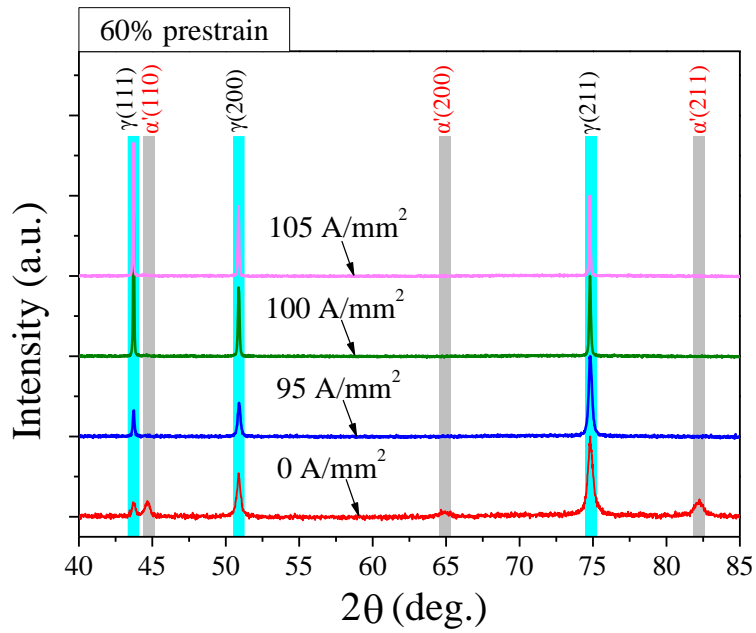


(b)

Figure 4. 9 FWHM profiles of specimens with (a) 20% prestrain and (b) 60% prestrain

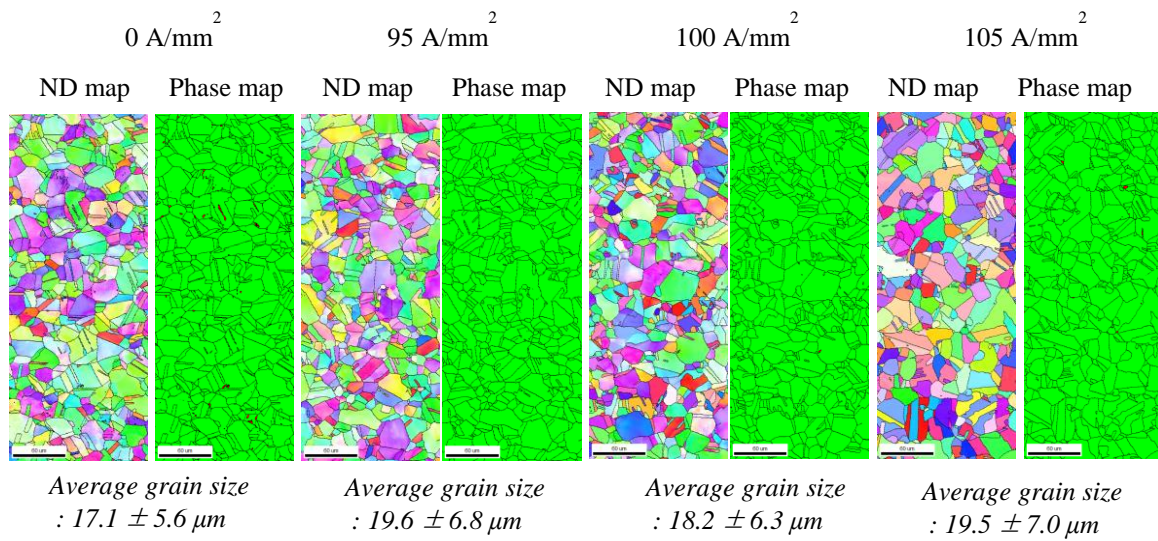


(a)

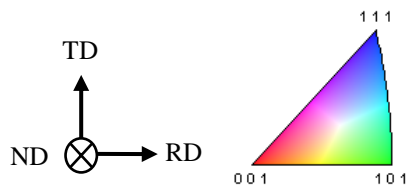
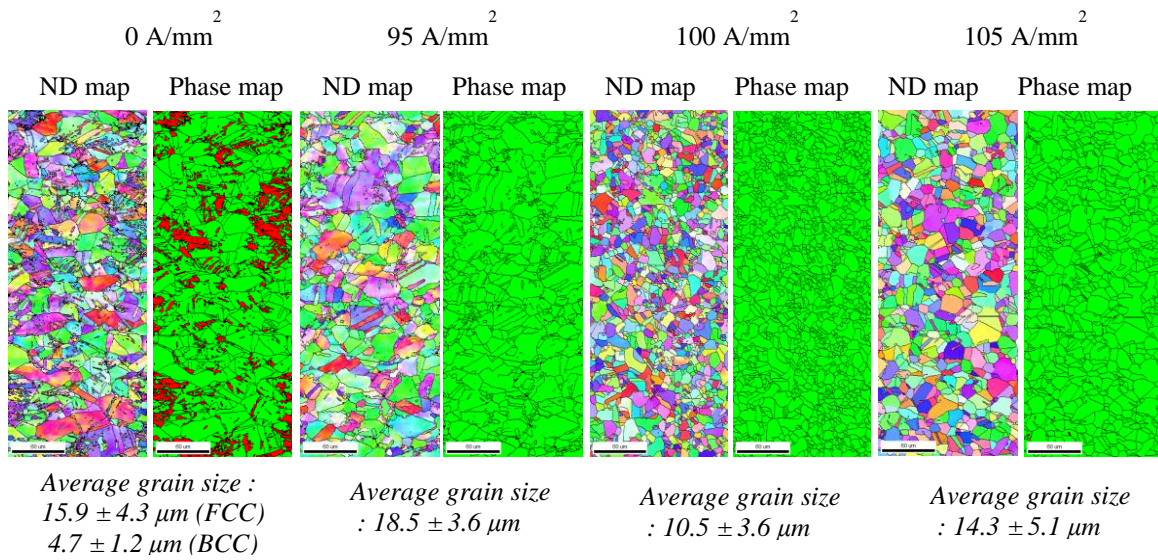


(b)

Figure 4. 10 X-ray diffraction spectra of specimens: (a) before EA annealing (b) with 60% prestrain after EA annealing

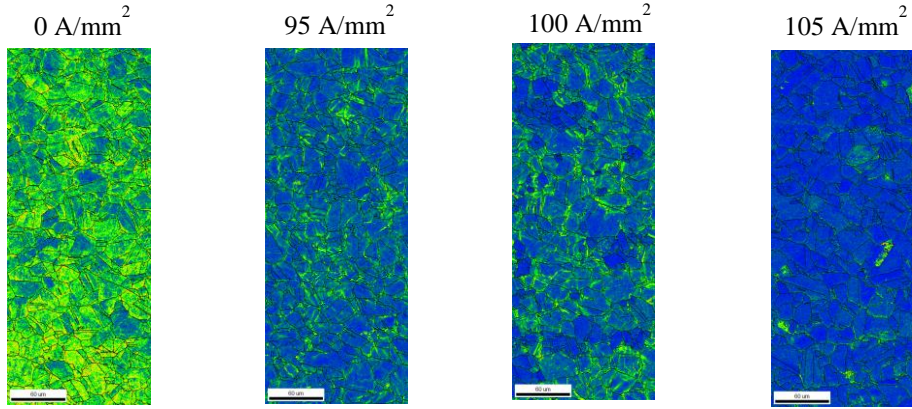
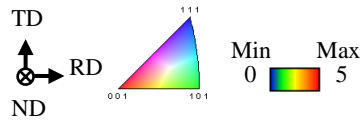


(a)

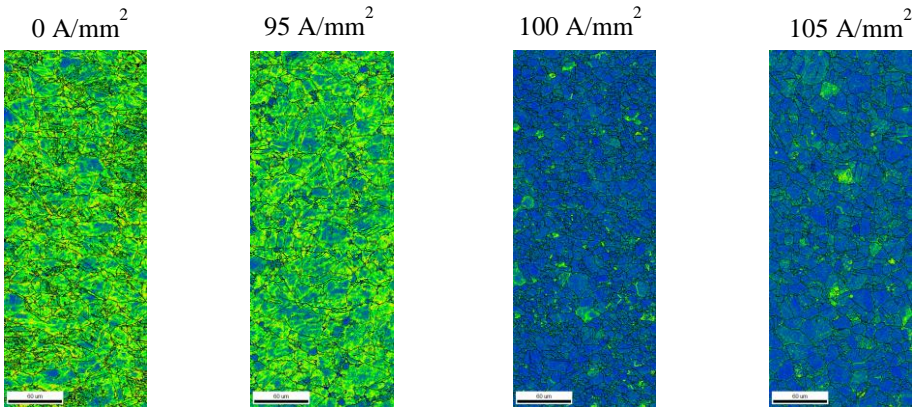


(b)

Figure 4. 11 EBSD inverse pole figures for ND and phase maps of specimens with (a) 20% prestrain and (b) 60% prestrain for various electric current densities



(a)



(b)

Figure 4. 12 Kernel average misorientation (KAM) maps with (a) 20% prestrain and (b) 60% prestrain for various electric current densities

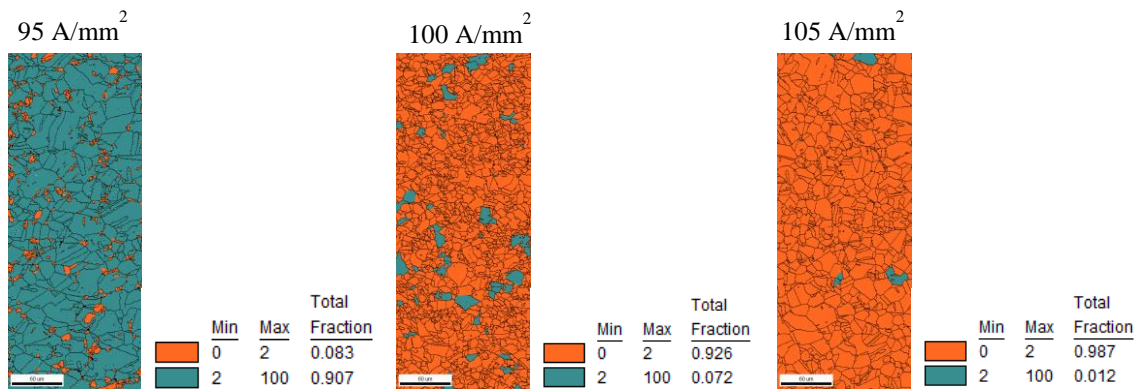
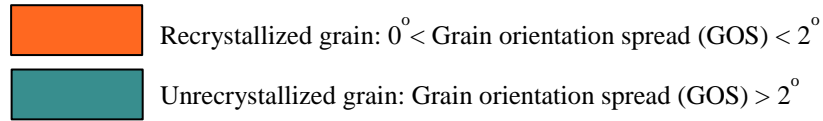


Figure 4. 13 Grain orientation spread (GOS) maps of specimens with 60% prestrain for various electric current densities

4.4 CONCLUSION

In the present study, the effect of EA subsecond annealing on the post-annealing mechanical and microstructural behavior of SUS304 was investigated. Under a quasi-static tensile test, the mechanical behavior of the prestrained specimen after applying a single pulse of electric current to the specimen suggests the occurrence of EA subsecond annealing. The results of the microstructural analysis show the annihilation of dislocations by the electric current, which confirms the occurrence of EA subsecond annealing. The increase in elongation of the SUS304 with EA subsecond annealing was due to two types of effect. One is the resetting martensite after EA subsecond annealing, causing the MIMT effect to be exhibited in the reloading test. The other is an annealing effect during application of electric current, which is identified by FWHM values from the XRD measurement and EBSD observation, respectively. Note that the annealing effect is including full annealing, recrystallization and reset MIMT effect. Therefore, this study suggests that the effect of electric current on the mechanical behavior can be strongly affected by microstructural phenomena in the selected metal alloy. The EAM technique can efficiently improve the formability by choosing the prestrain, current density in accordance with the material characteristic.

References

- Anderson, M., Gholipour, J., Bridier, F., Bocher, P., Jahazi, M., Savoie, J., Wanjara, P., 2013. Improving the Formability of Stainless Steel 321 through Multistep Deformation for Hydroforming. *Transactions of the Canadian Society for Mechanical Engineering* 37, 39–52.
- Conrad, H., 2000. Electroplasticity in metals and ceramics. *Materials Science and Engineering: A* 287, 276–287.
- Conrad, H., Karam, N., Mannan, S., 1983. Effect of electric current pulses on the recrystallization of copper. *Scripta Metallurgica* 17, 411–416.
- Conrad, H., Karam, N., Mannan, S., Sprecher, A.F., 1988. Effect of electric current pulses on the recrystallization kinetics of copper. *Scripta Metallurgica* 22, 235–238.
- Geijselaers, H.J.M., Perdahcioğlu, E.S., 2009. Mechanically induced martensitic transformation as a stress-driven process. *Scripta Materialia* 60, 29–31.
- Guy, K.B., Butler, E.P., West, D.R.F., 1983. Reversion of bcc α' martensite in Fe–Cr–Ni austenitic stainless steels. *Metal Science* 17, 167–176.
- Han, H.N., Lee, C.G., Suh, D.-W., Kim, S.-J., 2008. A microstructure-based analysis for transformation induced plasticity and mechanically induced martensitic transformation. *Materials Science and Engineering: A* 485, 224–233.
- Han, H.N., Oh, C.-S., Kim, G., Kwon, O., 2009. Design method for TRIP-aided multiphase steel based on a microstructure-based modelling for transformation-induced plasticity and mechanically induced martensitic transformation. *Materials Science and Engineering: A* 499, 462–468.
- Huang, G.L., Matlock, D., Krauss, G., 1989. Martensite formation, strain rate sensitivity, and deformation behavior of type 304 stainless steel sheet. *Metallurgical Transactions A* 20A, 1239–1246.

- Jeong, H.-J., Park, J., Jeong, K.J., Hwang, N.M., Hong, S.-T., Han, H.N., 2018. Effect of Pulsed Electric Current on TRIP-aided steel. *International Journal of Precision Engineering and Manufacturing-Green Technology* (in press).
- Kim, M.-J., Lee, K., Oh, K.H., Choi, I.-S., Yu, H.-H., Hong, S.-T., Han, H.N., 2014a. Electric current-induced annealing during uniaxial tension of aluminum alloy. *Scripta Materialia* 75, 58–61.
- Kim, M.-J., Lee, M.-G., Hariharan, K., Hong, S.-T., Choi, I.-S., Kim, D., Oh, K.H., Han, H.N., 2017. Electric current–assisted deformation behavior of Al-Mg-Si alloy under uniaxial tension. *International Journal of Plasticity*, 94, 148–170.
- Kim, M.-S., Vinh, N.T., Yu, H.-H., Hong, S.-T., Lee, H.-W., Kim, M.-J., Han, H.N., Roth, J.T., 2014b. Effect of electric current density on the mechanical property of advanced high strength steels under quasi-static tensile loads. *International Journal of Precision Engineering and Manufacturing* 15, 1207–1213.
- Lin, S.X., Chu, X.R., Bao, W.K., Gao, J., Ruan, L.Q., 2015. Experimental investigation of pulse current on mechanical behaviour of AZ31 alloy. *Materials Science and Technology* 31, 1131–1138.
- Luu, V., Nguyen, T., Hong, S.-T., Jeong, H.-J., Han, H., 2018. Feasibility of a Two-Stage Forming Process of 316L Austenitic Stainless Steels with Rapid Electrically Assisted Annealing. *Metals* 8, 815.
- Machlin, E.S., 1959. Applied Voltage and the Plastic Properties of ‘‘Brittle’’ Rock Salt. *Journal of Applied Physics* 30, 1109–1110.
- Mai, J., Peng, L., Lin, Z., Lai, X., 2011. Experimental study of electrical resistivity and flow stress of stainless steel 316L in electroplastic deformation. *Materials Science and Engineering: A* 528, 3539–3544.

- Mertinger, V., Nagy, E., Tranta, F., Sólyom, J., 2008. Strain-induced martensitic transformation in textured austenitic stainless steels. *Materials Science and Engineering: A* 481–482, 718–722.
- Michael F. McGuire, 2008. *Stainless Steels for Design Engineers* - ASM International.
- Okazaki, K., Kagawa, M., Conrad, H., 1978. A study of the electroplastic effect in metals. *Scripta Metallurgica* 12, 1063–1068.
- Padilha, A.F., Plaut, R.L., Rios, P.R., 2003. Annealing of Cold-worked Austenitic Stainless Steels. *ISIJ International* 43, 135–143.
- Park, J.-W., Jeong, H.-J., Jin, S.-W., Kim, M.-J., Lee, K., Kim, J.J., Hong, S.-T., Han, H.N., 2017. Effect of electric current on recrystallization kinetics in interstitial free steel and AZ31 magnesium alloy. *Materials Characterization* 133, 70–76.
- Rocha, M.R. da, Oliveira, C.A.S. de, 2009. Evaluation of the martensitic transformations in austenitic stainless steels. *Materials Science and Engineering: A* 517, 281–285.
- Smith, H., West, D.R.F., 1973. The reversion of martensite to austenite in certain stainless steels. *Journal of Materials Science* 8, 1413–1420.
- Thanakijkasem, P., Uthaisangasuk, V., Pattarangkun, A., Mahabunphachai, S., 2014. Effect of bright annealing on stainless steel 304 formability in tube hydroforming. *The International Journal of Advanced Manufacturing Technology* 73, 1341–1349.
- Thien, N.T., Hong, S.-T., Kim, M.-J., Han, H.N., Yang, D.-H., Lee, H.-W., Lee, K., 2016. Electrically assisted bake hardening of complex phase ultra-high strength steels. *International Journal of Precision Engineering and Manufacturing* 17, 225–231.
- Troitskii, O.A., 1969. Electromechanical Effect in Metals. *ZhETF Pisma Redaktsiiu* 10, 18.
- Ungár, T., Borbély, A., 1996. The effect of dislocation contrast on x-ray line broadening: A new approach to line profile analysis. *Applied Physics Letters* 69, 3173–3175.

Williamson, G.K., Hall, W.H., 1953. X-ray line broadening from filed aluminium and wolfram.
Acta Metallurgica 1, 22–31.

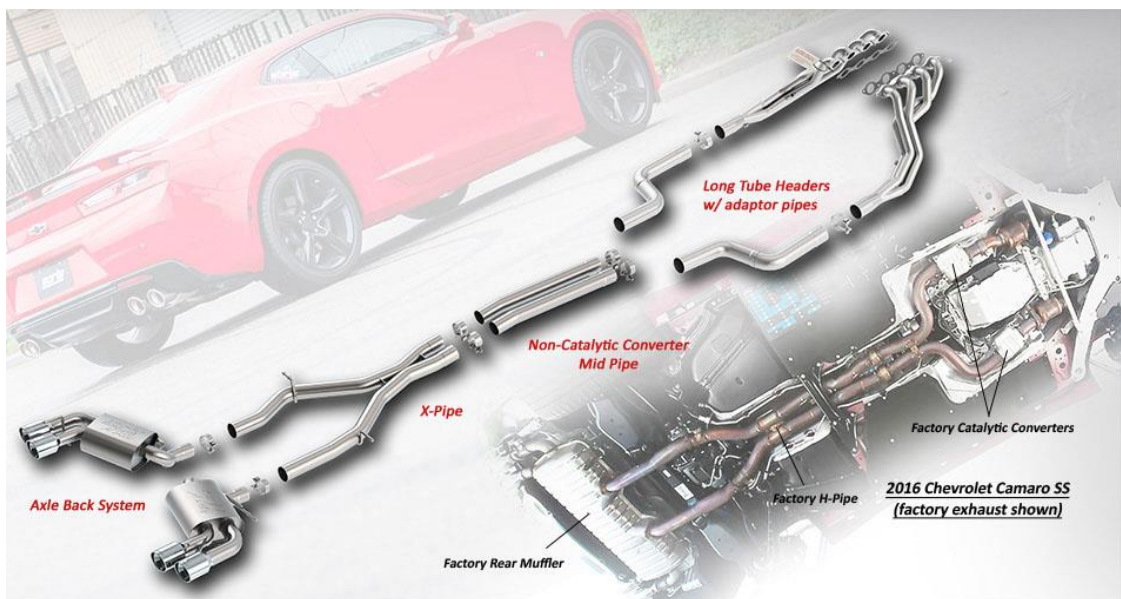
CHAPTER V

INDUSTRIAL APPLICATIONS

5.1 Industrial application of electrically assisted brazing technique in automotive exhaust systems

Automotive exhaust pipes are required to be thin-walled from the standpoint of energy saving and weight reduction, and yet they have to satisfy stringent requirements such as endurance, corrosion resistance, and heat resistance. The products of thin-wall welded stainless steel pipes have been employed by many automobile manufacturers as a mother material for components of automotive exhaust gas pipe systems comprising exhaust manifold, mufflers, axle back system, and catalytic converter, as shown in Figure 5.1.

Recently, there are several joining technique such as Arc welding, MIG welding, precision welding, torch welding, laser welding, hot pressure welding, and fusion welding. However, conventional welding processes may not be suitable for joining thin stainless steel sheets and may make it difficult to accommodate the recent industry trends of using thinner sheet materials for weight reduction. As shown in Chapter II, electrically assisted (EA) brazing is well known an advantage technique for thin sheet metal joining. In particular, we apply the EA brazing technique to joining parts of automotive exhaust pipe systems. This advantage technique could reduce weight ratio and cost of the exhaust pipe systems.



<https://www.borla.com/products/exhaust-systems/#>

Figure 5. 1 Schematic of an automotive gas exhaust pipe system

A ferritic stainless steel (FSS) with 1.0 mm thickness exhaust pipe system (Sejong, South Korea) is provided in distinct two parts. A nickel-based paste filler (AMS 4777, Lucas-Milhaupt Incorporated, USA) with its chemical composition (Ni-3.0Fe-7.0Cr-3.1B-3.4Si in wt.%) was used for brazing. The brazing joint with a length of 5 mm and a diameter of 47.6 mm was prepared by fulfilling the paste filler into the gap between two parts of the exhaust pipe system (as marked in Figure 5.3). A programmable welder (VADAL SP-1000U, Hyosung, South Korea) was used to apply an electric current to the specimens. A test fixture was designed to clamp and place the exhaust pipe system into the fixture, as described in Figure 5.2. Also, a pair of copper electrodes was used to apply electric current through the joint of the exhaust pipe system. A pulsed electric current was used for EA brazing. During EA brazing, the joint temperature with Ni-based filler was rapidly increased to the brazing temperature ($\approx 1100^{\circ}\text{C}$) by applying a pulsed electric current, which had a magnitude of I_i and a duration of t_i . The joint temperature was then held nearly constant for an additional holding time by periodically applying an electric current with time t_h by periodically applying an electric current I_m with a duration of t_m and a period of μ_m , as described in Chapter II. The heating parameters for the EA brazing and the induction brazing are listed in Table 5.1.

After brazing, the cross-sectional samples were prepared along the length direction of the brazed joint for microstructural analysis. The cross-sectional samples were processed using a standard metallographic grinding and polishing procedure and were finished with a 1 μm diamond suspension. The cross-sectional samples were examined using an optical microscope (confocal machine) to confirm that the brazing joint was successfully fabricated.

The joining of the exhaust pipe system with 1 mm wall thickness was successfully joined using the Ni-based filler metal by using EA brazing technique, as shown in Figure 5.3. The optical microscope pictures of cross-sectional specimens show that the intermetallic layers were precipitated between FSS base metal and filler metal (Figure 5.4). The average thickness of intermetallic layers (as marked blue dash line) is approximately 3.5 μm , which was measured by the optical microscope. These results suggest that the joining of the exhaust pipe system can be simplified and expedited by EA brazing process. Also, with a short brazing time process (25 sec) and a small amount of paste filler metal (20 gram), the EA brazing process of the exhaust pipe system may significantly reduce process time and weight ratio for joining the exhaust pipe system in comparison with conventional welding processes. Hence, the joining of thin wall materials using EA brazing technique can be simply and widely applied in many manufacturing processes.

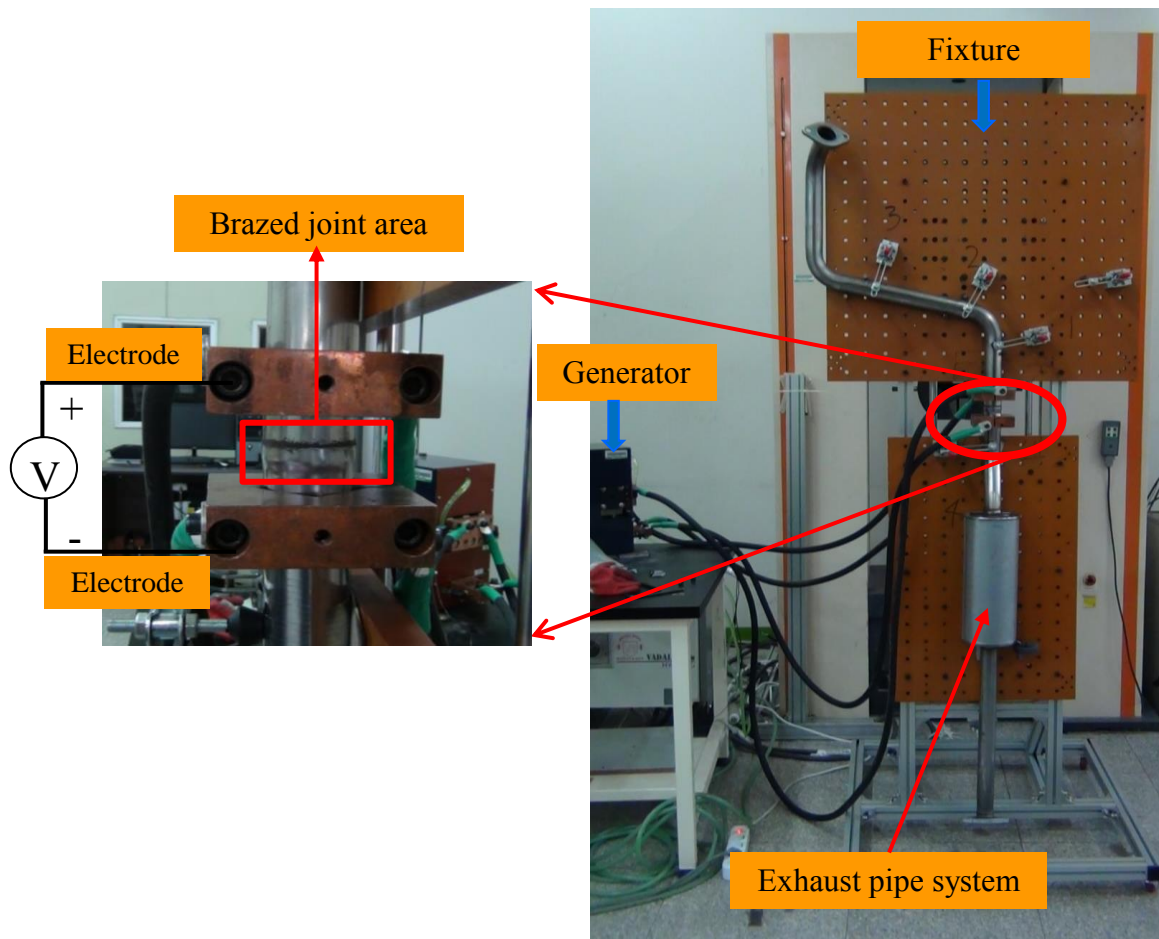


Figure 5. 2 Schematic of experimental set-up for EA brazing exhaust pipe system

Type	Electric current I_i (A)	Duration time t_i (sec)	Electric current I_m (A)	Period time μ_m (sec)	Duration time t_m (sec)	Number of pulses (pulses)
Electrically assisted brazing	5000	5	2300	0.2	1	17

Table 5. 1 Heating parameters for electrically assisted brazing and induction brazing

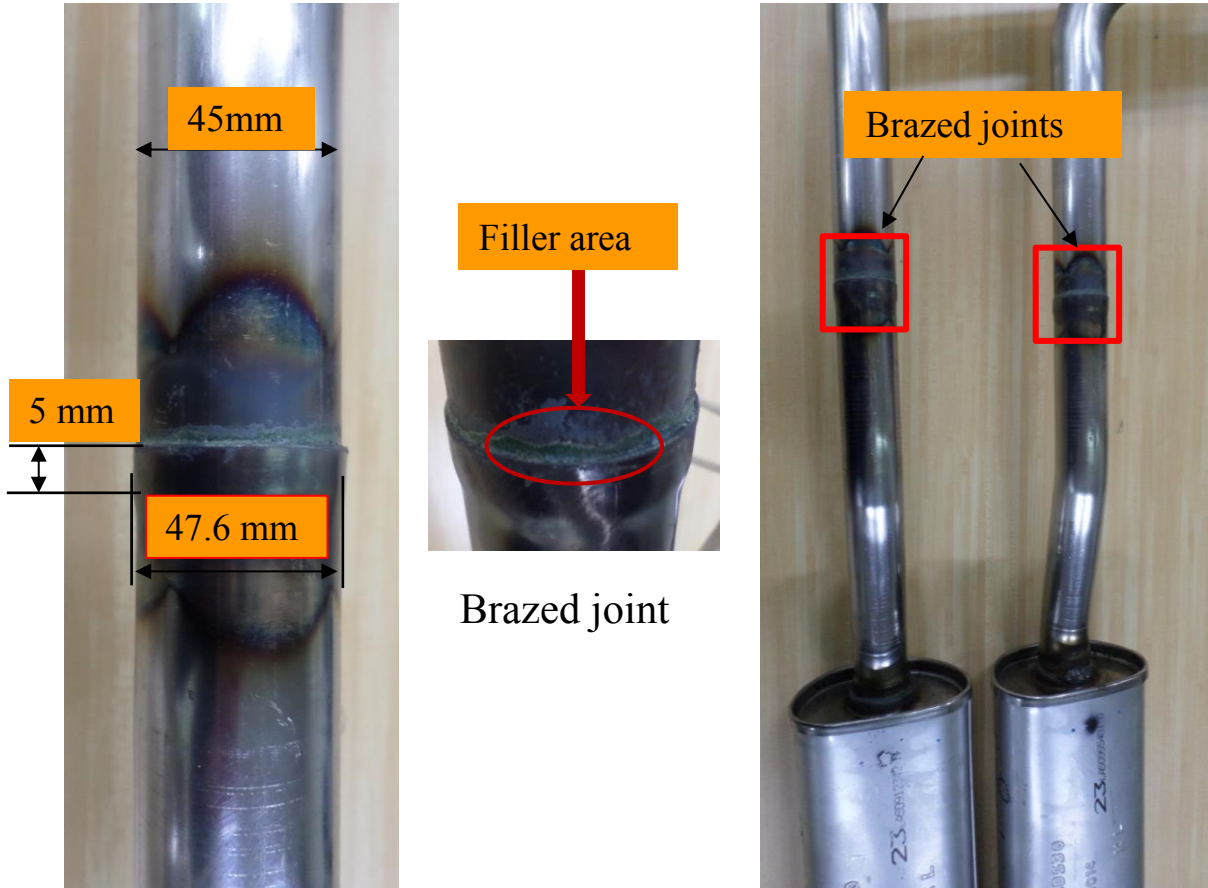


Figure 5. 3 Braze joints of exhaust pipe systems after EA brazing

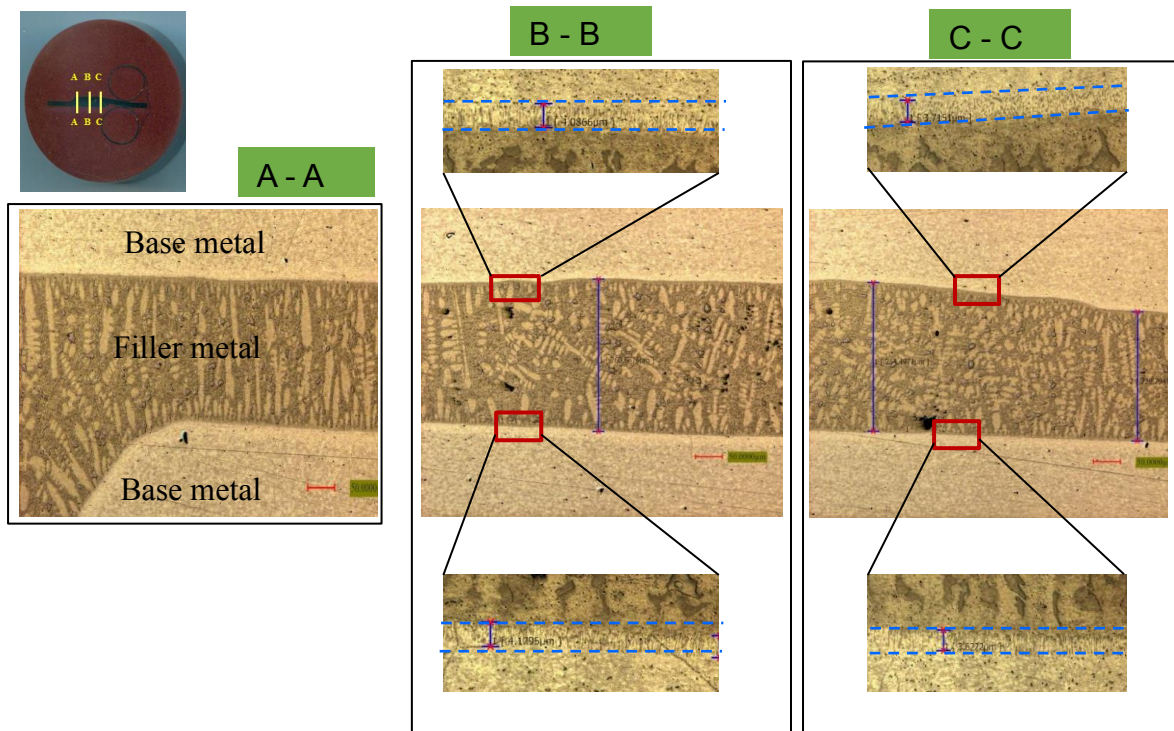


Figure 5. 4 The optical microscope of the brazed joint after EA brazing; blue dash line as marked the intermetallic layers; thickness of intermetallic layers in top and bottom of the brazed joint is a range of 3.0 to 4.0 μm

5.2 Electrically assisted springback reduction of bipolar plates for fuel cell

Fuel cell technology has gained increasing attention as a substitute for internal combustion engines in transportation applications. This technology promises high fuel efficiency and zero greenhouse and toxic gas emissions. A proton exchange membrane fuel cell (PEMFC) has been reported as the most promising technology owing to its superior performance at low temperature, prolonged operation time, rapid initiation and compact structure (Heras et al., 2009). These characteristics make PEMFCs very attractive as a power source for vehicles in comparison with other fuel cell systems. However, there are many technological challenges to overcome before mass production and commercialization of this technology. One of these challenges is the development of materials for bipolar separator plates (or simply, bipolar plates) able to offer long-term durability, reduced volume, lightweight and minimum manufacturing costs.

Graphite or graphite composite has been often used to produce bipolar plates owing to their low density, good corrosion resistance, and low interfacial contact resistance. However, mass production of the graphite bipolar plates is challenging and costly, and a certain thickness is required to compensate its high gas permeability. In order to overcome the drawbacks of graphite for the bipolar plates, various materials have been considered as a substitute. Among them, stainless steels have gained extensive attention because of its low stack cost, superior mechanical and thermal properties, and satisfactory workability (Hermann et al., 2005; Jin et al., 2014; Shimpalee et al., 2016).

Although the stamping process is much faster than mechanical machining, its drawback is that precision manufacturing is difficult. When channels are formed in stainless steel plates with a thickness of 0.1 mm through the stamping process, forming defects such as springback, cracks, thinning, wrinkles, surface corrugations, and warping occur. The biggest problem of mass-produced bipolar plates is that the channels do not form in the desired shapes but are

instead fabricated irregularly because of the springback (Chen et al., 2011; Jin et al., 2014).

Recently, electrically assisted forming (EAF) is a promising technique which can reduce or even eliminate springback after forming. Electrically assisted (EA) springback process is carried out to reduce or eliminate the springback of the bipolar plates with thin sheet stainless steels. The preformed 316L stainless steel bipolar plates with 0.1 mm thickness (provided by Sejong company) were prepared for EA springback. The electric current was generated by a programmable Vadal SP-1000U power supply (Hyosung, South Korea). By inserting a set of bakelite insulator plates between the copper electrodes and the upper and bottom part of the die, the compression machine was insulated from the electric current (Figure 5.5). A bipolar plate was firstly inserted inside the die and was then applied a pulsed electric current through the bipolar plate. Finally, the bipolar plate was removed from the die to measure the springback. Note that the springback height of the bipolar plates after EA springback was measured using Vernier caliper equipment. For parameter study, two different sets of pulsed electric current (100 pulses and 200 pulses) were applied to the bipolar plates in the EA springback test as shown in Table 5.2.

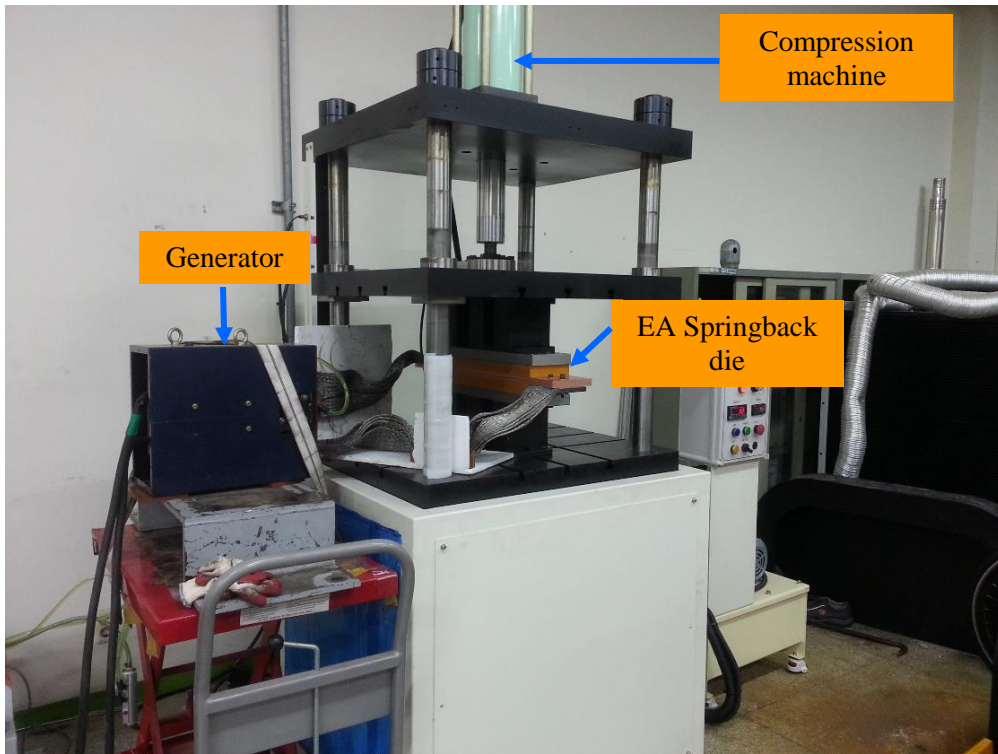
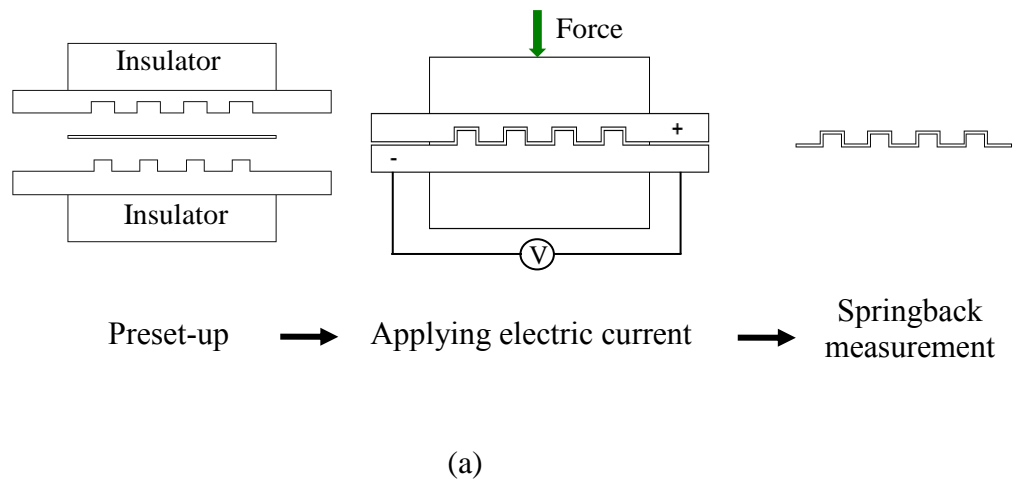
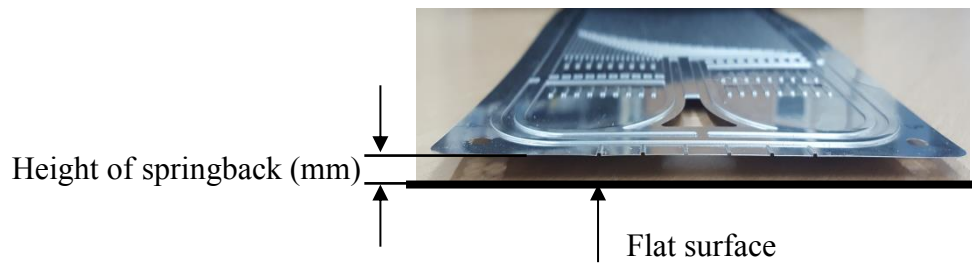


Figure 5. 5 (a) Electrically assisted springback reduction procedure of bipolar plates and (b) Schematic of experimental set-up in EA springback test

Sort	Electric current (KA)	Number of pulses (pulses)	Duration (sec)	Period time (sec)	Repeat (times)
	12	50	1	0.5	2 and 4
Material thickness			0.1 mm		
Load			2500 N		

Table 5. 2 Springback test parameters



(a)



(b)

Figure 5. 6 A SUS316L bipolar plate specimen after EA springback

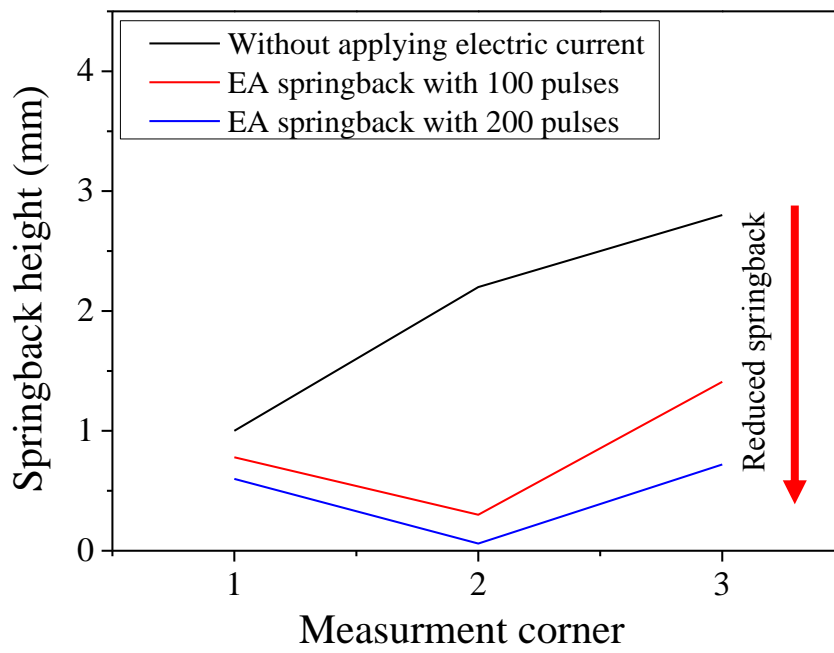


Figure 5. 7 Springback reduction height of bipolar plates after applying electric current

As expected, the formed bipolar plates were significantly reduced the springback by applying a pulsed electric current, as shown in Figure 5.6. The reduction in springback may be understood as a consequence of the reduction in the amount of elastic recovery due to the stress-drop at the pulse of electric current (Kim et al., 2014). For evaluation the springback reduction, the bipolar plate specimens were placed on the flat surface (as marked in Figure 5.6(a)) and then the height of points at the corner of the bipolar plates before/after EA springback was measured, as marked in Figure 5.6. As a result, the height of bipolar plate after applying electric current at selected points significantly reduced in comparison with the height of bipolar plate without applying electric current (initial preformed bipolar plate), as shown in Figure 5.7. Also, the height at the selected points is reduced with increasing the number of applied pulses electric current. However, 100% springback elimination is not achieved in the current state conditions, since the equipment is still not capable to increase the number of applied pulses electric current. Even though, the result of the study clearly shows that the EA springback technique is feasible with the significant benefits of reduced springback in thin sheet metal forming. Especially, the advantaged technique can be applied for manufacturing of bipolar plates with less than 0.1 mm metal thickness.

References

- Chen, T., Gu, Y.F., Li, C.P., Qiao, Y.Q., 2011. Stamping and Springback of PEMFC Metal Bipolar Plate. *Advanced Materials Research* 215, 1-4.
- Heras, N. de las, Roberts, E.P.L., Langton, R., Hodgson, D.R., 2009. A review of metal separator plate materials suitable for automotive PEM fuel cells. *Energy Environ. Sci.* 2, 206-214.
- Hermann, A., Chaudhuri, T., Spagnol, P., 2005. Bipolar plates for PEM fuel cells: A review. *International Journal of Hydrogen Energy* 30, 1297-1302.
- Jin, C.K., Koo, J.Y., Kang, C.G., 2014. Fabrication of stainless steel bipolar plates for fuel cells using dynamic loads for the stamping process and performance evaluation of a single cell. *International Journal of Hydrogen Energy* 39, 21461-21469.
- Kim, M.-S., Vinh, N.T., Yu, H.-H., Hong, S.-T., Lee, H.-W., Kim, M.-J., Han, H.N., Roth, J.T., 2014. Effect of electric current density on the mechanical property of advanced high strength steels under quasi-static tensile loads. *International Journal of Precision Engineering and Manufacturing* 15, 1207-1213.
- Shimpalee, S., Lilavivat, V., McCrabb, H., Khunatorn, Y., Lee, H.-K., Lee, W.-K., Weidner, J.W., 2016. Investigation of bipolar plate materials for proton exchange membrane fuel cells. *International Journal of Hydrogen* 41, 13688-13696.

CHAPTER VI

CONCLUSION

In chapter II, the effectiveness of electrically assisted brazing was compared with that of conventional induction brazing by joining ferritic stainless steel sheets with a Ni-based filler metal. As shown in the microstructural analysis results, the electric current during electrically assisted brazing significantly enhanced the diffusion between the filler metal and the ferritic stainless steel sheets in comparison with induction brazing. The enhanced diffusion during electrically assisted brazing strongly supports the athermal effect of electric current, which is closely related to the theory of electroplasticity. Also, the results of mechanical tests showed that electrically assisted brazing provided a joint strength comparable to the strength of the induction brazing joint with a significantly shorter processing time. Therefore, the electrically assisted brazing provides the technical advantage that the process time can be significantly reduced without sacrificing the joint strength (or a higher joint strength with a similar process time) in comparison with induction brazing. Also, due to the significantly higher heating rate, the energy loss to the environment during heating is likely to be less in electrically assisted brazing than in induction brazing. These superior properties of electrically assisted brazing over induction brazing could make electrically assisted brazing a strong candidate to replace conventional induction brazing.

In chapter III, the effects of a single pulse of electric current on the mechanical behavior and microstructure of a commercially available SUS316L were investigated to evaluate the feasibility of a two-stage forming process with rapid EA annealing in less than 1 sec. The mechanical behavior of the prestrained specimen after applying a single pulse of electric current to the specimen suggests the occurrence of EA annealing. The results of microstructural analysis show the annihilation of dislocations by the electric current, confirming the occurrence

of EA annealing. The experimental results show that the effectiveness of EA annealing strongly depends not only on the electric current parameters, but also the magnitude of the prestrain. Depending on the electric current parameters and the magnitude of the prestrain, full annealing with recrystallization was even possible to significantly increase the total maximum achievable elongation of the specimen. The results of the present study suggest that a two-stage forming process of SUS316L can be simplified and expedited by properly implementing rapid EA annealing in the process.

In chapter IV, the effect of EA subsecond annealing on the post-annealing mechanical and microstructural behavior of SUS304 was investigated. Under a quasi-static tensile test, the mechanical behavior of the prestrained specimen after applying a single pulse of electric current to the specimen suggests the occurrence of EA subsecond annealing. The results of the microstructural analysis show the annihilation of dislocations by the electric current, which confirms the occurrence of EA subsecond annealing. The increase in elongation of the SUS304 with EA subsecond annealing was due to two types of effect. One is the resetting martensite after EA subsecond annealing, causing the MIMT effect to be exhibited in the reloading test. The other is an annealing effect during application of electric current, which is identified by FWHM values from the XRD measurement and EBSD observation, respectively. Note that the annealing effect is including full annealing, recrystallization and reset MIMT effect. Therefore, this study suggests that the effect of electric current on the mechanical behavior can be strongly affected by microstructural phenomena in the selected metal alloy. The EAM technique can efficiently improve the formability by choosing the prestrain, current density in accordance with the material characteristic.